KU LEUVEN

ARENBERG DOCTORAL SCHOOL
Faculty of Engineering Science

Numerical Simulation of Two-Dimensional Bubble Dynamics and Evaporation

Xue Wang

Supervisors:
Prof. Bart Blanpain
Prof. Jan Degrève

Dissertation presented in partial fulfillment of the requirements for the degree of Doctor in Engineering Science

May 2015

Numerical Simulation of Two-Dimensional Bubble Dynamics and Evaporation

Xue WANG

Examination committee:
Prof. Willy Sansen, chair
Prof. Bart Blanpain, supervisor
Prof. Jan Degrève, supervisor
Prof. Patrick Wollants
Prof. Frederik Verhaeghe
Prof. Véronique Roig
(IMFT, Toulouse, France)
Prof. Geraldine Heynderickx
(Ghent University, Belgium)

Dissertation presented in partial
fulfillment of the requirements for
the degree of Doctor
in Engineering Science

May 2015

Uitgegeven in eigen beheer, Xue Wang, Kasteelpark Arenberg 44 bus 2450, B-3001 Heverlee (Belgium)

Acknowledgments

“*It is the time you have wasted for your rose that makes your rose so important.*”
– Antoine de Saint-Exupéry, The Little Prince

For me, pursuing a PhD is like planting a rose. It started with some buds of ideas, followed by sharp thorns, and finally ended with beautiful blossoms. In this marvelous adventure, many colleagues and friends encouraged me to conquer the thorns and gave me a hand to fertilize the soil. You all deserve a giant thank you!

Thank you, Prof. Bart Blanpain. I am proud of being your student. Back in October 2010, I wrote you an email that “I will come” and suddenly appeared in front of you. Now all of a sudden, it is time to leave. At this special moment, I would like to thank you for teaching me to write, to communicate, to play Boerengolf and to peel the potatos; thank you for teaching me to fish, instead of giving me fish, even though you were deeply worried whether I would catch one; thank you for your patience and thank you for providing me a free and relaxed environment. In China we have an old saying: "a teacher for a day is a father for a lifetime". All the things that you taught me can influence the rest of my life.

Thank you, Prof. Jan Degrève, for being my promoter. Thank you for your generous help when I am down; thank you for correcting my writing word by word; thank you for teaching me to defend myself and thank you for your congratulations on my every tiny improvement. We can slove anything even without MAOTAI.

Thank you, Prof. Frederik Verhaeghe. Without the interesting project that you wrote, I could not have the opportunity to come here. Thank you for being our research line leader and for organizing a lot of valuable discussions. Thank you, Prof. Patrick Wollants, for assessing my current work in all these years and for your advice and suggestions on the thesis. I also would like to thank Prof. Geraldine Heynderickx and Prof. Véronique Roig. It is my great honor to have you in my jury. Thanks to both of you for reading my thesis very carefully and for travelling twice to leuven to discuss in details. Thank you, Prof. Willy Sansen for taking your time and energy to chair my defences. Thanks to all of you for your unique contributions!

Thank you, Muxing. I will never forget the first two calls from you when I was still in China. Thank you for your encouragement and support. Sometimes it was just a word or a look, but I can read it. Thank you, Prof. Jan Baeyens, for sharing life experience and delicious fish meal with me, also for your kindness to my family.

Thank you, all the HiTemp group members (Pyro and Sremac). Time is magic. In the past few years, together, we shared the joy of HiTempers' marriage (Bart, S & Y, Thomas, Huai, Huayue, Lichun, Bin. . .), and witnessed the birth of HiTemp babies (Hendrik, Zhaoqing, Ellie & Tiebe, Sofia, Eric, Pengpeng, Jade & Ruben, Lilly, Maria, Nicola. . .). We have many wonderful academic activities, but also enjoy a lot of games (bowling, hiking, werewolves, cooking, drawing. . .). Here, I would like to express my special thanks to some colleagues that related to my work. Thank you, Bart. You showed me the talent of a PhD and paved the way for my work. Thank you, Lesley, for the conference in Trondheim and the Dutch abstract from Australia. Thank you, Chunwei, for the workshop in Dresden. Thank you, Vishal, Zhi and Bin, for your great ideas, inspiring discussions and selfless help. Thank you, Pengcheng, for your assistance in experiments, for reading my manuscripts many times, and for pushing me all the time. Thank you, my officemates Xiaoling, Prof. Nele Moelans, Philip, Qingge and Prof. Raf Schouwenaars, for your company and support. Thank you, all the colleagues in MTM, especially the kind help from Dirk, Mia, Mieke, Huberte, Jennifer, Paul, Rudy, Olivier, Pieter, Louis, Danny, Britt, Joop, Gert and Joris. I wish to acknowledge the financial support from Research Foundation Flanders (FWO) under Grant No.0433.10N.

Thank you, Prof. Marie-Françoise Reyniers, for arranging the visit to your group. The stay in LCT, UGent is enjoyable and fruitful. Thank you, Amit. Your deep thinking and solid knowledge can always broaden my horizons and improve my understandings. Thanks to all the colleagues there for treating me friendly. The happy hours and the birthday chocolates are memorable.

Also, there are many friends in Leuven I would like to thank. Thank you, Pengcheng, for showing me the fabulous sports centre when I was staying at home all day long. Thank you for being my coach, sports partner and mentor at the same time. Thank you, Xiebin, for guiding me all the time and spending a lot of time revising my thesis. Thank you, Ling, for bringing me to many beautiful places. Thank you, Xuan, for the best organizations of our trip. Thank you, Xiaoling & Zhi, for taking care of me for a very long time; thank you, Hao

& Bin, for providing me help whenever I need it; thank you, Wenxu & Xuan for letting me not alone during the Chinese new year; thank you, Yichen & Jian, for showing our family the beauty of Germany; thank you, Xiaodong, Minxian & Huayue, Chunwei and Chen for the wonderful get-together; thank you, Liugang & Yanyan, for the Beijing Roast Duck from Brussels; thank you, Lichun & Jiemei, for the home-made food; Thank you, Fei & Gong, Yuanyuan, Jingjing & Ji, Huili, Yujie, Shuigen, Qingge, Luman, Zhuangzhuang for making my stay in MTM colorful. Thank you, Yanyan, Yu, Lei, Ling, Zhe, Yejun, Tiannan, Hong and Jun for a lot of fun together. Specially, thank you, Yanyan, for providing me experimental materials and temporary accommodation.

Finally, I thank my family for their endless support. Thank you, my husband, for your broad shoulders and unconditional love. Thank you, my parents, for raising me up. Thank you, my sister and brother, for sharing the joys and sorrows. Thank you, my parents-in-law, for treating me as your own daughter and for putting all your efforts to my daughter. Thank you, my lovely daughter, for being happy every day. Mum is coming home and this thesis is for you!

Abstract

Gas bubble-melt interaction plays an important role in non-ferrous and ferrous metallurgical processes. During these processes, gas is injected into a metal bath for stirring or to add reactants at high temperature. The study of characteristics of liquid metal dynamics remains a challenge due to the limitations of current observation methods. The situation is further complicated as mass and heat transfer occur during the interaction. On the other hand, water has a similar kinematic viscosity as liquid metal, and therefore can be used to simplify the experimental situation for observations. Combined with proper numerical simulations, the gas bubble-water interaction can be extended to gas bubble-melt interaction, and can provide a partial insight in interactions at high temperature. In the present work, the gas bubble-liquid interaction is investigated based on a mesoscopic two-dimensional multiphase CFD (Computational Fluid Dynamics) model. The main research work is divided into two parts: (1) 2D numerical simulations of the quasi-two-dimensional inert bubble dynamics in liquid water and experimental validation. (2) 2D numerical simulations of bubble dynamics and evaporation in hot water.

In the first part, the buoyancy-driven single bubble behavior in a vertical Hele-Shaw cell was studied experimentally and numerically. The bubble behavior was simulated by taking a two-dimensional volume of fluid (VOF) method coupled with a continuum surface force (CSF) model and a wall friction model. By adjusting the viscous resistance values, the bubble dynamics in different gap thicknesses were simulated. The first simulations were carried out in a narrow cell (cell width $W = 5$ cm) with two gap thicknesses ($h = 0.5$ mm and 1.0 mm). For the main bubble flow properties including shape, path, terminal velocity, horizontal vibration and shape oscillation, a good agreement is obtained between experiment and simulation. The simulation confirms that the thin liquid films present between gas bubbles and the cell walls have a limited effect on the bubble dynamics.

The simulations were then expanded into four gap thicknesses and the effects of gap thickness on the bubble dynamics were discussed. It was found in both experiments and simulation that with an increased spacing between the cell walls, the bubble shape changes from oblate ellipsoid and spherical-cap to more complicated shapes while the bubble path changes from only rectilinear to a combination of oscillating and rectilinear; the bubble drag coefficient decreases and this results in a higher bubble velocity caused by a lower pressure exerted on the bubble; the wake boundary and wake length evolve gradually accompanied by vortex formation and shedding. Finally, the simulations were extended to a wide Hele-Shaw cell (W = 40 cm). The simulated bubble-induced liquid velocity and the released vorticity were compared with Roig *et al.*'s experimental measurements.

In the second part, the liquid water evaporating into the gas bubble was simulated by incorporating interfacial mass transfer at the interface grid cells between the liquid and gas bubble. The coupling between momentum and mass transfer was incorporated using a user-defined function (UDF). The local evaporation rate was derived from the Hertz-Knudsen equation. The measurements of Pauken for water evaporation rate in a moving air stream were used to mimic the interfacial evaporation at the bubble interface. The grid independence of the interfacial mass transfer flux was proven. The evolution of mass transfer rate and mass concentration in the bubble can be captured, as well as the interaction of the mass transfer and hydrodynamic properties.

Beknopte samenvatting

De interactie tussen een gasbel en de vloeistof speelt een belangrijke rol in non-ferro en ferro-metallurgische processen. In deze processen wordt een gas geïnjecteerd in het metaalbad voor het mengen of voor de toevoeging van reactanten bij hoge temperatuur. Enerzijds blijft studie naar de karakteristieke kenmerken van metaalhydrodynamica een uitdaging, vanwege de beperkingen van de huidige observatietechnieken. Het gelijktijdig optreden van massa- en warmtetransport met de gas-vloeistof interacties maakt de situatie nog ingewikkelder. Anderzijds heeft water een gelijkaardige kinematische viscositeit als vloeibaar metaal, waardoor het als substituut kan dienen en hiermee de observaties aan de hand van experimenten vereenvoudigt. In combinatie met gepaste numerieke simulaties kan het een gedeeltelijk inzicht bieden in de interacties op hoge temperatuur. In het huidig werk wordt de gasbel-vloeistof interactie onderzocht aan de hand van een mesoscopisch, twee-dimensioneel, multifase CFD (computationele vloeistofdynamica) model. Het onderzoek is opgedeeld in twee delen: (1) Een 2D numerieke simulatie en experimentele validering van de quasi-twee-dimensionele interactie tussen een inerte gasbel en water. (2) Een 2D numerieke simulatie van de beldynamica en verdamping in warm water.

In het eerste deel wordt eerst het gedrag van één enkele opwaartse gasbel experimenteel en numerisch bestudeerd aan de hand van een verticale Hele-Shaw cel. Het belgedrag werd gesimuleerd gebruikmakend van een twee-dimensionele Volume-of-Fluid (VOF) methode, gekoppeld met het Continuum Surface Force (CSF) model en een model voor de wrijving met de wand. Door aanpassing van de viskeuze weerstandswaarden kan de beldynamica voor verschillende diktes van de opening bestudeerd worden. De initiële simulaties werden uitgevoerd voor een smalle cel (celbreedte $W = 5$ cm) met twee diktes ($h = 0.5$ en 1.0 mm). Een goede overeenkomst tussen experiment en simulaties werd bekomen voor de algemene beldynamica eigenschappen, zoals vorm, traject, eindsnelheid, horizontale trillingen en vormveranderingen. De simulaties bevestigen dat de dunne vloeistoffilm tussen de gasbel en de wand slechts een beperkte invloed

heeft op de beldynamica.

Vervolgens werden de simulaties uitgebreid naar vier diktes en werd het effect van de dikte op de beldynamica bestudeerd. In zowel de experimenten als de simulaties werd bevonden dat, met een toenemende dikte, de vorm van de bel overgaat van een afgeplatte ellipsoïde en een bolkap gasbel naar meer ingewikkelde vormen, terwijl het beltraject overgaat van rechtlijnig naar een combinatie van oscillerend en rechtlijnig; de belwrijvingscoëfficient neemt af en dit leidt tot een hogere snelheid vanwege een lagere druk uitgeoefend op de bel; de grens en lengte van het kielzog neemt geleidelijk aan toe en wordt vergezeld van vorming en afstoten van vortices. Als laatste werden de simulaties verder uitgebreid naar een brede Hele-Shaw cel ($W = 40$ cm). De berekende vloeistofsnelheid, opgewekt door de gasbel, en de vrijgekomen vorticiteit werden vergeleken met de experimenteel opgemeten waarden van Roig *et al.*

In het tweede deel wordt een simulatie uitgevoerd van de verdamping van water naar de gasbel door het in rekening brengen van het grensvlakmassatransport in de roostercellen met een grensvlak. De koppeling tussen de momentum- en massaoverdracht werd ingebouwd aan de hand van een zelfgeschreven subroutine (User-Defined Function; UDF). De lokale verdampingssnelheid werd bekomen door middel van de Hertz-Knudsen vergelijking. De verdamping aan het grensvlak werd nagebootst aan de hand van verdampingssnelheden in een luchtstroom, verkregen uit de experimenten van Pauken. De flux van het grensvlakmassatransport werd getest op roosteronafhankelijkheid. Het is mogelijk zowel de evolutie van massaoverdrachtsnelheid, de massaconcentratie in de gasbel, als de interactie tussen de massaoverdracht en de hydrodynamische eigenschappen vast te leggen.

Nomenclature

α	Viscous resistance	[m^2]
γ	Volume fraction	
δ_{film}	Film thickness	[m]
η	Evaporation coefficient	
κ	Curvature	[m^{-1}]
$\mathit{\Lambda}$	Thermal conductivity	[$\mathrm{W{\cdot}m^{-1}{\cdot}K^{-1}}$]
μ	Dynamic viscosity	[$\mathrm{Pa{\cdot}s}$]
ν	Kinematic viscosity	[$\mathrm{m^2{\cdot}s^{-1}}$]
ρ	Average density	[$\mathrm{kg{\cdot}m^{-3}}$]
σ	Surface tension	[$\mathrm{N{\cdot}m^{-1}}$]
τ	Dimensionless time	
φ	Velocity constant	
χ	Mole fraction	
ω	Mass fraction	
$\mathit{\Omega}$	Vorticity	[s^{-1}]

A	Interface area	[m^2]
Ar	Archimedes number	
Bo	Bond number	
c	Evaporation parameter	[$\mathrm{s{\cdot}m^{-1}}$]
c_A	Concentration	[$\mathrm{mol{\cdot}m^{-3}}$]
c_p	Heat capacity	[$\mathrm{J{\cdot}kg^{-1}{\cdot}K^{-1}}$]
C_a	Capillary number	
C_D	Drag coefficient	
d	Bubble diameter	[m]
D	Diffusion coefficient	[$\mathrm{m^2{\cdot}s^{-1}}$]
E	Energy	[$\mathrm{J{\cdot}kg^{-1}}$]
Eo	Eötvös number	

E_s	Energy source term	$[\mathrm{J{\cdot}m^{-3}{\cdot}s^{-1}}]$
e	Aspect ratio	
f	Frequency	$[\mathrm{s^{-1}}]$
f_1	Horizontal velocity frequency	$[\mathrm{s^{-1}}]$
f_2	Perimeter oscillation frequency	$[\mathrm{s^{-1}}]$
$\mathbf{F}$	Force source term	$[\mathrm{N{\cdot}m^{-3}}]$
$\mathbf{F}_\sigma$	Surface tension source term	$[\mathrm{N{\cdot}m^{-3}}]$
$\mathbf{F}_w$	In-gap wall friction source term	$[\mathrm{N{\cdot}m^{-3}}]$
g	Gas	
$\mathbf{g}$	Gravity acceleration	$[\mathrm{m{\cdot}s^{-2}}]$
h	Gap thickness	[m]
H	Heat capacity	$[\mathrm{J{\cdot}kg^{-1}}]$
$\mathit{\Delta} H_{vap}$	Latent heat of vaporization	$[\mathrm{J{\cdot}kg^{-1}}]$
i	Phase index	
j	Species index	
J	Diffusion flux	$[\mathrm{kg{\cdot}m^{-2}{\cdot}s^{-1}}]$
J'	Evaporation flux	$[\mathrm{kg{\cdot}m^{-2}{\cdot}s^{-1}}]$
K	Mass transfer coefficient	$[\mathrm{m{\cdot}s^{-1}}]$
l	Liquid	
L	Perimeter	[m]
L_{wake}	Wake length	[m]
M	Molar mass	$[\mathrm{kg{\cdot}mol^{-1}}]$
$\dot{m}$	Mass transfer rate	$[\mathrm{kg{\cdot}m^{-3}{\cdot}s^{-1}}]$
n_A	Mass transfer rate	$[\mathrm{mol{\cdot}s^{-1}}]$
p	Pressure	[Pa]
p_0	Pressure at bubble nose	[Pa]
Pe	Peclet number	
p_{mod}	Modified pressure	[Pa]
p_{sat}	Saturated vapor pressure	[Pa]
r	Radius	[m]
r_c	Radius of curvature at the front stagnation point	[m]
R	Universal gas constant	$[\mathrm{J{\cdot}mol^{-1}{\cdot}K^{-1}}]$
R_e	Reynolds number	
$Re(h/d)^2$	Gap Reynolds number	
S	Area	$[\mathrm{m^2}]$
Sc	Schmidt number	
Sh	Sherwood number	

t	Physical time	[s]
T	Temperature	[°C] or [K]
T_{ref}	Reference temperature	[°C] or [K]
$\mathbf{u}$	Fluid velocity vector	[m·s^{-1}]
u_{axis}	Vertical velocity when $y = 0$	[m·s^{-1}]
u_b	Bubble terminal velocity	[m·s^{-1}]
u_x	Horizontal velocity	[m·s^{-1}]
u_{x0}	Horizontal velocity amplitude	[m·s^{-1}]
u_y	Vertical velocity	[m·s^{-1}]
V	Volume	[m^3]
V_{cell}	Volume of the grid cell	[m^3]
W	Cell width	[m]
x	Horizontal position	[m]
y	Vertical position	[m]

2D	Two-dimensional
3D	Three-dimensional
CFD	Computational fluid dynamics
CSF	Continuum surface force
PLIC	Piecewise linear interface construction
PLIF	Planar laser-induced fluorescence
PIV	Particle imaging velocimetry
SIMPLE	Semi-Implicit-Method for Pressure Linked Equations
SLIC	Simple linear interface construction
UDF	User-defined function
VOF	Volume of fluid

Contents

Chapter 1

General Introduction

In this chapter, a brief introduction to the research topics, outline of the project and the structure of the thesis is presented.

1.1 Introduction

1.1.1 Gas injection in pyrometallurgical processes

The injection of gas into liquid metals is widely used in pyrometallurgical processes such as nickel and copper converting, steelmaking, and chloride fluxing of aluminum (Figure 1.1). Diverse needs can be achieved by these gas injection steps, for example, fluxing a chlorine and nitrogen gas mixture through the liquid aluminum for degassing, removal of impurities like magnesium, nonmetallic inclusions and alkali metals [1]. In steelmaking, gas injection is applied to enhance reaction rates, eliminate thermal and compositional gradients and to remove nonmetallic inclusions [2].

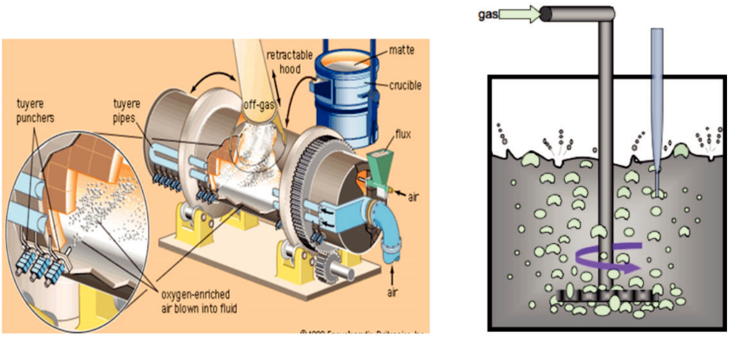

(a) (b)

Figure 1.1: Typical gas injection systems in pyrometallurgy. (a) copper converting[1]; (b) chloride fluxing of aluminum[2].

Gas injection may be achieved with different types of injection devices such as tuyeres, porous plugs, or a lance, and the gas may be blown from the top, side or bottom of the furnace. Upon injection, buoyancy-driven gas bubbles are dispersed within a continuous liquid phase. The high surface area-to-volume ratio of the bubbles greatly increases the gas/liquid contact area and provides excellent mass and heat transfer characteristics at the gas/liquid interface. Meanwhile, the bubble column has the advantages of easy construction, low cost and simple operation [3].

---

[1] http://www.dundeeprecious.com/files/images/projects/pierce_smith_furnace.jpg

[2] http://www.autumnfjeld.com/autumnfjeld/wordpress/wp-autfiles/old_silly_site/files/AutumnResearchMar16.pdf

Despite the widespread industrial applications, the detailed understanding of the fluid mechanics prevailing in bubble column reactors is unfortunately still lacking [4]. The performance of the bubble column reactor relies on the combined outcome of multiphase fluid dynamics, interfacial mass transfer and chemical reactions (when the gas is reactive). The bubble column reactors cover a wide range of spatial scales which span about 7 orders of magnitude (Figure 1.2). It would be a difficult task to understand the details at all scales within and surrounding the bubble. The current work focuses on the phenomena on the meso-scale due to the following reasons [5]: (1) the meso-scale is the most informative scale to understand the whole range of scales, and it is the bridge between the micro-scale nature and the macro-scale appearance; (2) in-depth understanding of the meso-scale structure is critical to scale-up of real size reactors, and (3) the meso-scale structure is still a common challenge, its effects on the flow, heat/mass transfer have not been understood well and literature shows striking differences.

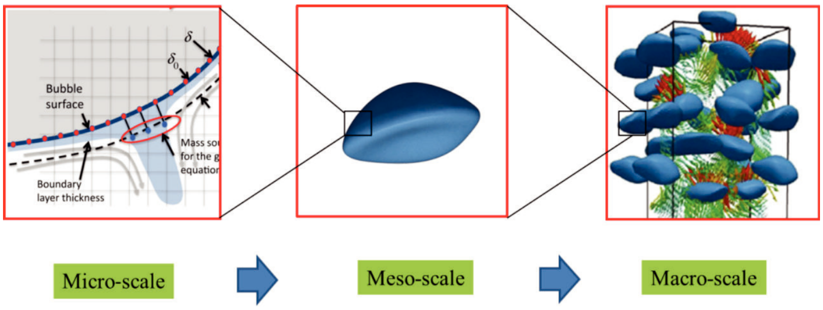

Figure 1.2: Multi-level modelling of bubble column reactors [6, 7].

1.1.2 Silicon tetrachloride injection in liquid zinc

Silicon tetrachloride gas injection in liquid zinc is an ideal case study of gas injection into melts. The characteristics of this process are that $SiCl_4$ gas is injected into liquid zinc at operating temperatures above the boiling point of $ZnCl_2$ (732°C) but below the boiling point of liquid zinc (906°C), and Si particles are formed due to reductive reactions (see Appendix A for the physical properties of $SiCl_4$-Zn system). Ideally, a temperature between 850-880°C is preferable to keep the zinc vapor pressure high. The phenomena accompanied with $SiCl_4$ bubble rise are illustrated in Figure 1.3. During the bubble rise, the reduction can take place at the gas-liquid interface and in the bulk of the bubble due to the evaporation of liquid zinc into the bubble. Correspondingly, solid silicon is generated in the bulk gas phase or at the bubble interface. It can dissolve in the liquid zinc and float at the top of the liquid melt due to density difference. Therefore, a complete description of the system should include mass transfer of evaporation, gas-gas reaction, gas-liquid reaction and dissolution, also their interaction with bubble dynamics and the corresponding heat transfer.

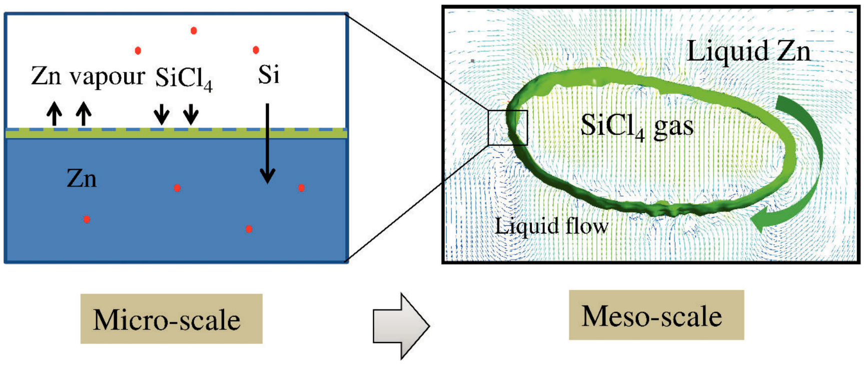

Figure 1.3: Illustration of $SiCl_4$(g)-Zn(l) system at micro- and meso-scales.

Even at the meso-scale, it is impossible to study all these phenomena in one model. Further simplification of the situation is necessary. From literature, it was found that the reaction mostly proceeds under the gaseous state of $SiCl_4$ and Zn [8], which means the gas-liquid reaction can be reasonably neglected. Meanwhile, the bubble lifetime is measured in seconds, which is very short. It is very difficult to track the Si particle on this small time scale. The Si can exist in the gas phase due to formation, dissolve in the liquid phase, or remain in the suspension as aggregate. Its existence changes continuously during the whole injection process which lasts for hours. Therefore, the focus of the present study is on the bubble dynamics and mass transfer due to evaporation at meso-scale.

1.2 Objectives of the thesis

The main objective of the present study is to develop a numerical model to predict qualitatively and quantitatively the bubble dynamics of a gas bubble and the associated liquid evaporation into the gas bubble. The choice for a numerical simulation study was made based on the fact that the experimental measurement of detailed bubble flow properties is difficult due to the opacity of liquid metal and high temperature characteristics. In this study, the simulation is not directly focused on the gas bubble in liquid metal, instead, liquid water will be used due to its similar hydrodynamic properties, its ease of handling and its availability of the quantified liquid characteristics. Therefore, the following objectives will be pursued:

(1) To simulate numerically the two-dimensional bubble dynamics, to discover the characteristics of the bubble properties such as bubble shape and bubble terminal velocity, extracting the liquid flow properties, such as liquid velocity and liquid vorticity.

(2) To validate the simulated bubble dynamics quantitatively with our own experiments and available literature.

(3) To couple the evaporation-induced micro-scale interface mass transfer with phase change into the meso-scale bubble dynamics.

(4) To investigate the parameter effects on the liquid evaporation-induced bubble growth numerically, also the interplay of bubble dynamics and bubble evaporation on the bubble behavior.

1.3 Outline of the thesis

Two numerical models were developed, the first is the two-dimensional bubble dynamics model, and the second is the two-dimensional bubble dynamics and evaporation model. Chapters 3–5 are on the description of the first model and experimental validation. Chapter 6 is devoted to the second model.

Chapter 2 involves a review of some important aspects of bubble dynamics and bubble mass transfer related to this study. A brief review on the bubble dynamics and mass transfer in liquid metal and in liquid water in both three- and two-dimensions is provided. Both experimental observations and numerical simulations are presented.

Chapter 3 is concerned with the model development and the numerical solution methods. A detailed description of the governing equations is presented and the numerical schemes employed to solve them are introduced. As a test, the model is developed to simulate the bubble dynamics of a nitrogen gas bubble ($2 \leqslant d \leqslant 25$ mm, d bubble diameter) in liquid water in a narrow cell (Figure 2.8, cell width $W = 5$ cm) at room temperature. The averaged properties of bubble shape, bubble path, bubble terminal velocity, as well as the secondary motion of shape oscillation and horizontal vibration, are simulated and compared with our own experimental measurements.

Chapter 4 discusses the effects of gap thickness on the bubble dynamics and presents the bubble flow properties as a function of the gap thickness. Meanwhile, the coupling of pressure distribution and velocity distribution in the wake is discussed based on the simulated results.

Chapter 5 further extends the studies to a wide cell with an aim to provide a quantitative simulation of the bubble wake. The general velocity coefficient and dependency on gap thickness are found. The simulation shows a quantitative agreement with experiments performed by Roig *et al.* [9].

Chapter 6 presents a numerical study of bubble dynamics and evaporation. In this study, numerical investigations are conducted into the bubble growth of a two-dimensional nitrogen bubble in water at higher temperatures which is below the liquid boiling point. The model is based on the coupling of the interface mass transfer and bubble dynamics. The effects of bubble size, shape oscillation, temperature and evaporation coefficient on mass transfer rate at gas/liquid interface are discovered.

Chapter 7 summarizes the major conclusions and discusses some suggestions and recommendations for future work.

Chapter 2

Literature Review

This chapter gives a comprehensive literature review on bubble dynamics and mass transfer in liquid metal and water, in both two- and three-dimensions. The numerical simulation methods available for bubble dynamics and mass transfer are also discussed, together with their applications.

2.1 Experimental work

2.1.1 Bubble dynamics and mass transfer in liquid metal

Bubble dynamics

In the study of mesoscopic bubble dynamics, the overall bubble flow properties such as bubble shape, bubble trajectory and bubble terminal velocity are important for stirring and mass transfer. Meanwhile, the details of the gas circulation inside the bubble and the bubble-induced liquid flow in the bubble wake are indispensable for a full understanding of the complex two-phase flow and mass transfer. However, in the studies of single bubble behaviour in liquid metal, progress is quite slow due to the difficulty in conducting experiments at high temperatures and due to the opacity of the melt.

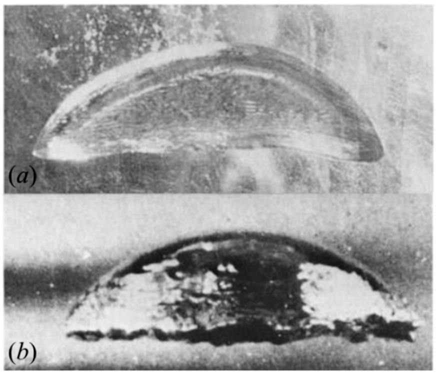

Figure 2.1: Spherical-cap bubbles in mercury and water. (a) A two-dimensional argon bubble (base 8 cm) rising in mercury [10]. (b) A nitrogen bubble (base 7.3 cm) rising in a column of water [11].

In the 1960s, Davenport and his colleagues carried out experiments on large spherical-cap bubbles rising in mercury and silver in both three-dimensional columns [10] and semi-two-dimensional columns [12]. The bubble shape and rise velocity were detected. In the three-dimensional experiments, the bubble shape was measured by means of electrical probes. For a direct visualization of the bubble interface, semi-two-dimensional experiments were carried out. Also in 1968, Schwerdtfeger measured the argon bubble velocities in a three-dimensional liquid mercury column with an ultrasonic pulse-echo instrument [13]. Though these experiments are nearly 50 years old and the measurements are rough, they obtained very important information on the bubble shape and bubble terminal velocity in liquid metal.

The shapes of spherical-cap bubbles observed by Paneni & Davenport [12] are similar in thin sheets of water and mercury (the sheets are wide enough that the bubbles in both cases do not touch the walls), except that the higher surface tension of mercury increases the radius of curvature at the bubble's trailing edge (Figure 2.1). They also found that shapes are similar in two-dimensional and three-dimensional systems. For the bubble rise velocity, Davenport *et at.* [10] found that the velocities of bubbles rising in mercury and in water are similar (bubble diameter $10 < d < 48$ mm). The measured velocity is smaller than the theoretical expression of $u_b = 0.67(\mathrm{g}r_c)^{0.5}$ or $u_b = 1.02(\mathrm{g}r)^{0.5}$ (EQ. (8.3.6) in Figure 2.2a. u_b bubble terminal velocity, g gravity acceleration, r_c radius of curvature, and r bubble radius). The constricting effects of the walls in the experiments attribute to the reduced terminal velocity. In Schwerdtfeger's study, smaller bubble sizes were studied ($2 < d < 15$ mm). The terminal velocities in liquid mercury and in liquid water still show similarities (Figure 2.2b) [12].

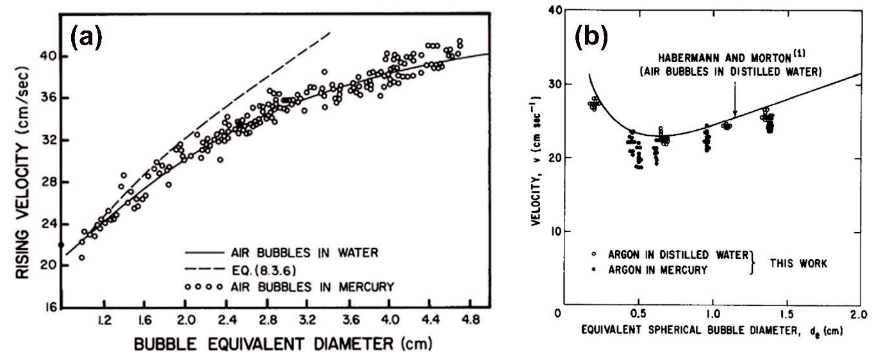

Figure 2.2: Rising velocities of bubbles in water and in mercury. (a) Velocities of spherical-cap air bubbles rising in mercury and in water [10]. (b) Velocities of small argon bubbles in mercury and distilled water at room temperature [13].

The recent study on bubble dynamics in liquid metal can be divided into two categories, one about liquid velocity measurements, the other related to visualization of the bubble contour:

(1) Liquid velocity measurements

The techniques of local and instantaneous measurements in liquid metals are known to be much more difficult than in classical transparent fluids like water and air [14]. The conventional measuring techniques used for ordinary flows include

(a) flow visualization, (b) measurement of velocities with differential pressure, (c) electromagnetic velocity measurement, (d) hot wire and hot film anemometry, (e) laser-Doppler velocimetry and (f) ultrasound Doppler velocimetry [15]. Most of the methods fail in liquid metal flows, or their applicability is strongly limited [14]. The application of ultrasound Doppler velocimetry to liquid metal flows has been found promising. Reliable results were obtained in liquid mercury, gallium and eutectic alloy GaInSn at low temperatures. The range of applicability has been extended to flows of liquid sodium(150°C), to PbBi bubbly flow (180–300°C) and CuSn flow at temperatures of about 620°C [16]. However, due to the lacking of bubble shape and path, reconstruction of bubble wake structure is difficult.

(2) Visualization of bubble contour

Table 2.1: Comparison of bubble visualization techniques in liquid metal [17–19].

Category	Methods	Advantage	Disadvantage
Direct Visualization	○ X-ray photography	○ Fast data collection	○ Expensive to operate
	○ Neutron radiography	○ Graphical ○ Non-contact	○ Strong attenuation
Indirect probe measurement	○ Thermal sensor	○ Simple design	○ Slow response
	○ Electric resistivity sensor	○ Durable	○ Low accuracy
	○ Capacitance probe		○ Contacting liquid

The measurement techniques that can be used to visualize the bubble in liquid metal in three-dimensions are summarized in Table 2.1. These techniques fall under two general categories, namely direct visualization techniques and indirect probe measurements [17]. The optical approach is widely used in water-based systems, however, optical techniques cannot work in liquid metals because visible light cannot be transmitted in liquid metals. Therefore, radiographic imaging such as X-rays and neutron beams is needed. In the second category, the property differences between the gas phase and the liquid phase are exploited. These include electrical properties, thermal conductivity and mechanical properties. Among all these techniques, high energy X-rays and electroresistivity probe attract more attention. However, these two methods are not able to provide accurate information on the bubble shape. The bubble contour obtained by the electric probe is composed of a limited number of vertical cross sections, resulting in a low resolution and large error (Figure 2.3a). The image by radiography can provide a better quality, however, the bubble shapes show a jagged interface due to image noise (Figure 2.3b). Another limitation for radiography is that the size of the container is limited due to severe light attenuation. The thickness of the tank used in [19] is 30 mm. None of these techniques are applicable to small bubbles since the dimensions become comparable to the resolutions.

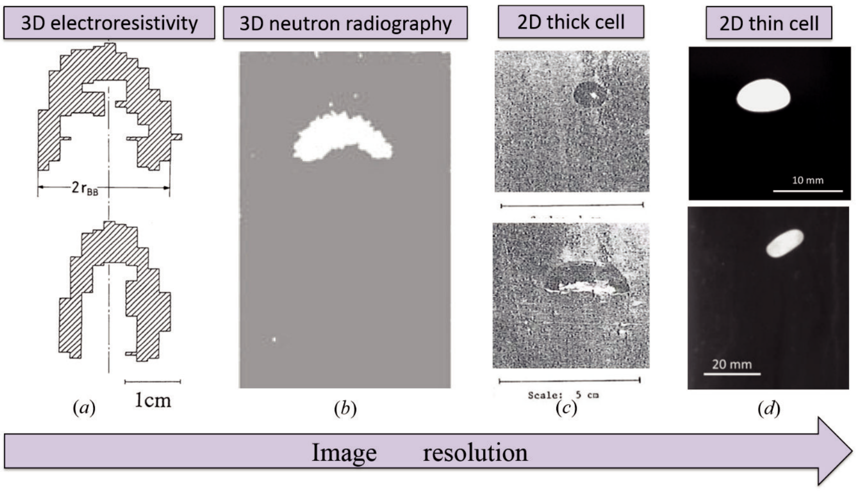

Figure 2.3: Comparison of the images captured by different techniques. (a) Two successively rising bubbles with multineedle electroresustivity for Wood's metal-He system [18]. The 3D experiment was carried out in a cylindrical test vessel wih an inner diameter of 200 mm and a height of 300 mm. (b) A spherical cap water vapor bubble in a liquid Pb-Bi alloy with high-frame-rate neutron radiography [19]. The 3D rectangular dimensions are 400 mm height, 80 mm width and 30 mm thickness. (c) Air bubbles in mercury under semi-two-dimensional flow conditions, in a thin sheet of 800 mm high by 300 mm wide and 4.7 mm thick [12]. (d) Two nitrogen bubbles in liquid mercury (upper one) and in liquid zinc (lower one) in a Hele-Shaw cell with dimensions of 450 mm height 50 mm width 1.0 mm thickness, and 490 mm height 95 mm width 1.5 mm thickness, respectively [20].

To overcome the three-dimensional visualization difficulties and to provide high resolution of bubble contours, very recently in 2014, Klaasen *et al.* [20] tried to confine the bubble in two-dimensions in a Hele-Shaw cell. The cell is composed of two parallel transparent walls separated by a small gap. The thickness of the gap is 1.0 or 1.5 mm, which is much smaller than that of Paneni and Davenport (1 cm) [12]. Together with a proper non-wetting transparent wall, the bubbles in liquid mercury (room temperature) and liquid zinc (700°C) were visualized with ease by a high-speed camera. Through the comparison of the bubble contours obtained by the above mentioned experiments (Figure 2.3), it is apparent that, in the near future, the two-dimensional technique has the advantage of providing more details on the bubble dynamics as well as on the mass transfer without the difficulties present in the three-dimensional observations.

Mass transfer

The studies on bubble mass transfer in liquid metal are very few. For the liquid-side mass transfer coefficient, Davenport *et al.* measured the mass transfer coefficient of large spherical-cap bubbles in three dimensions by pressure change [10]. The rates of absorption of oxygen by liquid mercury and molten silver have been interpreted [10]. The measured overall mass transfer coefficient of oxygen into mercury K_l is 0.055 cm·s^{-1}, into liquid silver is 0.036 ± 0.007 cm·s^{-1} (1000°C). Although the error for measurement in the liquid metal was estimated to be ±30–40%, the detected liquid-side mass transfer coefficient is similar to that of CO_2-H_2O system (The overall mass transfer coefficient of about 0.026 cm·s^{-1} was observed for CO_2-H_2O system at 15°C). The mass transfer coefficient was estimated by $K_l = 0.82r^{-0.25}D^{0.5}g^{0.25}$ (K_l liquid phase mass transfer coefficient, D diffusion coefficient). For gas-side mass transfer, the studies are only on the macro-scale mass transfer coefficient (K_gA) where interface mass transfer area A is unknown [21, 22].

In conclusion, a full understanding of mesoscopic bubble dynamics in three-dimensions is still lacking due to poor image resolution, while a two-dimensional visualization can provide more details. The available studies confirm that the bubble dynamics and mass transfer coefficient are similar in liquid metal and in liquid water due to similar mass and momentum transport properties. Therefore, it is possible to use a water model to simulate the liquid metal situation based on the similarity criteria.

2.1.2 Bubble dynamics and mass transfer in liquid water

Unlike the slow progress of the bubble dynamics in liquid metal, numerous studies of bubbles in liquid water have been carried out since the 1950s. No attempt has been made to provide a complete list of the available experimental techniques and results in literature. The works by Davies & Taylor [23], Davenport [24], and Clift, Grace & Weber [25] provide a guide to the underlying theory of the fluid dynamics associated with bubbles moving in a liquid medium. The reviews can be found elsewhere [26, 27]. Here a short review on bubble dynamics and mass transfer is presented.

Dimensionless parameters

In general, a gas bubble rising in an infinite liquid medium is dependent on the physical properties of the surrounding fluid. These properties include the density of liquid phase ρ_l, the density of gas phase ρ_g, the viscosity of liquid phase μ_l, the viscosity of gas phase μ_g, the surface tension σ, equivalent diameter of the gas bubble d. The three-dimensional bubble diameter d is defined by:

$$d = 2\left(\frac{3V}{4\pi}\right)^{1/3} \tag{2.1}$$

where V is the bubble volume. The two-dimensional bubble diameter d is defined by:

$$d = 2\left(\frac{S}{\pi}\right)^{1/2} \tag{2.2}$$

where S is the bubble area in the plane.

The consideration of gas phase density and viscosity is normally ignored due to small values compared to that of the liquid phase. Besides these properties, the bubble terminal velocity u_b is also an important parameter though it is not independent.

The following dimensionless parameters are used to describe the bubble dynamics:

Reynolds number:

$$Re = \frac{\text{inertial force}}{\text{viscous force}} = \frac{\rho_l u_d d}{\mu_l} \tag{2.3}$$

Eötvös number:

$$Eo = \frac{\text{buoyancy force}}{\text{surface tension force}} = \frac{\rho_l g d^2}{\sigma} \tag{2.4}$$

Weber number:

$$We = \frac{\text{inertial force}}{\text{surface tension force}} = \frac{\rho_l u_b^2 d}{\sigma} \tag{2.5}$$

Morton number:

$$Mo = Eo\frac{We^2}{Re^4} = \frac{g\mu_l^4}{\rho_l \sigma^3} \tag{2.6}$$

Drag coefficient:

$$C_D = \frac{We}{Eo} = \frac{4gd}{3u_b^2} \tag{2.7}$$

Similarly, for gas bubble mass transfer, except for the above mentioned physical properties, the diffusion coefficient D and mass transfer coefficient K are also important. The mass transfer coefficient K is defined as:

$$K = \frac{n_A}{A\Delta c_A} \tag{2.8}$$

where n_A is the mass transfer rate; A is the mass transfer area; Δc_A is the driving force concentration difference.

The corresponding dimensionless numbers include:

Schmidt number:

$$Sc = \frac{\text{viscous diffusion rate}}{\text{mass diffusion rate}} = \frac{\mu}{\rho D} \tag{2.9}$$

Péclet number:

$$Pe = \frac{\text{convective transport rate}}{\text{diffusive transport rate}} = Re \cdot Sc \tag{2.10}$$

Sherwood number:

$$Sh = \frac{\text{convective mass transfer coefficient}}{\text{diffusive mass transfer coefficient}} = \frac{Kd}{D} \tag{2.11}$$

Bubble shape

The shape of a rising bubble is determined by the pressure distribution along the interface layer and the shape is therefore defined by the mutual interaction of surface tension, viscosity, buoyancy and inertial forces [27]. Clift *et al*. [25] provided a graphical correlation of the shapes of bubbles and drops in terms of Re, Eo and Mo (Figure 2.4).

For a gas bubble in liquid water, the physical properties of density, kinematic viscosity and surface tension are constant, the bubble shape is therefore mainly dependent on the bubble size. The Morton number of water is 10^{-11}, which is very close to the liquid metal Morton range of $10^{-11.8}$-$10^{-13.8}$ [20]. Therefore, the bubbles can be grouped in the following three categories [28]:

(a) Spherical bubbles

In this category, the bubble size is very small. They are approximated by a spherical shape in the low Reynolds number range, and they rise in a rectilinear path.

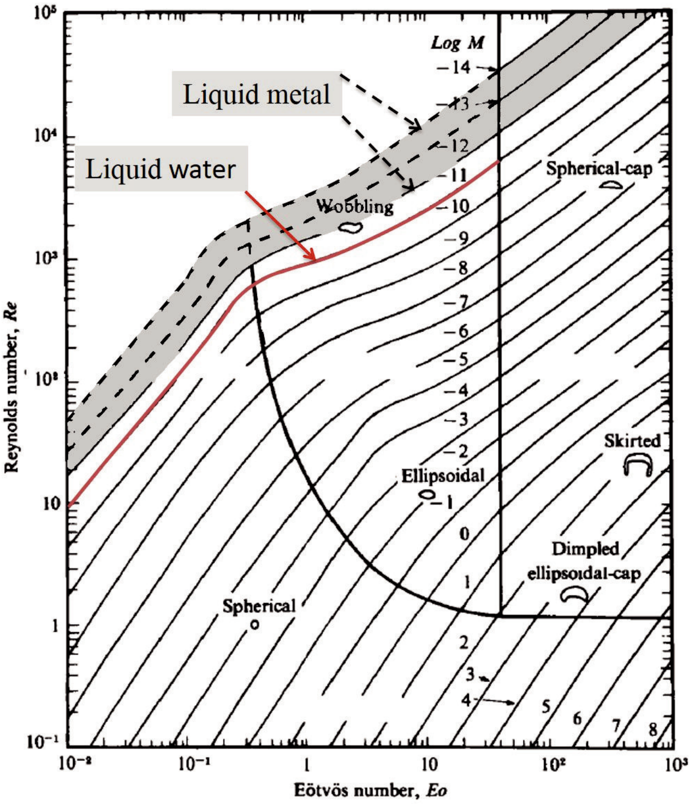

Figure 2.4: Shape regimes for bubbles and drops in unhindered gravitational motion through liquids [25].

(b) Ellipsoidal bubbles

In this case, the bubble size is intermediate. They can take a variety of shapes except for an ellipsoidal shape. The bubbles show two types of secondary motion including shape oscillation and path instability.

(c) Spherical-cap bubbles

With a further incease of the bubble size, the shape of the bubbles in this range can be closely approximated with a spherical cap upper surface and a flat base. In the case of large bubbles, the effects of surface tension and viscosity are negligible and the rise velocity is given by the equation of Davies and Taylor [23].

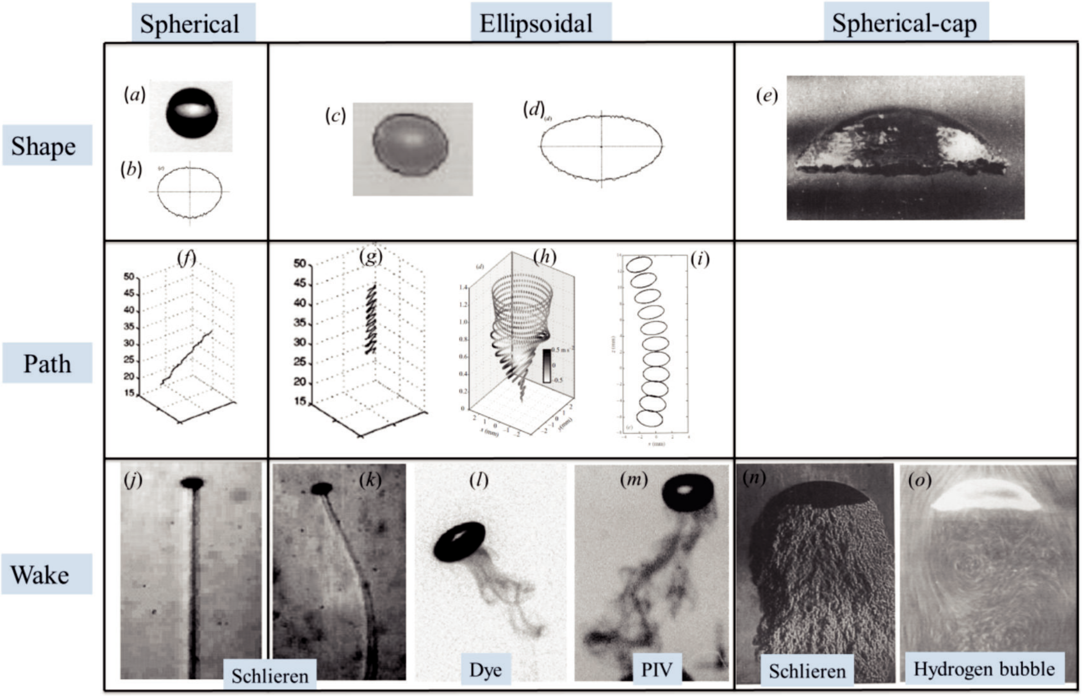

Figure 2.5: Experimental studies of bubble shape, bubble path and bubble wake in the literature. For bubble shape, (a) $d = 1.74$ mm [29]; (b) $d = 1.28$ mm [30]; (c) $d = 2.48$ mm [31]; (d) $d = 1.82$ mm [30]; (e) $d = 42$ mm [25]. For bubble path, (f) $d = 1.37$ mm [29]; (g) $d = 1.52$ mm [29]; (h) $d = 2.24$ mm [32]; (i) $d = 2.48$ mm [31]; (j) $d = 1.58$ mm [33] (k) $d = 2.02$ mm [33]. (l) d lies in 0.66–0.93 mm in silicone oil [34]. (m) d lies in 4–8 mm, $Re = 1500$ [35], (n) $d \approx 45$ mm [36], (o) d (unknown) [37].

The typical bubble shapes for the three types of bubbles are shown in Figure 2.5a–e. Saffman [38] found that the transition size from the spherical bubble to ellipsoidal bubble in tap water is $d = 1.4$ mm, while the value is $d = 1.8$ mm in pure water by Duineveld [30] and $d = 1.7$ mm in pure water by Wu & Gharib [29]. The differences in the above studies demonstrated that the onset of the shape change is very complicated and dependent on the physical properties and contamination.

Terminal velocity

Terminal velocity of gas bubbles is one of the parameters, which determines the gas phase residence time and hence the contact time for the interfacial transport and subsequently contributes to the performance of the equipment [26]. The terminal velocities of gas bubbles in pure liquid water and in water with surfactants have been studied widely, and it was found that surface-active contaminants affect the terminal velocity most strongly in the ellipsoidal regime [25]. For this reason, the experimental results are scattered (Figure 2.6a). The effects of contamination are beyond our scope, therefore, a general introduction of the bubble terminal velocity in pure water is introduced.

In 1967, Mendelson summarized the characteristics of the terminal velocity (Figure 2.6b) and subdivided the curve into four regions [39]:

Region 1: $d < 0.7$ mm (radius < 0.035 cm)

In this region, Stokes derived the correlation resulting from force balance on very small bubbles in a quiescent liquid [26]. Under the assumption that the bubbles do not have any internal circulation and no slip at the interface, the terminal velocity obeys Stokes' law:

$$u_b = \frac{\mathrm{g}\rho d^2}{18\mu} \tag{2.12}$$

Region 2: $0.7 < d < 1.4$ mm ($0.035 <$ radius < 0.07 cm)

In this region, the internal circulation reduces the shear stress at the interface and the rise velocity is greater than predicted by Stokes' law.

Region 3: $1.4 < d < 6$ mm ($0.07 <$ radius < 0.3 cm)

In this region, Mendelson predicted the bubble terminal velocity from wave theory (the bubbles are assumed interfacial disturbances, and their terminal

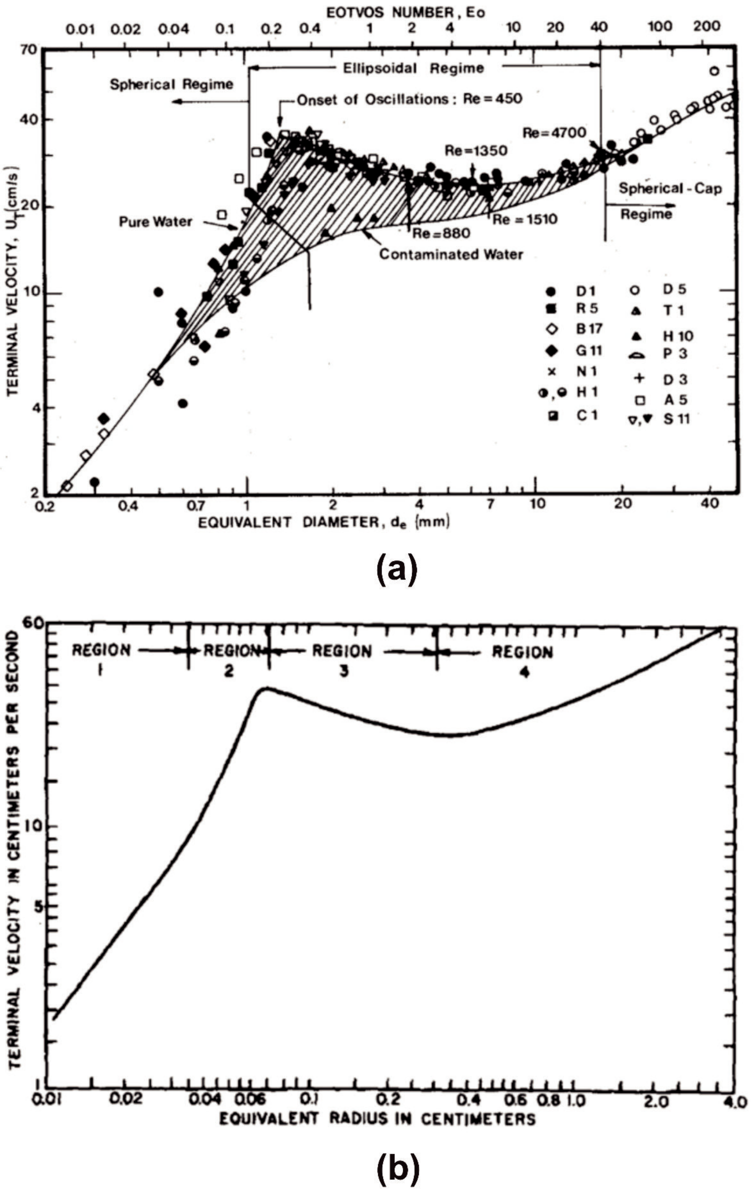

Figure 2.6: Terminal velocity of bubbles in water from different resources. (a) Terminal velocity of air bubbles in water at 20°C [25]. (b) Typical curve of the terminal velocity of bubbles as a function of bubble size in a low viscosity liquid [39].

velocity is similar to those of waves on an ideal fluid) by:

$$u_b = \sqrt{\frac{2\sigma}{\rho_l d} + \frac{\mathrm{g}d}{2}} \tag{2.13}$$

Despite of the lacking of solid physical explanation Mendelson's relation in Region 3 can fit the experimental data very well. Recently, new correlations have been proposed [40, 41], however, they are more complicated and less popular.

Region 4: $d > 6$ mm (radius > 0.3 cm)

The velocity of a spherical cap bubble is described by Davies and Taylor [23] as:

$$u_b = 0.67\sqrt{\mathrm{g}r_c} \quad \text{or} \quad u_b = 1.02\sqrt{\mathrm{g}r} \tag{2.14}$$

where r_c is the radius of curvature at the front stagnation point, r the equivalent radius of the bubble.

The corresponding correlations for drag coefficient can be found in [26] but it is not treated in this part.

Bubble path

Different bubble shapes give rise to different bubble paths, this can lead to different liquid flow and mixing situation. In general, for a spherical bubble, a rectilinear path is recognized, while the ellipsoidal bubble has an oscillating path. The path can be either zig-zag or spiral (Figure 2.5). For a spherical-cap bubble, the bubble takes a rectilinear path again. However, Wu & Gharib [29] found the critical bubble diameter for shape transition from spherical to ellipsoidal to be 1.7 mm, while the critical bubble diameter for path transition from rectilinear to zig-zag is 1.5 mm (Figure 2.5g). This means that the formation of the zig-zag path is complicated and not only dependent on the bubble size. It was found that wake instability plays a central role in path instability [33].

Bubble wake

Unlike the gas bubble in liquid metal, the bubble wake behind the gas bubble in liquid water can be visualized by different types of techniques, such as Schlieren [33], dye [34], particle imaging velocimetry (PIV) [35] and small hydrogen bubbles [37] (Figure 2.5). Their wake structure also varies with the bubble type. The instability of the bubble wake can explain the unsteady bubble path. However, the interaction of these three parameters of bubble shape, bubble path and bubble wake are very complicated. In the studies of bubble wake, PIV has the ability to provide local liquid velocity and vertical structure, which has been applied to the ellipsoidal bubble. However, similar to the studies of bubble path, the wake structure of the spherical-cap bubble was studied some years before [36, 37], and these studies are not sufficient to discover the onset of the wake change from laminar to turbulent.

Mass transfer

- Liquid-phase mass transfer

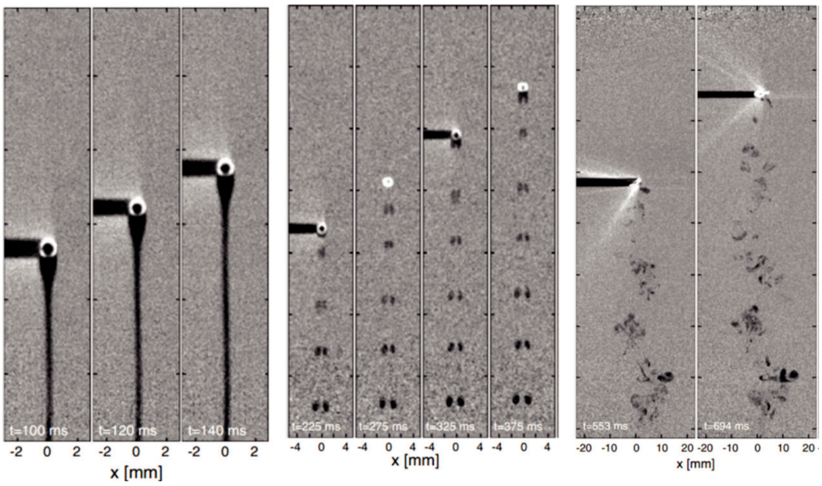

(*a*) (*b*) (*c*)

Figure 2.7: The experimental studies of bubble mass transfer in the wake for different diameters [42]. (a) $d = 1.1$ mm; (b) $d = 1.5$ mm; (c) $d = 4.4$ mm.

A complete literature review of liquid-side mass transfer coefficients is given in Clift's book " Bubbles, Drops, and Particles" [25]. Others who have tried to study more practical cases have ended up with empirical correlations which are limited to special circumstances. It is worth mentioning that, due to the improvement of the techniques, the local mass transfer around a single bubble can be visualized by a planar laser-induced fluorescence (PLIF) technique [42], and the spatio-temporal dynamics of mass transfer has been visualized, as shown in Figure 2.7. The bubble with diameter $d = 1.1$ mm rises rectilinearly, the dissolved CO_2 accumulates in a region directly behind the bubble and extends further in a straight line (Figure 2.7a). The mass transfer of a zigzagging bubble ($d = 1.5$ mm) is associated with the trailing vortices in the wake (Figure 2.7b), and the mass transfer becomes irregular for a bigger bubble size of $d = 4.4$ mm (Figure 2.7c). This represents a great progress in understanding the mass transfer details in the wake.

- Gas-phase mass transfer

The gas-phase mass transfer was also reviewed in Clift's book [25]. The gas-side transfer coefficient is greatly dependent on two factors: (1) whether the gas inside the bubble is stagnant or circulating; (2) whether the bubble is oscillating or not [25]. The analytical solutions for (1) are only available for spheres in creeping flow (Reynolds number $Re \ll 1$). Newman [43], Kronig [44], Johns and Beckmann [45], Watada *et al.* [46] contributed to the solutions of different Peclet number, and most of the results come from drops instead of bubbles. For the situation of (2), there are studies for droplets. It has been proven by drop oscillation that the oscillations are sufficiently strong to promote vigorous internal mixing. When the bubble is oscillating, the effects of oscillation on the gas phase mass transfer are still unknown.

Compared with the liquid-phase mass transfer, measurements of the global gas-phase mass transfer are difficult due to the following reasons [47]: (1) When gas phase resistance is controlling, the mass transfer rate is much higher than in the case of liquid phase (the diffusion coefficient in gas phase is in the order of 10^{-5} m^2/s, while in liquid phase 10^{-9} m^2/s). (2) Bubble internal flow is difficult to capture, so it is difficult to determine the effect on mass transfer rate. (3) Accurate bubble mass transfer time is hard to determine. Direct visualization of the local concentration inside the gas phase as in the liquid phase is even more challenging.

There are two good reports on the dispersed gas phase mass transfer in bubbles: (1) Filla (1975) [47] measured the gas phase mass transfer coefficient K_g in slug flow (it is characterised by the motion of large capsule-shaped bubbles, frequently referred to as Taylor bubbles or gas slugs, almost filling the tube separated from the wall of the tube by a liquid film and separated from each other by liquid plugs [48]). In order to minimize absorption during formation and surfacing, the bubble was injected through a liquid of three immiscible layers. Only the middle layer absorbs the solvent. The solvent used was NH_3, the three layers were mercury, tap water and paraffin oil. The absorbed NH_3 was measured by titration. The concentration of NH_3 in the slug was not provided, but from the information that the slug volume was assumed constant, it can be assumed to be very small. The measured K_g ranges from 2–6 cm/s depending on tube dimensions. (2) Zaritzky [49] studied K_g by injecting a single bubble in a column. SO_2 was chosen as solvent gas and a photographic method was used to detect bubble radius change. In his experiment, he assumed bubble volume change was caused by absorption and detected bubble diameter change to calculate K_g. The measured Sherwood number Sh ranges from 14–17.

The above studies only obtained averaged values for overall mass transfer coefficient, and a number of important questions were not addressed. For example, what is the internal circulation inside the gas bubble? Is there any difference for different types of bubbles? What is the effect of shape oscillation on the mass transfer? How about the instantaneous mass transfer coefficient for different types of bubbles? To solve these questions, a numerical method can be helpful.

2.1.3 Bubble dynamics in a Hele-Shaw cell

Direct observation of bubbles is somewhat cumbersome and some of the results could be contradictory due to the complexity in 3D observation, even in water. The difficulty of describing the bubble motion in 3D suggests us to simplify the bubble motion to two dimensions, while keeping high-Reynolds flow properties of the bubble motion. Meanwhile, in two-dimensions, it is easier to observe the shape change due to mass transfer.

For this purpose, a Hele-Shaw cell is introduced as a two-dimensional setup. It is defined as two parallel flat transparent plates that are separated by a very small distance, which was introduced by Hele-Shaw in 1898 [50]. In the space between the plates, a liquid layer is confined and the motion in the direction perpendicular to the cell is limited. The schematic pictures are shown in Figure 2.8. After averaging over the interstice, the liquid layer can be regarded as a two-dimensional bounded domain.

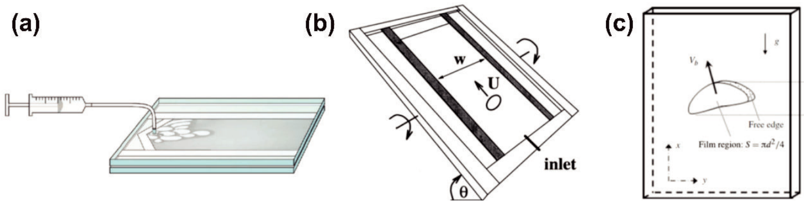

Figure 2.8: Illustrations of various Hele-Shaw cells. (a) A horizontal cell as used for viscous fingering studies [51]. (b) A tilted cell used for bubble dynamics studies [52]. (c) A vertical cell for bubble dynamics studies [9].

The advantages of the Hele-Shaw cell include better visualization, better measurement and simplification of the complex dynamics. The studies of fluid flow in a Hele-Shaw cell can be divided into two types: (1) Viscous fingering in a Hele-Shaw cell. Viscous fingering is generated by displacing a more viscous fluid in a gap of less viscous fluid. The interface is unstable and develops waves out of which a single finger grows. Much work has been done to investigate the shape and stability of the fingers [50, 53]. (2) Motion of bubbles in a Hele-Shaw cell. The studies of motion of bubbles in Hele-Shaw cell can be further subdivided into two categories:

- Bubble flow in viscous liquids

In the early studies, Hele-Shaw cell was used to describe the Stokes flow where advective inertial forces are small compared with viscous forces ($Re \ll 1$). The studies focus on the bubble behaviour in viscous fluids. (The typical viscosity of the fluid is 100 times larger than that of water). Some analytic solutions for the viscous flow in Hele-Shaw cell were obtained by Taylor & Saffman [54] and Tanveer [55]. Systematic experiments on the bubble motion in Hele-Shaw cells were conducted by Maxworthy [56] and Kopf-Sill & Homsy [57].

- Bubble flow in low-viscous liquids

Recently, the importance of the Hele-Shaw cell on high Reynolds number bubble dynamics in low-viscous liquids has been recognized. The bubble motion in water and other low-viscous fluids in a vertical Hele-Shaw cell was studied by Wu (1997) [58], by Kozuka & Kawaguchi (2006-2011) [59–61], by Roig *et al.* (2012) [9] and by Klaasen *et al.* [62, 63]. The main interest lies on the buoyancy-driven bubble flow in a vertical Hele-Shaw cell. The bubble velocity, bubble path and bubble wake can be captured. Their studies provide very important information for the validation of the simulation results. The next three chapters will give a direct and detailed comparison between simulation results and experimental measurements, therefore, the review on the bubble shape, bubble path, as well as bubble wake in a Hele-Shaw cell is omitted here to avoid duplication. A detailed comparison of three-dimensional bubble dynamics and two-dimensional bubble dynamics can be found in the thesis of Klaasen [20], and it was concluded that in both cases paths evolve similarly, and the contours of two-dimensional bubbles largely resemble the projections of the three-dimensional shape of freely rising bubbles.

2.2 Numerical simulation

Due to the increase of the computational power, numerical simulations of two-phase flow and mass transfer can be achieved with quantitative data. In

Table 2.2: Overview of techniques for multi-fluid flows with sharp interfaces [64].

Method	Advantages	Disadvantages
Level-set	Conceptually simple Easy to implement	Limited accuracy Loss of mass (volume)
Shock-capturing	Straightforward implementation Abundance of advection schemes are available	Numerical diffusion Fine grids required Limited to small discontinuities
Marker particle	Extremely accurate Robust Accounts for substantial topology changes in interface	Computationally expensive Redistribution of marker particles required
SLIC VOF	Conceptually simple Straightforward extension to three dimensions	Numerical diffusion Limited accuracy Merging and breakage of interfaces occurs automatically
PLIC VOF	Relatively simple Accurate Accounts for substantial topology changes in interface	Difficult to implement in three dimensions Merging and breakage of interfaces occurs automatically
Lattice Boltzmann	Accurate Accounts for substantial topology changes in interface	Difficult to implement Merging and breakage of interfaces occurs automatically
Front-tracking	Extremely accurate Robust Accounts for substantial topology changes in interface	Mapping of interface mesh onto Eulerian mesh Dynamic remeshing required Merging and breakage of interfaces requires subgrid model

this part, the main focus is on the available numerical methods for gas-liquid multiphase flow, and also on their applications to the bubble dynamics and mass transfer.

2.2.1 Simulation methods

The interface tracking methods include front-tracking methods, shock capturing methods, level-set methods, marker particle methods and SLIC and PLIC volume of fluid (VOF) methods, which are summarized with their advantages and disadvantages in Table 2.2.

Among these methods, VOF methods, Level-set methods and Front-tracking methods are widely used for gas bubble–liquid flow simulation. An introduction to these methods will be given in this section.

VOF methods

Volume of fluid (VOF) methods have been used extensively in the simulation of two phase flow since it was introduced in 1976 by Noh and Woodward [65]. In these methods, the interface is given implicitly by the fraction of volume within each grid cell of one of the fluids. The volume fraction γ is defined as:

$$\gamma \begin{cases} = 1 & \text{phase 1} \\ = 0 & \text{phase 2} \\ 0 < \gamma < 1 & \text{interface} \end{cases} \tag{2.15}$$

The volume fraction is advected by the velocity field by means of:

$$\frac{\partial \gamma}{\partial t} + \nabla \cdot (\mathbf{u}\gamma) = 0 \tag{2.16}$$

The average density, viscosity and other properties in the interface grid cells are calculated by volume fraction. Then the gas-liquid two-phase problem is turned into a one fluid problem (solving a single set of momentum equations). The surface tension could also be calculated by volume fraction in and adjacent the grid cell [66].

Two important classes of VOF methods can be distinguished with respect to the representation of the interface, namely simple linear interface construction (SLIC) and piecewise linear interface construction (PLIC) approach [67]. The difference of the two methods is illustrated in Figure 2.9. The method of PLIC

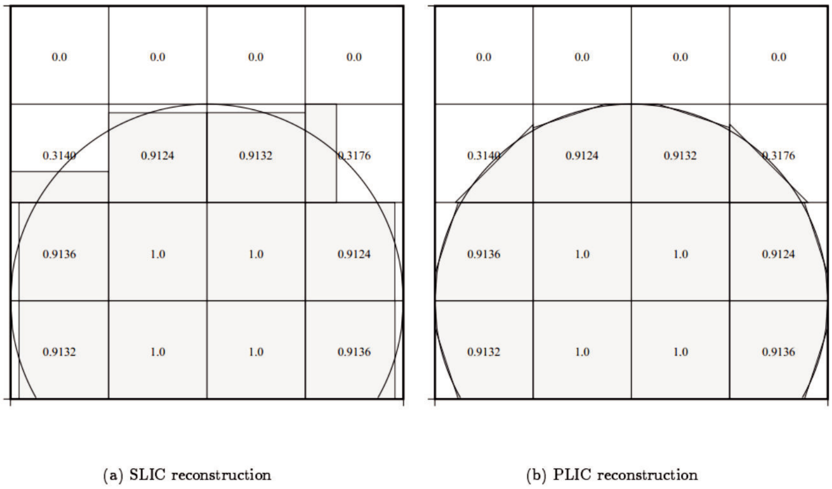

(a) SLIC reconstruction (b) PLIC reconstruction

Figure 2.9: Reconstructed interfaces for a circle using the SLIC and PLIC methods [67].

is more accurate. In PLIC, the interface is approximated by a straight line segment in each grid cell, but the line can be oriented arbitrarily with respect to the coordinate axis. The orientation of the line is determined by the normal to the interface, which is found by considering the average volume fraction of both the grid cell under consideration as well as the adjacent grid cells. The result of the advection generally depends on the accuracy of the interface reconstruction and finding the normal accurately therefore becomes critical for PLIC methods. Given the volume fraction in each grid cell and the normal, the exact location of the interface can be determined. After all, the VOF methods are simple and robust with good conservation properties, suitable for developing complex models.

Level-set methods

The level-set approach was originally introduced by Osher and Sethian (1988) to simulate the motion of an incompressible two phase flow [68]. The level-set method uses a distance function to capture the gas-liquid interface on the fixed Eulerian grid. In two-dimensions, the distance function $\phi(x, y, t)$ describes the distance from location (x, y) to the gas-liquid interface at time t. In the level-set method, the interface Γ is the zero level-set of a ϕ function:

$$\Gamma = \{(x, y \mid \phi(x, y, t)) = 0\} \tag{2.17}$$

The level-set function is considered to be positive in one phase and negative in the second phase (Figure 2.10). Therefore,

$$\phi(x, y, t) \begin{cases} > 0 & \text{phase 1} \\ = 0 & \text{interface} \\ < 0 & \text{phase 2} \end{cases} \tag{2.18}$$

The evolution of ϕ is governed by a transport equation:

$$\frac{\partial \phi}{\partial t} + \mathbf{u} \cdot \nabla \phi = 0 \tag{2.19}$$

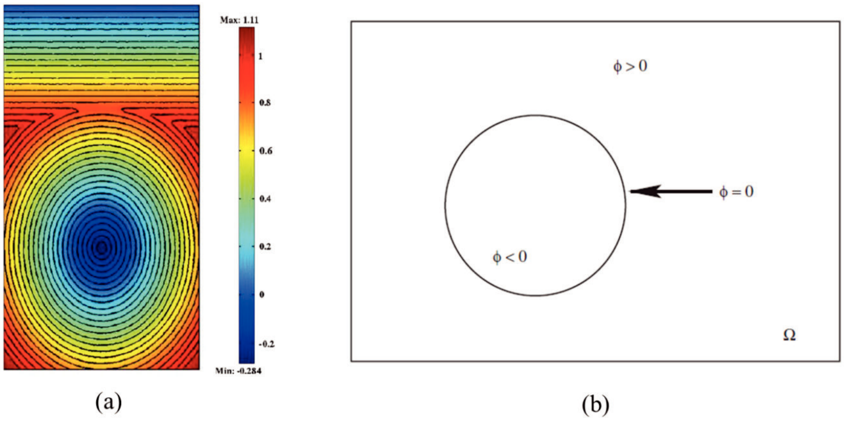

Figure 2.10: Illustration of the level-set function. (a) A contour plot of the initial conditions of the level-set function for different level sets [69]. (b) Characteristics of the level-set function indicating that the level-set function carries positive value in the continuous phase, negative value in the dispersed phase, and is equal to zero at the interface [69].

Level-set methods could automatically deal with topological changes and it is in general easy to obtain high order of accuracy. However, one of the drawbacks of level-set methods is that they are not conservative. Even if the initial value of the level-set function ϕ_0 is set to be the distance function, the level-set function may not remain as a distance function at $t > 0$ when the advection equation is solved for ϕ [70]. Thus a reinitialization scheme is needed to keep the zero level-set to be the location of the gas-liquid interface. Deshpande and Zimmerman found in their two-dimensional drop dynamics that after incorporating re-initialization of ϕ, there is still a 9% loss in the cross-sectional area of the droplet, but is better than the 32% loss in the same without re-initialization of ϕ [69].

To solve the question, some researchers tried to combine the VOF methods and level-set methods to find a conservative method [71, 72]. Besides, Enright *et al.* [73] presented an efficient semi-Lagrangian based particle level-set method for the accurate capturing of an interface. The method can have better conservation properties compared to the level-set method.

Front-Tracking methods

The group of Tryggvason has developed a CFD code for numerical simulation of three dimensional gas bubbles based on an Euler-Lagrange approach, which is called Front-Tracking method [74].

The Front-Tracking method is developed from Marker in Cell methods, which set some massless maker-particles in the initial interface, and update the location of markers with flow. The connected marker points can be used to track the boundary between different fluids or phases (Figure 2.11). Combining with fine grids in the boundary grid, extremely accurate boundary location, area, density, surface tension, concentration and other material properties can be calculated to improve performance of the standard VOF methods in an Eulerian frame.

On the other hand, the Front-Tracking is a very complex method. In order to manipulate those markers evenly distributed on the interface and to maintain the mass conservation, a series of artificial adjustments is necessary [76]. Bubble breakup and coalescence need special handling too. The reaction and phase change in the bubble need great care to be treated.

In summary, VOF methods are the oldest and most widely used methods to directly advect the interface due to its relative simplicity and natural mass conservation. For the level-set methods, it is easy to extract the geometric information and easy to implement in 3D, however, it has the disadvantages of mass loss. The front-tracking methods are extremely accurate, yet due to its complexity limited in its application.

2.2.2 Bubble dynamics and mass transfer in simulation

The above mentioned three methods had good performance in the applications of bubble dynamics and mass transfer. No attempt was made to summarize all these simulations, but some typical results are reviewed here. Similar to the experimental studies, the results show in the aspects of bubble shape, bubble path, bubble wake and bubble mass transfer.

Bubble shape

The computed bubble shape is an important evaluation of the model's correctness. Therefore, there are many studies on the bubble shape simulation.

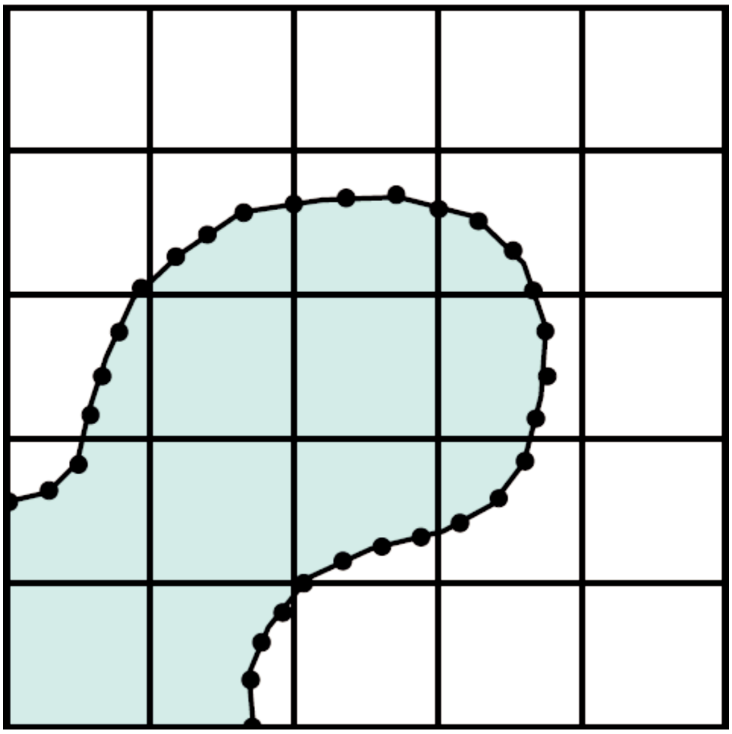

Figure 2.11: In front-tracking the fluid interface is represented by connected marker particles that are advected by the fluid velocity, interpolated from fixed grid [75].

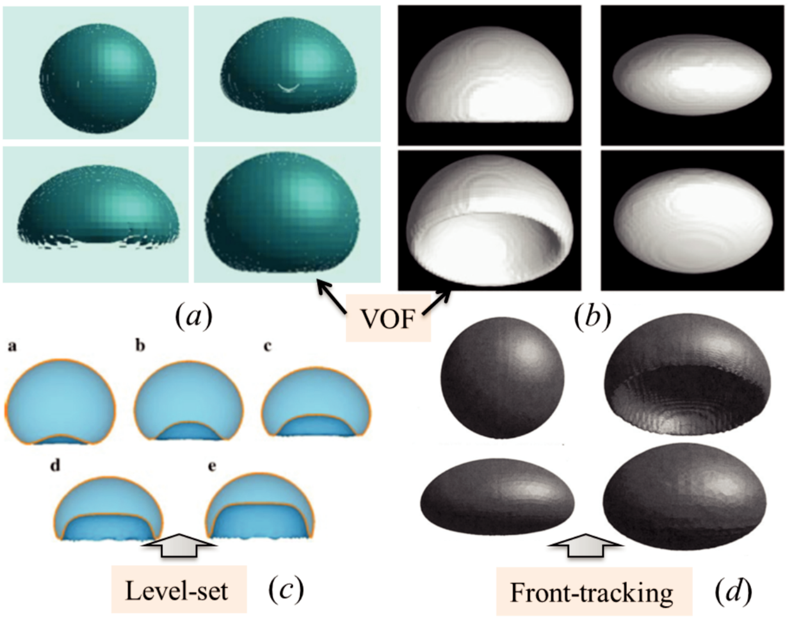

Figure 2.12: The simulated bubble shape by the three methods. (a) 3D spherical, ellipsoidal, skirted and dimpled bubbles in a viscous liquid by VOF methods (*Eo*: 1–100; *Mo*: 10^{-3}–10^{-1}; $Re < 20$) [77]. (b) 3D spherical-cap bubbles and ellipsoidal bubbles in viscous flow [78] by VOF methods. (c) 3D ellipsoidal cap bubbles at different conditions ($Eo = 116$; *Mo*: 1–1000; *Re*: 2–16.4) by level-set methods [70]. (d) 3D spherical, skirted, ellipsoidal and wobbling bubbles in various liquids by front-tracking methods (*Eo*: 0.97–10; *Mo*: 10^{-12}–97.1; *Re*: 1.6–1980) [64].

Figure 2.12 shows some simulated 3D bubble shapes by the three interface methods. All the models can reconstruct the bubble interface and predict the shapes of spherical, ellipsoidal and spherical-cap bubbles. However, in many studies, they focused on the bubbles in a viscous liquid at low Reynolds numbers. The simulation of the bubble shape in liquid water is therefore not common to find. In Figure 2.12, only (d) is the bubble shape in liquid water, all the other cases are the results for viscous fluid at very low *Re*. A complete and quantitative simulation of the three types of bubbles is still computationally very demanding.

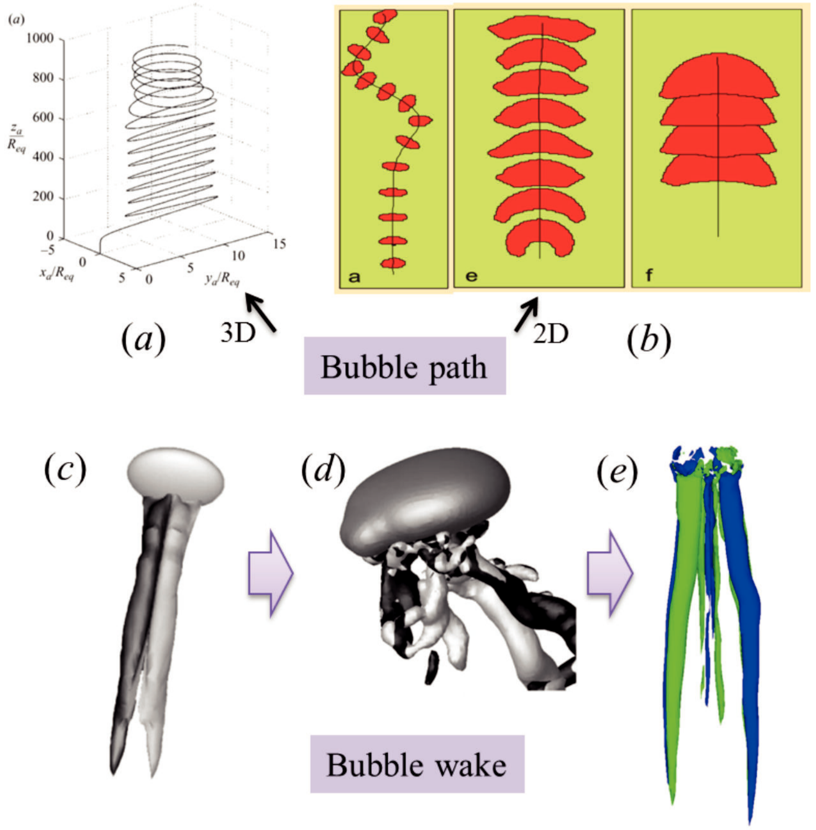

Figure 2.13: The simulated bubble path and wake. (a) The path of an oblate bubble [79]. (b) The rise trajectory for the bubble size of 4 mm, 12 mm, 20 mm [80]. (c) The isosurface of the streamwise vorticity for the shape [79]. (d) The vorticity isosurface for an asymmetric deformed bubble [81]. (e) The vortex structure when the bubble travels in a rectilinear path under magnetic field [82].

Bubble path and bubble wake

In addition to the studies of bubble shape, the bubble path and bubble wake are also studied numerically. Mougin & Magnaudet simulated the bubble path and wake structure for an ellipsoidal bubble with a prescribed shape [79] (Figure 2.13a and 2.13c). The classical VOF 2D simulation of the bubble path by Krishna & van Baten [80] is also shown in Figure 2.13b. Despite the big success in predicting the bubble path, they provide only a qualitative

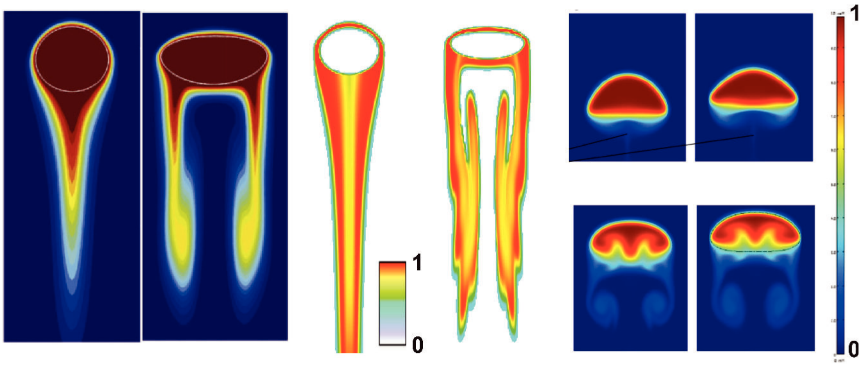

Figure 2.14: 8 Examples of simulated bubble mass transfer. (a) The mass transfer from a single rising bubble at different *Re* (8 and 60 respectively) [6]. (b) Distribution of local selectivity at different *Re* (16.2 and 34.8) [83]. (c) Solvent concentration at different times [84].

agreement. Gaudlitz & Adams coupled shape oscillation and path instability in the simulation [81] (Figure 2.13d). The wake structure studies are further extended to bubbles under a vertical magnetic field [82] (Figure 2.13e). These simulations reinforced the conjecture that path instability is mainly attributed to wake instability. The effects of bubble shape aspect ratio, lateral force on the wake instability were also discussed.

Mass transfer

The coupling of bubble dynamics and mass transfer is accomplished in all the three methods. Most of the studies on bubble mass transfer are in 2D, since the addition of the mass transfer equations greatly increases the computational cost, especially when the Schmidt number is large. In these simulations, they all focus on the mass transfer in the liquid phase, and the local concentration in the wake can be visualized. From the direct comparison of the images in Figure 2.14 and the measured contours in Figure 2.7, we know that a qualitative agreement can be achieved although Figure 2.7 is 3D and Figure 2.14 is 2D. For the liquid-phase mass transfer, the Schmidt number Sc has the order of 1000, *i.e.*, the mass boundary layer is much thinner than the momentum boundary layer. Therefore, in order to capture the mass concentration gradient, the Reynolds number is artificially decreased for a lower value of Schmidt number by increasing the viscosity. Figure 2.14a and 2.14b are the results under the conditions of $Re < 50$.

The validated mass transfer simulations for high-Reynolds-number oscillating bubbles in water are still missing.

2.3 Conclusions

Based on the experimental review, direct observation of mesoscopic gas bubbles in liquid metal in 3D is difficult, while it can be better captured in a 2D Hele-Shaw configuration. The averaged bubble flow characteristics such as bubble shape, bubble path can be visualized, however, a numerical simulation of 2D bubble dynamics is necessary for a full understanding of the bubble dynamics in two-dimensions. From the literature, it is known that even in water, 3D bubble dynamics is very complicated. Therefore, we also hope that by using a 2D configuration, the simpler phenomena studied can provide some fundamental knowledge and shed light to the questions in 3D. The water experiments provide more quantified data for experiments and easy-to-do experiments adopted as required by the validation requirements. Therefore, it was decided to model the bubble dynamics and evaporation-induced mass transfer in water due to the dynamic and mass transfer similarities of liquid water and liquid metal described under 2.1.1.

From the simulation point of view, direct numerical simulation models of gas-liquid flow and mass transfer are promising. All three methods mentioned under 2.2.1 have the potential to deal with these problems. The VOF method is most suitable in our case due to its natural mass conservation and accurate results [85]. With this model, we hope to get a quantified simulation of the two-dimensional bubble dynamics and mass transfer for high Reynolds number bubble flow in water.

Chapter 3

2D Bubble Dynamics

Buoyancy-driven single bubble behaviour in a vertical Hele-Shaw cell with various gap Reynolds numbers $Re(h/d)^2$ is studied in this chapter. Two gap thicknesses, $h = 0.5$ mm ($Re(h/d)^2 = 1.0$–8.5) and 1 mm ($Re(h/d)^2 = 6.0$–50) were used to represent low and high gap Reynolds number flow. Periodic shape oscillation and path vibration were observed once the gap Reynolds number exceeds the critical value of 8.5. The bubble behaviour was also numerically simulated by taking a two-dimensional volume of fluid (VOF) method coupled with a continuum surface force (CSF) model and a wall friction model in the commercial computational fluid dynamics (CFD) package Fluent. By adjusting the viscous resistance values, the bubble dynamics in the two gap thicknesses can be simulated. For the main flow properties including shape, path, terminal velocity, horizontal vibration and shape oscillation, good agreement is obtained between experiment and simulation. The estimated terminal velocity is 10%–50% higher than the observed one when the bubble diameter $d \leqslant 5$ mm, $h = 0.5$ mm and 9% higher when $d \leqslant 18$ mm, $h = 1.0$ mm. The estimated oscillation frequency is 50% higher than the observed value. Three-dimensional effects and spurious vortices are most likely the reason for this inaccuracy. The simulation confirms that the thin liquid films between gas bubbles and the cell walls have a limited effect on the bubble dynamics.

X. Wang, B. Klaasen, J. Degrève, B. Blanpain, F. Verhaeghe. Experimental and numerical study of bouyancy-driven single bubble dynamics in a vertical Hele-Shaw cell. *Physics of Fluids*, 26 (2014) 123303.

3.1 Introduction

A Hele-Shaw cell confines a bubble in a narrow gap between two flat parallel plates [54]. The thickness of the gap between the plates (h) is typically very small (normally in the order of 1 mm). When the confinement ratio $h/d \ll 1$ (d, the equivalent diameter of the bubble), the bubble inside the cell is flattened and loses the freedom in the third dimension, hence the bubble flow can be treated as two-dimensional [86]. Apart from the confinement ratio, the bubble motion in the Hele-Shaw cell is determined by the complex interplay of viscous forces, inertial forces and surface tension. Depending on the relative importance of these forces, the diversity of bubble dynamics can be represented. When the bubble Reynolds number is very small, *i.e.* $Re \ll 1$ ($Re = \rho u_b d/\mu$, ρ is the mass density of the fluid, u_b the velocity of the bubble, μ the dynamic viscosity of the fluid), the inertial forces are negligible, only viscous forces and surface tension are important. This regime is applicable for gas bubbles in a Hele-Shaw cell involving a highly viscous liquid, which has been studied analytically and experimentally [54–56, 86–88]. When the bubble Reynolds number is moderate or high, *i.e.* $Re \geqslant 1$, the inertial forces cannot be neglected, and all three forces are significant. The moderate Re regime (Re in the order of 100) refers to a gas bubble in a tilted Hele-Shaw cell filled with a low viscous liquid, while the high Re regime (Re in the order of 1000) corresponds to the bubble behaviour in a vertical Hele-Shaw cell with a low viscous liquid. The governing non-dimensional numbers for an unbounded two-dimensional buoyancy-driven bubble in the Hele-Shaw cell include the Archimedes number ($Ar = \rho\sqrt{\mathrm{g}d}d/\mu$), h/d and the Bond or Eötvös number ($Bo = Eo = \rho \mathrm{g} d^2/\sigma$), σ is the surface tension, g the gravitational acceleration. When the cell width W is finite and the bubble is large, h/W becomes influential and it can replace h/d when $r_c/W > 0.7$, where the dimension control changes from bubble dimension to cell width dimension and the bubble becomes a gas slug [89] (r_c, the radius of curvature at the front stagnation point). In addition, the gap Reynolds number $Re(h/d)^2$ is also an important parameter, which compares the in-plane inertial time scale and the in-gap viscous time scale [90, 91]. It is dependent on both Ar and h/d. Kelley and Wu [58] studied the path instability of a circular bubble at moderate Re and concluded that a critical Reynolds number ($\approx$ 200) controls the path instability. Bush [52] reported a peculiar wake structure of a penny-shaped air bubble at moderate Re. Using the same experimental technique, Bush and Eames [92] examined the fluid displacement associated with the rectilinear motion of oblate ellipsoidal/elliptical-cap bubbles. For these studies, only constant bubble shapes in a tilted Hele-Shaw cell were observed. Kawaguchi's group [59–61] and Roig *et al.* [9] expanded the studies to a large range of bubble sizes in a vertical cell at high Re. Kawaguchi *et al.* [59] examined the steady-state bubble shape, trajectory, and peripheral length in water as a function of *Eo* ($Eo \leqslant 40$, $Ar \leqslant 7 \times 10^3$, $h = 1.0$ mm, $W = 5$ cm) and pointed out that *Eo* is the controlling parameter of the path instability. This work was further extended to polymer solutions [60] and to transient states [61]. Roig *et al.* [9] investigated the path and shape oscillation of bubbles in water in a wider *Re* range ($Eo \leqslant 140$, $Ar \leqslant 15 \times 10^3$, $h = 1.0$ mm, $W = 40$ cm). Although the cell width values in their experiments are different, since an identical gap thickness was used, their results are consistent, *i.e.* the shape oscillation and path instability are coupled in most of the *Ar* range ($600 \leqslant Ar \leqslant 4 \times 10^3$ in ref [13] and $100 \leqslant Ar \leqslant 6 \times 10^3$ in ref [9]). In all these experiments, the governing parameter h/d was adjusted only by changing the initial bubble size while the cell gap thickness was fixed. As far as is known, the effect of gap thickness on the bubble dynamics in a vertical Hele-Shaw has not been studied in detail and the path and shape responses on gap thickness variations remain unknown.

In contrast to the availability of the experimental results on diverse high-Reynolds-number bubble shapes and paths, only the large spherical-cap bubbles were analytically studied [89]. The theoretical terminal velocity of the bubbles is given as $u_b = \varphi\sqrt{gd}$(with φ a constant in a given geometry) and Roig *et al.* [9] fitted their experimental data with $\varphi = 0.42$ ($Re > 3000$). In this equation, the velocity is assumed to be related to the bubble size only, and therefore the effect of the gap thickness h on the terminal velocity is not incorporated and unknown. To understand the bubble dynamics in a more fundamental way, a numerical simulation by taking all the related forces into account has to be conducted. Although the numerical method has been widely used to study the formation and dynamics of a single bubble in other media [93] and other types of flows in the Hele-Shaw cell [94–97], direct simulation of high-Reynolds-number bubble flow in the vertical Hele-Shaw cell filled with water has not been found in the open literature. In the present study, a 2D volume of fluid (VOF) method will be used to simulate the bubble dynamics in the vertical Hele-Shaw cell. The same method was used to simulate a free rising bubble [80, 98]. Different from these studies, Darcy's law is added in the model to describe the in-gap wall friction. By doing this, the Hele-Shaw cell high-Reynolds-number bubble dynamics can be simulated quantitatively and the effect of gap thickness can be incorporated easily and accurately.

3.2 Experimental setup

A vertical Hele-Shaw cell with two gap thicknesses has been constructed in the experiment: (1) $h = 0.5$ mm (± 0.02 mm), for low gap Reynolds number bubble behaviour; (2) $h = 1$ mm (± 0.02 mm), for high gap Reynolds number bubble behaviour. The other two dimensions of the cells were identical, *i.e.*

50 mm in width and 500 mm in height. The equipment is as described in ref [62]. The cell was made of soda-lime glass with a thickness of 10 mm. The glass plates were washed in advance with Piranha solution (3:1 mixture of 96% H_2SO_4 and 30% H_2O_2) to remove organic residues and hydroxylate surfaces, making the plates highly hydrophilic. A bubble was generated with a syringe needle (inner diameter range 0.3–0.8 mm) controlled by an electromagnetic micro valve (brand is Burker). By varying the time step of the valve and the needle inner diameter, the initial bubble size could be controlled. Technically pure nitrogen gas (99.9%) and ultrapure water (18.2 MΩcm resistivity at 25°C produced by Millipore Direct-Q 3 UV ultrapure water system) were used to avoid the effect of surface active agents. Thin liquid films were formed between the gas bubble and the wall due to the total wetting of water on the washed glass cell. The images of the bubble were recorded with a Tesin Cyclocam high speed video camera at a frame rate of 250 fps (resolution 640 × 480 pixels). The shutter time in the experiment was 2 ms. The recorded image frames were sequentially analysed with a Matlab-based processing script. In each frame, the area S, perimeter L, and gravity centre (x, y) of the bubble were determined by mapping the bubble contour. The equivalent diameter d of the two-dimensional bubble was calculated as $d = 2(S/\pi)^{1/2}$; the vertical velocity u_y as $u_y = \Delta y/\Delta t$ and the horizontal velocity u_x as $u_x = \Delta x/\Delta t$, where Δt is the time step.

3.3 Numerical simulation

Figure 3.1 schematically illustrates the buoyancy-driven single bubble flow in the vertical Hele-Shaw cell. As mentioned previously, the bubble motion in the Hele-Shaw cell (when $h/d \ll 1$) can be treated as two-dimensional. Roig *et al.* [9] confirmed that the motion is less sensitive to three-dimensional effects when $h/d \leqslant 0.5$. However, the viscous drag in the third dimension needs to be considered and coupled properly in the simulation. In this paper, a gap-averaged 2D simulation is used, in which assumptions are made according to the flow properties in the third dimension: (1) the effects of the thin films due to total wetting are neglected (Figure 3.1c); (2) the third-dimensional velocity distribution can be averaged (Figure 3.1e).

As for assumption (1), there are two equations that can be used to calculate the liquid film thickness ($2\delta_{film} = 1.337h(Ca)^{2/3}$ in ref [87] and $2\delta_{film} = 0.66h(Ca)^{2/3}/(1{+}3.33(Ca)^{2/3})$ in ref [99], $Ca = \mu u_b/\sigma$). These yield a similar result, *i.e.* $2\delta_{film} = 0.06h$–$0.08h$, which is quite small. Meanwhile, Roig *et al.* [9] studied the drag force due to the liquid films by using a scaling law and pointed out that the drag force depends on the boundary conditions at the bubble and thin film interface: if the interface is free of contaminants, a zero-shear-stress boundary condition applies and no extra force is exerted by the thin film; the contaminated interface becomes rigid and a no-slip boundary condition applies; while a partially contaminated interface may have a non-zero viscous shear stress. In their experiment, distilled water was used and it was found that the drag due to the thin films is negligible. In our experiment, ultrapure water was used and the glass plates were washed with Piranha solution, so the effects of contamination can be neglected and the drag force due to total wetting is assumed to be zero.

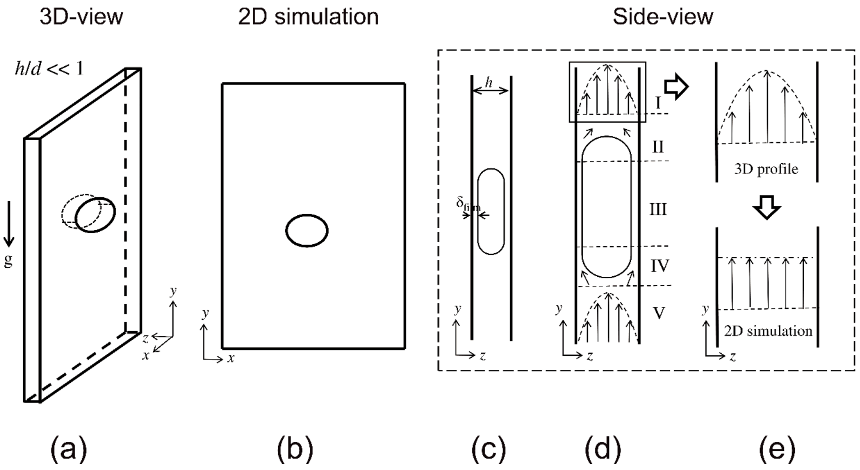

Figure 3.1: Illustration of the Hele-Shaw cell. (a) Schematic view of the three-dimensional cell. (b) Schematic view of the two-dimensional simulation. (c) Side view of a bubble rising within the gap. (d) The velocity vectors within the gap. (e) Simplification of velocity profile in 2D simulation.

As for the assumption (2), Beavers *et al.* [100] concluded that transition to turbulent flow only occurs when the cell Reynolds number $Re = \rho u h/\mu$ (the characteristic length is gap thickness h) exceeds 2200, so the laminar flow can be preserved safely in all cases once the velocity remains below 0.2 m/s and the cell thickness is below 9 mm simultaneously. When the flow is far away from the bubble interface, the velocity distribution is parabolic due to Poiseuille flow (regions I and V in Figure 3.1d). The velocity distribution in the third dimension can be averaged in our 2D simulation by adding an averaged additional force in the momentum equation, which is illustrated in Figure 3.1e. Inside the bubble (region III in Figure 3.1d), the velocity distribution depends on the thin films since the thin films can change the boundary conditions at the bubble-liquid film interface. However, their effects are negligible in our case and Poiseuille flow is assumed. Near the curved bubble interface (Regions II and IV in Figure 3.1d), the flow streamline is bent and confined by the surface tension in the third dimension, the viscous dissipation is therefore increased. [101] The three-dimensional effects are difficult to quantify and only qualitative estimations can be made here: large gap thickness and small bubble size lead to high three-dimensional effects. In the simulated gap thickness range (h = 0.5–1 mm) and bubble size range (d = 3–25 mm), we assume these effects are negligible and the flow in the gap follows the Poiseuille flow.

Other assumptions include: the fluids are incompressible, the entire system is isothermal so that constant fluid properties for both phases are guaranteed, and surface tension σ is constant.

3.3.1 Governing equations

Based on the above assumptions, the bubble dynamics in a vertical Hele-Shaw cell can be numerically simulated by a gap-averaged two-dimensional multiphase model. In the VOF method, a single set of momentum and continuity equations for unsteady, incompressible, immiscible two-phase flow is applied to both phases. The tracking of the interfaces between the phases is accomplished by the solution of the continuity equation for the volume fraction of each fluid through the domain:

Continuity:

$$\frac{\partial \rho}{\partial t} + \nabla \cdot (\rho \mathbf{u}) = 0 \tag{3.1}$$

Volume fraction:

$$\frac{\partial \rho \gamma}{\partial t} + \nabla \cdot (\rho \gamma \mathbf{u}) = 0 \tag{3.2}$$

Momentum:

$$\frac{\partial}{\partial t}(\rho \mathbf{u}) + \nabla(\rho \mathbf{u}\mathbf{u}) = -\nabla p + \nabla \cdot \mu(\nabla \mathbf{u} + \nabla \mathbf{u}^T) + \rho \mathbf{g} + \mathbf{F}_\sigma + \mathbf{F}_w \tag{3.3}$$

where $\mathbf{u}$ is the fluid velocity, t the physical time, p the pressure, γ the volume fraction of the second phase (gas phase) in the computational grid cell. When the grid cell is completely filled with liquid, γ equals zero; and γ equals one when the cell is completely filled with gas. For a grid cell containing the interface, γ takes a value between 0 and 1. $\mathbf{g}$ is the acceleration due to gravity, ρ the average density, and μ the average dynamic viscosity. In our case, ρ and μ are constant in each fluid with a jump at the interface. They can be defined by

$$\rho = \gamma \rho_g + (1 - \gamma)\rho_l \tag{3.4}$$

$$\mu = \gamma\mu_g + (1-\gamma)\mu_l \tag{3.5}$$

$\mathbf{F}_\sigma$ denotes an additional surface tension source term. The surface tension along the interface between gas bubble and water is described by the continuum surface force (CSF) model [66]. The force at the surface can be expressed as a volume force using the divergence theorem, which is added to the momentum equation as a source term:

$$\mathbf{F}_\sigma = -\sigma\rho\kappa\nabla\gamma/(0.5(\rho_g + \rho_l)) \tag{3.6}$$

where σ is the surface tension, κ the curvature of the interface, which is defined in terms of the divergence of the unit normal:

$$\kappa = \nabla \cdot (\nabla\gamma / \mid \nabla\gamma \mid) \tag{3.7}$$

where $\nabla\gamma$ is the gradient of the volume fraction γ, $|\nabla\gamma|$ the length of $\nabla\gamma$. The detailed calculation of the gradient of the volume fraction function and curvature can be found in ref [102, 103].

$\mathbf{F}_w$ is an additional in-gap wall friction source term, which can be described by Poiseuille's law:

$$\mathbf{F}_w = -12\mu\mathbf{u}/h^2 \tag{3.8}$$

where h is the gap thickness of the Hele-Shaw cell. It means the additional gap-averaged pressure drop in the Hele-Shaw cell has a linear relationship with the gap-averaged velocity. In simulation, Darcy's law is used to calculate the in-gap wall friction due to the similarity between the Hele-Shaw cell wall resistance and porous media resistance. The equation of Darcy's law for porous media resistance is as follows:

$$\mathbf{F} = -\mu\mathbf{u}/\alpha \tag{3.9}$$

where α is the viscous resistance. By comparing equation 3.8 with 3.9, the Hele-Shaw flow can be seen as a two-dimensional flow in porous media, whereby the viscous resistance α in the Hele-Shaw cell is equivalent to:

$$\alpha = h^2/12 \tag{3.10}$$

By using equation 3.10, the bubble behaviour in cells with different gap thicknesses can be simulated by adjusting the viscous resistance values. The wall friction source term is only applied to the liquid phase since the flow in the gas phase is not parabolic due to the existence of thin liquid films.

3.3.2 Simulation strategies

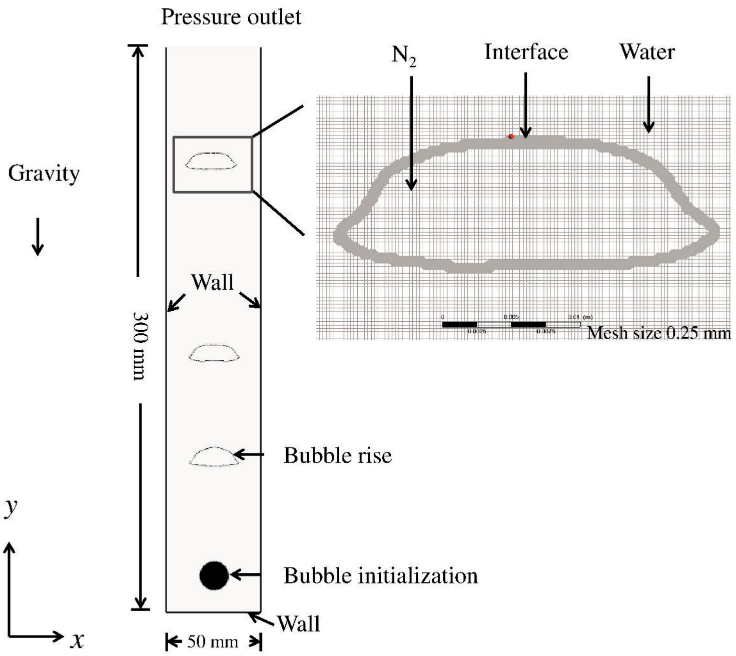

Figure 3.2: Computational domain and boundary conditions in simulation.

The commercial CFD software ANSYS Fluent 14.0 was used to simulate the motion of a single nitrogen gas bubble rising in a vertical Hele-Shaw cell filled with water. The computational domain consisted of a 50 mm in width by 300 mm in height rectangle, whose height was 200 mm less than the experimental conditions. No difference was found by decreasing the height due to small hydrostatic pressure difference (less than 2%). The domain was filled with stationary water and a spherical bubble was initialized in the centre bottom of the domain as shown in Figure 3.2. For the bubbles with large deformation (d = 8–11 mm for h = 1.0 mm), left-right asymmetric initial bubble shapes such as semicircle were initialized to avoid bubble break-up. The operating pressure was 1 atm. No-slip boundary conditions were applied at all walls. The initial bubble rise velocity was zero. The bubble was able to develop into a typical shape, to reach a terminal velocity within about 0.5 s and to rise to the liquid surface in 2.0–4.0 s depending on the terminal velocity. The steady-state data (1.0–2.0 s) was used for comparison. The volume fraction cut-off was 10^{-6}.

The simulated bubble size corresponds to the area enclosed by the contour line where the volume fraction $\gamma = 0.5$. The material properties were included in the Fluent database: the density of the water is 997 kg/m^3, the viscosity of the water is 8.94×10^{-4} Pa·s; the density of the nitrogen is 1.185 kg/m^3, the viscosity of the nitrogen is 1.663×10^{-5} kg/(m·s). The surface tension is 0.0729 N/m. Uniform quadrilateral meshing was used, each grid cell was 0.25 mm by 0.25 mm, which means 240,000 grid cells in total. Grid independence was proved by further reducing the grid cell size to 0.125 mm yielding only a 0.5% terminal velocity difference. A laminar model was chosen due to small cell Reynolds number values.

During the calculation, the unsteady scalar (pressure, velocity components and volume fraction) transport equations were discretized to algebraic equations by a control-volume method. An explicit geometric reconstruction scheme that is based on the PLIC (Piecewise-Linear-Interface-Calculation) method [104] was used to solve the volume fraction equation. Second-order upwind scheme was used to discretize the convection terms of the velocity components. The diffusion terms were discretized using a second-order accurate central differencing scheme. The gradients of the scalars needed in the convection and diffusion discretization were calculated using the least squares cell-based method. The velocity-pressure coupling and overall solution procedure were based on the SIMPLE (Semi-Implicit- Method for Pressure Linked Equations) segregated algorithm. A first order implicit time-marching scheme was used for the integration of the transient term. A constant time step (0.0005 s) was used.

3.4 Results and discussion

The bubble behaviour in the Hele-Shaw cell with the gap thicknesses of (1) h = 0.5 mm, viscous resistance $\alpha = 4.8 \times 10^7$ m^{-2}; (2) h = 1.0 mm, viscous resistance $\alpha = 1.2 \times 10^7$ m^{-2} were simulated and compared with experimental results. Section 3.4.1 and 3.4.2 show the results of h = 0.5 mm and h = 1 mm respectively.

3.4.1 Results for gap thickness $h = 0.5$ mm

In this section, the experimentally observed and simulated results of bubble shape, bubble path and bubble terminal velocity are compared and evaluated. The vortex and flow distribution are illustrated to understand the bubble dynamics fully.

Bubble shape and path

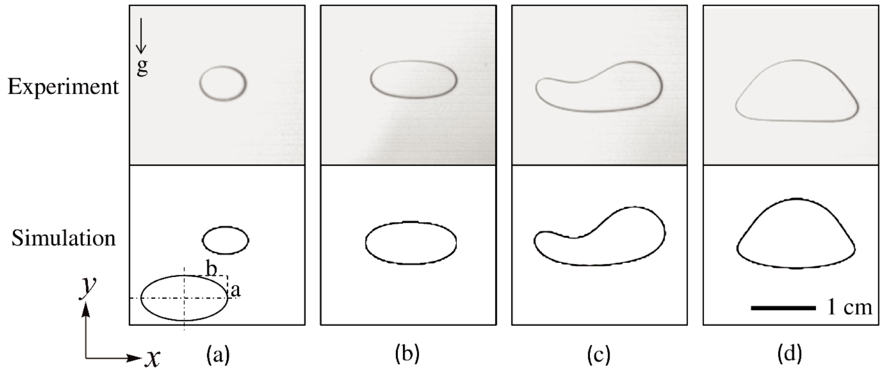

Figure 3.3: Comparison of bubble shapes between experiment and simulation for gap thickness $h = 0.5$ mm. Top: experiment. Bottom: simulation. (a) $d =$ 5 mm; (b) $d = 8$ mm; (c) $d = 11.5$ mm; (d) $d = 13$ mm. The downward arrow and symbol g show the direction of gravitational force.

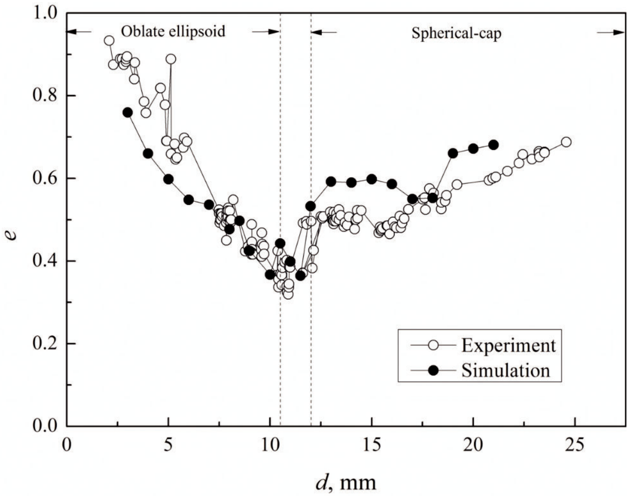

Figure 3.4: Comparison of bubble aspect ratio between experiment and simulation for gap thickness $h = 0.5$ mm.

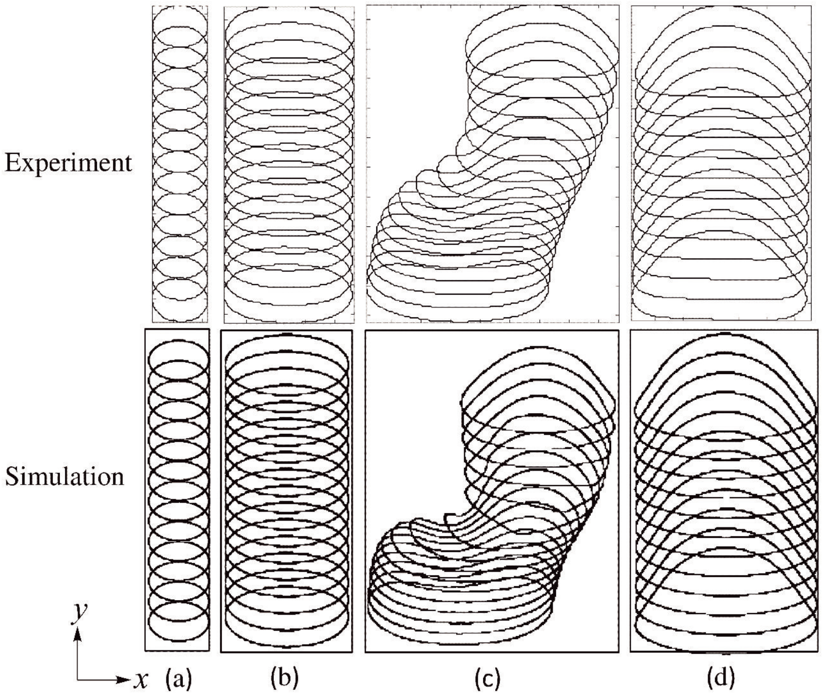

Figure 3.5: Comparison of bubble paths between experiment and simulation for gap thickness $h = 0.5$ mm. The successive contours are plotted at a time interval of 0.02 s. Top: experiment. Bottom: simulation. (a) $d = 5$ mm; (b) $d = 8$ mm; (c) $d = 11.5$ mm; (d) $d = 13$ mm.

Two shape regimes are found in the case of gap thickness $h = 0.5$ mm: oblate ellipsoid ($d < 10.5$ mm) and spherical-cap ($d > 12$ mm). The transition from oblate ellipsoid to spherical-cap occurs when $10.5 \text{ mm} < d < 12$ mm. The upper part of Figure 3.3 shows some typical experimentally observed bubble shapes. When d is small (Figure 3.3a and 3.3b), the bubble takes the shape of oblate ellipsoid. With an increase of d (Figure 3.3c), the bubble becomes unstable and loses the fore-and-aft symmetry. The fore-part of the bubble tends to have a negative curvature, which results in a transition to a spherical-cap regime (Figure 3.3d). A further increase in d does not change the bubble shape anymore. The simulated bubble shapes in the lower part of Figure 3.3 agree with the observed ones. To further characterize the shape change, the aspect ratio (e) evolution is illustrated in Figure 3.4, which is the ratio of the length projected on the symmetry axis to the maximum diameter normal to the axis [25] (a/b

in Figure 3.3). In the oblate ellipsoidal regime, e decreases with the increase of d, reaching lowest value of 0.31. In the spherical-cap regime, e increases with increasing d. The simulation results show a similar tendency with small deviations.

The paths of the bubbles are shown in Figure 3.5. Experiment and simulation show very similar results for different types of bubbles. A rectilinear path is observed for the oblate ellipsoidal and spherical-cap bubbles. The path deviates only when the shape undergoes the transition from oblate ellipsoid to spherical-cap (Figure3.5c). The path deviation lasts for less than 0.1 s. Once the transition is finished, the path becomes rectilinear again.

Bubble terminal velocity

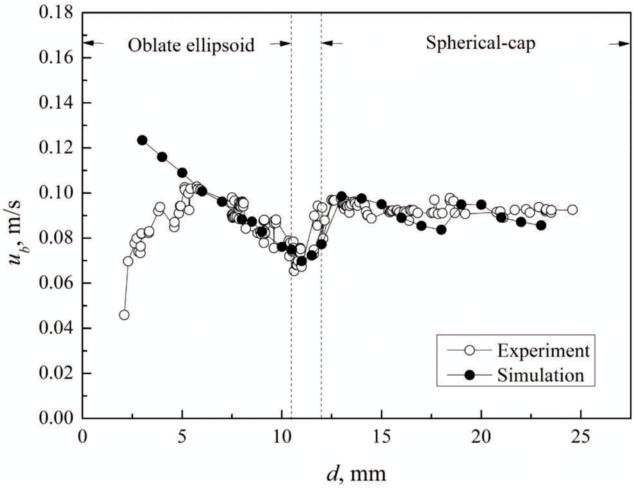

Figure 3.6: Comparison of terminal velocity between experiment and simulation for gap thickness $h = 0.5$ mm.

Figure 3.6 compares the simulated and observed terminal velocity for steady-state shapes. The observed velocity first increases and then decreases in the oblate ellipsoidal regime. In this regime, when the bubble size is small ($d < 5$mm), the increased buoyancy force leads to a velocity increase. With a further increase in bubble size, the drag force is increased due to the increase of the aspect ratio and therefore results in a decrease in terminal velocity. For transition bubbles, the terminal velocity increases with the bubble size as the aspect ratio increases. The change of terminal velocity becomes limited when the bubble reaches a spherical-cap shape ($d > 12$ mm). The overall experimental terminal velocity range is 0.046–0.10 m/s ($d = 2$–25 mm). Compared to the experimental data, the simulation results follow a similar trend as a function of bubble size when $d > 5$ mm. However, the simulation overestimates the terminal velocity when $d \leqslant 5$ mm. The smaller the bubble size, the higher the deviation (10%–50%) between experiment and simulation.

Vortex and flow distribution

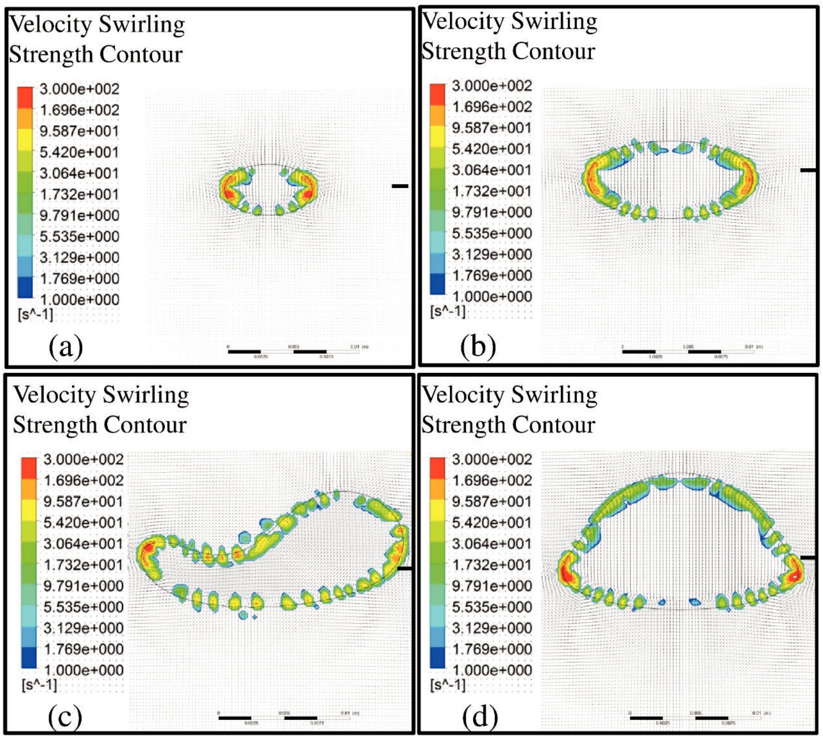

Figure 3.7: The simulated velocity swirling strength contours for gap thickness $h = 0.5$ mm. (a) $d = 5$ mm; (b) $d = 8$ mm; (c) $d = 11.5$ mm; (d) $d = 13$ mm.

The simulated vortices are given in Figure 3.7 to further understand the bubble path. There is no universally accepted mathematical definition of a “vortex”.

Both vorticity (curl of the velocity) and swirling strength can be used to visualize the vortices [105]. The swirling strength can better visualize the vertex core, so we use swirling strength instead of vorticity. It is used to identify and visualize the vortex contour, which uses the imaginary part of the complex eigenvalue of $\nabla \mathbf{u}$ to visualize vortices and to quantify the strength of the local swirling motion inside the vortex [105, 106]. It can be seen that the vortices are found only near the gas bubble/water interface. This is due to the spurious vortical currents induced by the coupled CSF force model [102]. It is a common problem in simulation and does not affect the calculation of bubble shape and terminal velocity [107, 108]. Vortices are not found in the liquid, which means that the vorticity is not strong enough to form a vortex core, and the wake is thus closed without vortex shedding. Without the effect of vortices, the path orientation is not perturbed and remains rectilinear.

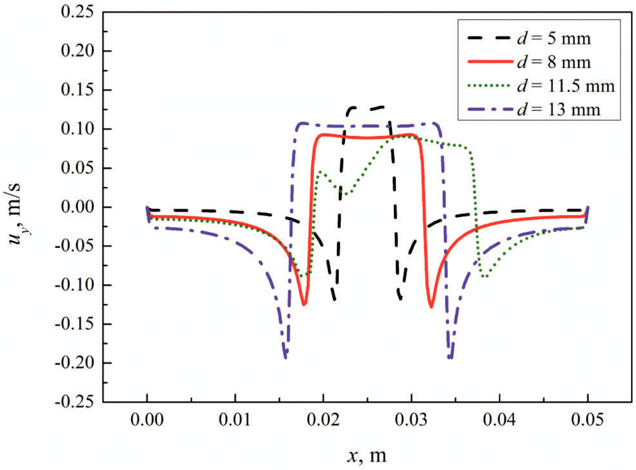

Figure 3.8: The vertical velocity distribution as a function of horizontal distance x for gap thickness $h = 0.5$ mm. The height at which the x coordinate axis is positioned is marked with a short marker line on the right side of the plots in Figure 3.7.

The vertical velocity across the bubble interface along the whole cell width is illustrated in Figure 3.8. In all cases, the liquid backflow can be seen clearly. Except for $d = 5$ mm ($d/W \leqslant 0.1$), the no-slip boundary conditions will directly affect the flow profile in the plane of the cell.

To summarize, the following flow behaviour can be obtained from experiments for gap thickness $h = 0.5$ mm: (1) two shape regimes when $d \geqslant 2$ mm, oblate

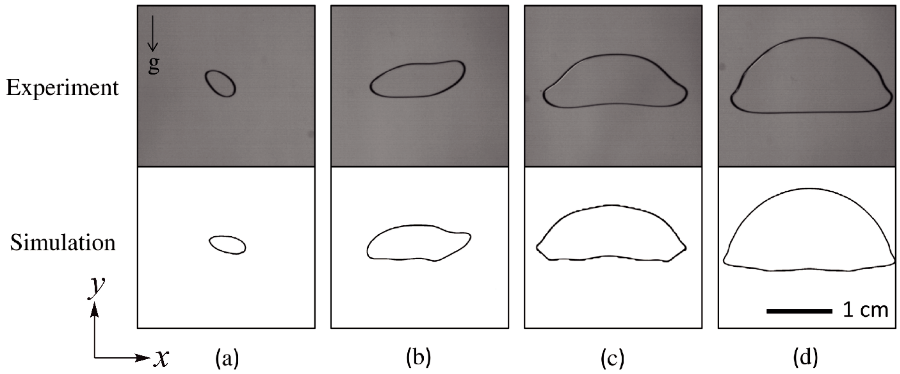

Figure 3.9: Comparison of bubble shapes between experiment and simulation for gap thickness $h = 1.0$ mm. Top: experiment. Bottom: simulation. (a) $d =$ 5 mm; (b) $d = 10$ mm; (c) $d = 15$ mm; (d) $d = 20$ mm. The downward arrow and symbol g stands for the direction of gravitational force.

ellipsoid and spherical-cap; (2) oblate ellipsoidal and spherical-cap bubbles take the rectilinear path; shape transition results in path deviation, the deviation lasts for 0.1 s; (3) the terminal velocity is in the range of 0.046–0.10 $\mathrm{m{\cdot}s^{-1}}$. The simulation results agree with the experimental results very well except for the overestimation of the terminal velocity when $d \leqslant 5$ mm. The simulation shows no vortices in the liquid region, which explains the rectilinear path. It also shows that the side-wall effects are not negligible when $d/W > 0.1$.

3.4.2 Results for gap thickness $h = 1.0$ mm

Similar to section 3.4.1, the experimental and simulated results on bubble shape, bubble path, bubble terminal velocity and bubble secondary motion are compared in this section for a gap thickness of $h = 1.0$ mm, followed by the simulated results on vortex and flow distribution.

Bubble shape and path

The bubble shapes for gap thickness $h = 1.0$ mm are more complicated compared with those for $h = 0.5$ mm. Except for the shapes of oblate ellipsoid and spherical-cap, bubble rotation, deformation and oscillation (periodic deformation) result in two more shape regimes: a wobbling regime and an oscillating spherical-

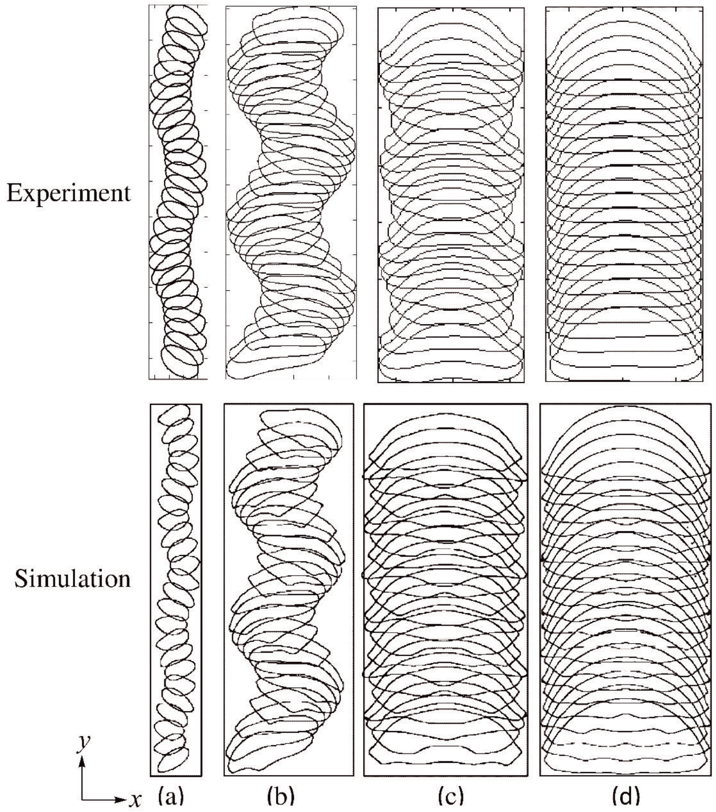

Figure 3.10: Comparison of bubble paths between experiment and simulation for gap thickness $h = 1.0$ mm. The successive contours are plotted at a time interval of 0.02 s. Top: experiment. Bottom: simulation. (a) $d = 5$ mm; (b) $d = 10$ mm; (c) $d = 15$ mm; (d) $d = 20$ mm.

cap regime. The typical contours of the four shape regimes are illustrated in Figure 3.9. Figure 3.9a illustrates an oblate ellipsoid bubble. Its fore-aft and left-right symmetry is lost due to shape rotation. Figure 3.9b is a wobbling bubble. The interface of the bubble is deformed by shape oscillation. The oscillating spherical-cap bubble contour is shown in Figure 3.9c, which has left-right symmetry as the spherical-cap bubble (Figure 3.9d). The simulated bubble shapes (bottom part of Figure 3.9) are very close to the observed bubble shapes and agree with the results in [59] and in [9].

The comparison of the typical bubble paths is shown in Figure 3.10. Different bubble regimes have different bubble paths. The oblate ellipsoidal bubble (Figure 3.10a) has a zigzag path with a very small shape oscillation. The wobbling bubble (Figure 3.10b) has a zigzag path with a strong shape oscillation. For oscillating spherical-cap bubble (Figure 3.10c), the path becomes rectilinear accompanied by a continuous shape oscillation. The shape oscillation disappears for a spherical-cap bubble (Figure 3.10d), resulting in a straight path only. The simulation can predict the path transition and shape change correctly. Differently, the simulated spherical-cap bubble (d = 20 mm) has a small fluctuation in the rear surface, which disappears when $d \geqslant 22$ mm.

Bubble terminal velocity

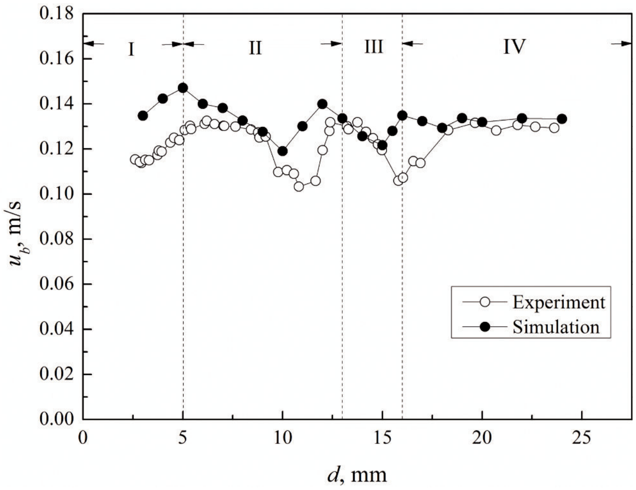

Figure 3.11: Comparison of terminal velocity for gap thickness h = 1.0 mm. I: oblate ellipsoid; II: wobbling; III: oscillating spherical-cap; IV: spherical-cap.

The comparison of the terminal velocity in experiment and simulation is illustrated in Figure 3.11. Since there are four shape regimes now, the terminal velocity evolution as a function of bubble size is more complicated than that of h = 0.5 mm (two regimes). In the experiment, the terminal velocity increases with increasing bubble size when the bubble is oblate ellipsoidal due to the increased buoyancy force. The terminal velocity first decreases and then increases when the bubble is wobbling. It reaches the lowest value when d = 10.5 mm. The velocity decreases again when the bubble is in the oscillating spherical-cap regime due to energy dissipation during oscillation. The terminal velocity increases when the spherical-cap regime is reached due to the decrease of the shape oscillation, and it becomes almost constant in the end. The overall terminal velocity range is 0.10–0.14 m/s. The simulated bubble terminal velocity is close to the experimental results with an averaged 9% deviation (higher value in simulation) when $d \leqslant 18$ mm.

Horizontal vibration

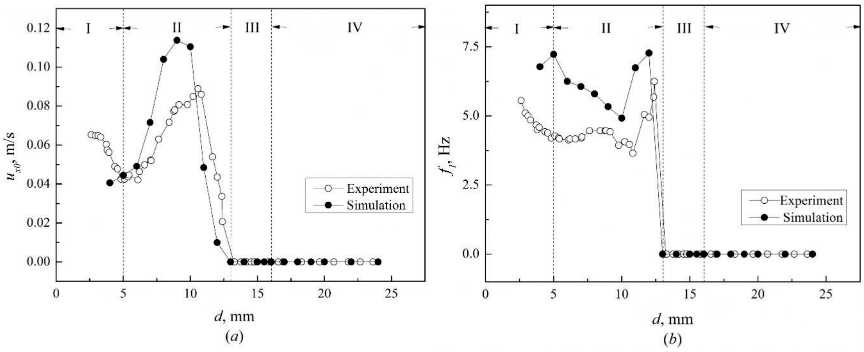

Figure 3.12: Comparison of horizontal velocity (a) amplitude u_{x0} and (b) frequency f_1 for gap thickness $h = 1.0$ mm. I: oblate ellipsoid; II: wobbling; III: oscillating spherical-cap; IV: spherical-cap.

The zigzag path is characterised by the periodic horizontal vibration. To describe the horizontal vibration of the bubbles, a sine function similar to the one proposed by Kozuka *et al.* [60] can be used:

$$u_x(t) = u_{x0} \sin(2\pi f_1 t + \alpha) \tag{3.11}$$

Where $u_x(t)$ is the horizontal velocity at a given time t, u_{x0} the horizontal velocity amplitude, $2\pi f_1$ the angular frequency and α the initial phase difference. Therefore, two important parameters, namely amplitude u_{x0} and horizontal velocity frequency f_1, can be used to characterize the horizontal vibration. Their experimental and theoretical comparisons are shown in Figure 3.12. It can be seen from Figure 3.12a that only oblate ellipsoidal and wobbling bubbles have periodic horizontal velocity. The observed horizontal velocity amplitude decreases with increasing bubble size when the bubble is oblate ellipsoidal, then it increases when the bubble starts wobbling and finally decreases to zero when the bubble becomes spherical-cap. The highest value of 0.09 m/s is reached when $d = 10.5$ mm. The horizontal vibration evolution goes the contrary to the evolution of the terminal velocity. The simulated amplitude evolution follows a similar tendency as in the experiments but with a higher peak value. Figure 3.12b shows the frequency comparison. It is clear that the experimentally horizontal velocity frequency is in the range of 4–6 Hz. The simulated frequency has a similar change but with a higher frequency range of 5–8 Hz.

Shape oscillation

Similar to the horizontal vibration, the shape oscillation can also be described by amplitude and frequency. Perimeter oscillation is used in this study to describe the bubble shape oscillation. Only the frequency with the larger amplitude is compared. Figure 3.13a shows the perimeter oscillation amplitude f_2 as a function of bubble size. The oscillation shows up in three bubble types. The effect is very small when the bubble is oblate ellipsoidal. When the bubble is wobbling, the amplitude first increases and then decreases to a lowest value. The oscillation slows down gradually until it reaches zero when the oscillated bubble is spherical-cap. The simulated results follow the same evolution as a function of bubble size. However, when $16 \leqslant d \leqslant 17$ mm, the simulated bubbles still have shape oscillation with a constant frequency while the experimentally observed bubble does not.

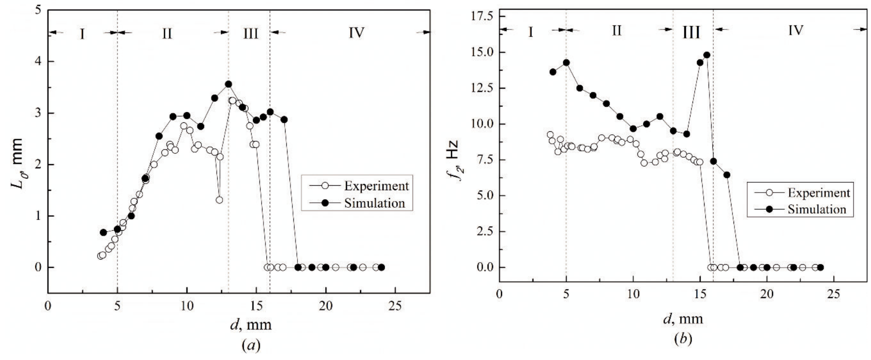

Figure 3.13: Comparison of perimeter oscillation (a) amplitude L_0 and (b) frequency f_2 for gap thickness $h = 1.0$ mm. I: oblate ellipsoid; II: wobbling; III: oscillating spherical-cap; IV: spherical-cap.

Figure 3.13b shows the frequency comparison of the perimeter oscillation. The frequency of the perimeter oscillation in the experiments is approximately twice the frequency of the horizontal vibration when d $\leqslant$ 10.5 mm, then the shape oscillation frequency becomes independent due to the reduced path vibration. The predicted frequency in the simulations is also higher than the observed one.

Irregularity is found in the simulation results when $d = 15$ and 15.5 mm, with a frequency that is twice that of the neighbouring bubbles. The reason for this is not clear, it is possible that the secondary oscillation is suddenly enlarged so that a higher magnitude as the primary oscillation is obtained.

Vortex and flow distribution

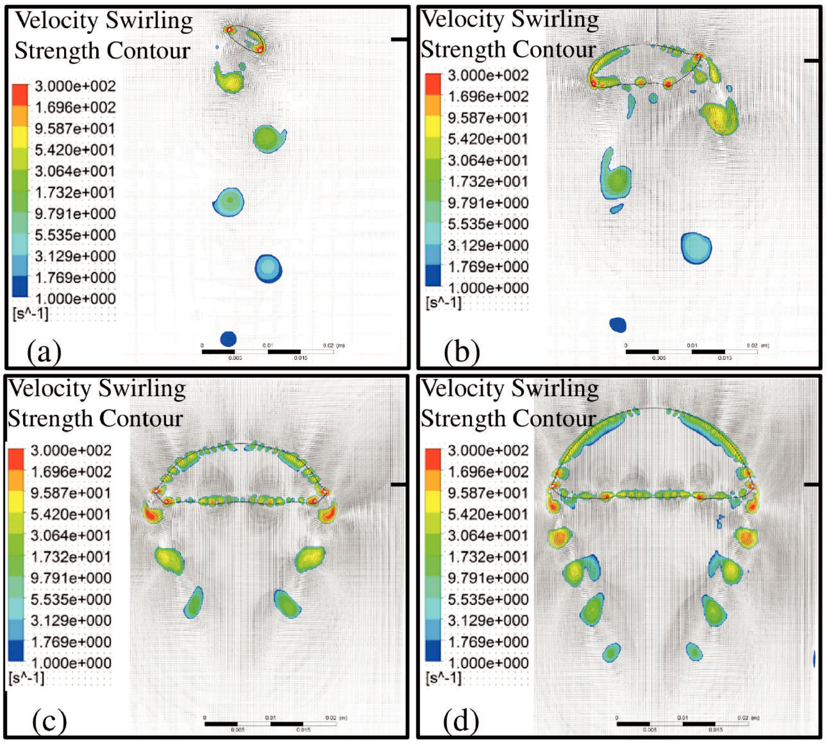

Figure 3.14: The simulated velocity swirling strength contours for gap thickness $h = 1.0$ mm. (a) $d = 5$ mm; (b) $d = 10$ mm; (c) $d = 15$ mm; (d) $d = 20$ mm.

The simulated flow vortex is illustrated in Figure 3.14 to give a better understanding of the gas-liquid flow interaction. The same vortex detection method is used as in the case of gap thickness $h = 0.5$ mm. Different from that case, vortex shedding is found now for all the bubble types and it is affected by the bubble regimes. For oblate and wobbling bubbles which go through a zigzag path, the vortices are asymmetric. For spherical-cap bubbles with a rectilinear path, vortices are shedding simultaneously from both sides of the bubble edge. The dissipation of the vortex is very fast. Only several vortices are found behind the bubble. The simulation results resemble the experimental observation in ref [60].

Similarly, the simulated vertical velocity distribution across the bubble interface along the whole width is shown in Figure 3.15. The liquid velocity near the side walls is very high, and increases with an increase of the bubble size. When d = 20 mm, the liquid backflow velocity is about 0.15 m/s near the wall. This means that the side-wall effects are influential to the bubble terminal velocity and shape oscillation.

As a whole, the bubble behaviour in a cell with gap thickness $h = 1.0$ mm has the following characteristics: (1) four bubble shapes, oblate ellipsoid, wobbling, oscillating spherical-cap and stable spherical-cap; (2) in addition to a rectilinear path, a zigzag path is coupled with the oscillating bubble shape; (3) the bubble terminal velocity is in the range of 0.10–0.14 m/s; (4) the horizontal vibration affects two bubble regimes, while the shape oscillation affects three bubble regimes. All these phenomena can be simulated reasonably well.

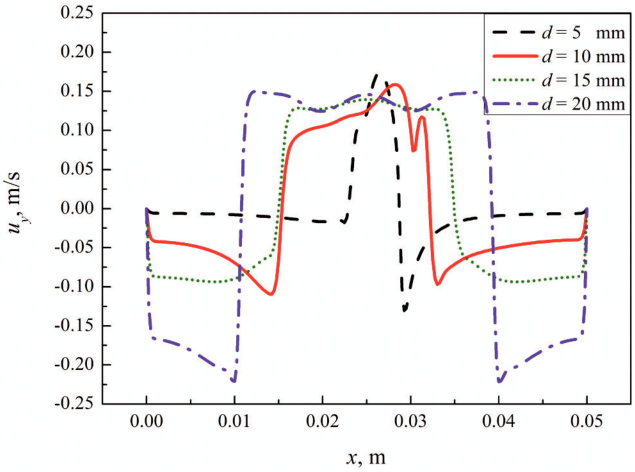

Figure 3.15: The vertical velocity distribution as a function of horizontal distance x for gap thickness $h = 1.0$ mm. The height at which the x coordinate axis is positioned is marked with a short marker line on the right side of the plots in Figure 3.14.

3.4.3 Discussion

Comparison of the bubble behaviour in the two gap thicknesses

Table 3.1: The vertical Hele-Shaw bubble motion in two different gap thicknesses in the experiment (vortex from simulation).

h, mm	d, mm	Shape	Path	Terminal velocity, m·s^{-1}	Vortex
0.5	2–10.5	Oblate ellipsoid	Rectilinear	0.046–0.10	No
0.5	12–25	Spherical-cap	Rectilinear	0.10	No
1.0	2–5	Oblate ellipsoid	Zigzag	0.11–0.14	Asymmetric shedding
1.0	5–13	Wobbling	Zigzag	0.11–0.14	Asymmetric shedding
1.0	13–16	Oscillating spherical-cap	Rectilinear	0.11–0.13	Symmetric shedding
1.0	16–25	Spherical-cap	Rectilinear	0.13	Symmetric shedding

As shown in the results, by changing the cell gap thickness, the bubble flow characteristics including shape, path, terminal velocity and vortex become quite different, as summarized in Table 3.1. Only two stable shapes are found in the case of gap thickness h = 0.5 mm, while four are present in the case of h = 1.0 mm. Furthermore, shape oscillation accompanies the wobbling and spherical-cap regimes of h = 1.0 mm. In the current experiments, the bubble size and cell width are kept the same with identical Ar and Bo, and therefore any difference in the bubble motion behaviour is directly caused by the change in the gap thickness. With a narrow gap thickness, a higher viscous resistance is expected and the dependence of bubble motion on bubble size can also be less significant. As given in Table 3.1, the bubble paths for h = 0.5 mm are rectilinear only, while both zigzag and rectilinear paths can be observed for h = 1.0 mm in the observed bubble size range. A difference in the corresponding terminal velocity is also observed. A higher velocity is obtained for h =1.0 mm for the same bubble size. In addition, different gap thicknesses result in very distinctive vortex behaviour: no vortices when h = 0.5 mm, while vortex shedding and the ensuing bubble oscillation when h = 1.0 mm.

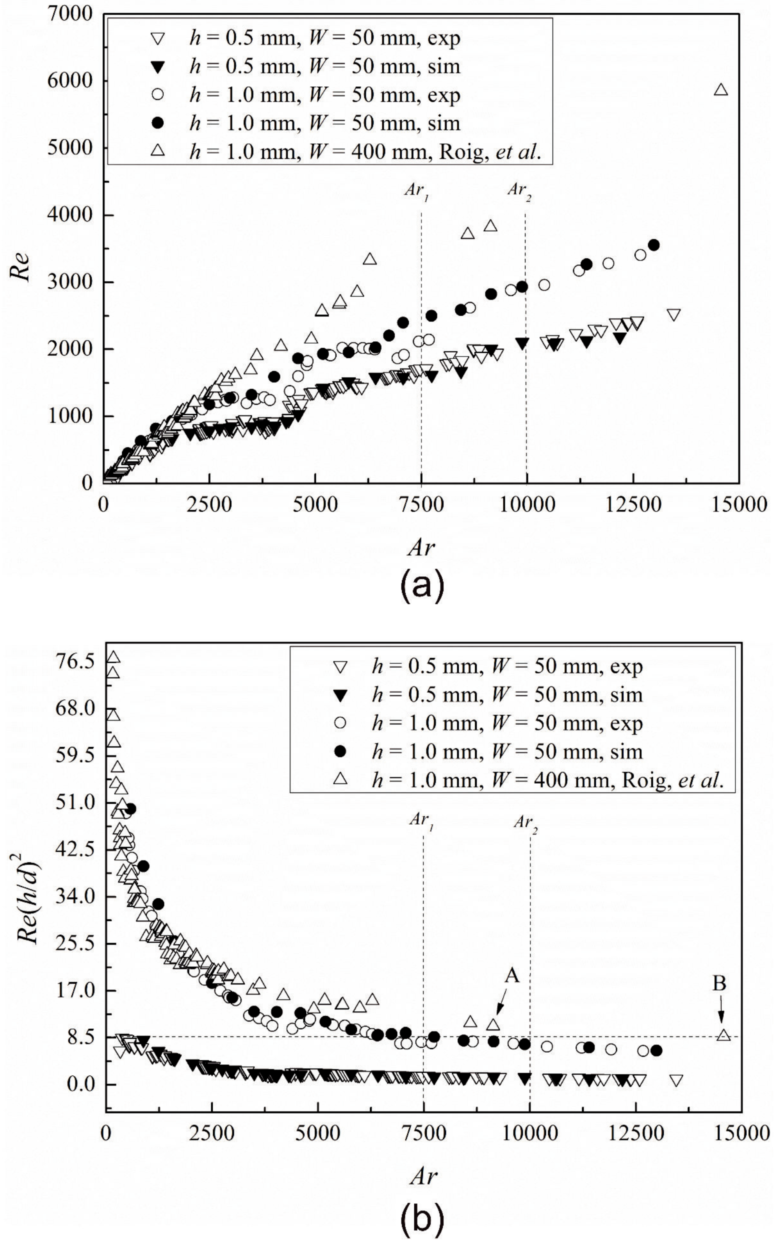

Figure 3.16: Re and $Re(h/d)^2$ evolution as a function of Ar. (a) Re; (b) $Re(h/d)^2$. The values for $Re(h/d)^2$ at point A and B are 10.6 and 8.1, respectively.

Governing parameters for the bubble shape and path instabilities

The non-dimensional governing parameters for the unbounded two-dimensional bubble dynamics in a vertical Hele-Shaw cell include Ar, Bo, h/d. In this research, although the cell width is finite, $r_c/W < 0.7$ is satisfied in the whole bubble size range, with a maximum value of 0.6. Therefore, the effect of h/d is significant and cannot be simply replaced by h/W. That is to say, the dimensionless numbers for our finite bubble dynamics include Ar, Bo, h/d and d/W. To quantify how these parameters control the bubble dynamics, especially to discover the onset of the shape and path instabilities, the Re and $Re(h/d)^2$ evolution as a function of Ar are compared in Figure 3.16. For generalization, the experimental results of the unconfined bubbles in ref [9] are also presented to compare with our results.

The effects of d/W can be seen by comparing the results of $h = 1.0$ mm, $W = 50$ mm with that of $h = 1.0$ mm, $W = 400$ mm by Roig, *et al* [9]. When $h = 1.0$ mm, $W = 50$ mm, there is a critical Ar number ($Ar_1 = 7500$) which controls the disappearance of the shape and path instabilities. For $W = 400$ mm, the critical Ar number increases to $Ar_2 \approx 10000$ [9]. Besides, higher Re and $Re(h/d)^2$ values are observed when $Ar \geqslant 2500$. Despite the difference in behaviour, it is clear that the shape and path instabilities are not controlled by d/W when $Ar < 7500$ since different d/W can have similar bubble instabilities. Instead, h/d is more likely to be the main controlling parameter due to the distinct behaviour in the two different gap thicknesses. When $h = 0.5$ mm, there is no critical Ar number since all the bubbles have a stable shape and path. Therefore, the Ar number is not the universal controlling parameter for the shape and path instabilities.

For both gap thicknesses, Re increases linearly with Ar, following the same trend in ref [9]. Re falls in the range of 200–2600 and 200–3500 in the case of gap thicknesses $h = 0.5$ and 1.0 mm respectively when the cell width $W = 50$ mm. Since high Re motion is obtained in all cases, the Re number by itself cannot explain the observed behavioural differences.

The $Re(h/d)^2$ evolution is shown in Figure 3.16b. For $h = 0.5$ mm, $W = 50$ mm, all bubbles have a stable shape and path and they lie in the region where Re(h/d)2 < 8.5. For h = 1.0 mm, W = 50 mm, the stable bubbles when $Ar_1 \geqslant 7500$ also lie in the same region of $Re(h/d)^2 \leqslant 8.5$. For a wide cell of $h = 1.0$ mm, $W = 400$ mm, the transition between oscillatory and steady motions is hard to define experimentally due to the difficulty of producing a single bubble [9]. However, based on the available two data points (A and B in Figure 3.16b, their trajectories were shown in Figure 3.13, ref [9]), it was found that the bubble is unstable when $Re(h/d)^2 = 10.6$ (point A) while it is stable when $Re(h/d)^2 = 8.1$ (point B), therefore, a similar $Re(h/d)^2$ value ($8.1 \leqslant Re(h/d)^2 < 10.6$) is assumed to control the shape and path instabilities as well. These analogous results demonstrate that $Re(h/d)^2$ determines (or partially determines) the stability of shape and path. Above a critical $Re(h/d)^2$ value, shape oscillation coupled with path vibration determines the main flow characteristics, while shape and path stabilities can be reached once $Re(h/d)^2$ is below this critical value. And the critical value of 8.5 can be applied in both gap thicknesses. Therefore, a general rule based on both the confined bubbles and also the unconfined bubbles can be stated here: small $Re(h/d)^2$ leads to shape and path stabilities.

Model evaluation

The effectiveness of the gap-averaged 2D simulation is evaluated based on the comparison between simulation and experiment in the two cases. For the case of $h = 0.5$ mm, except for the overestimation of the terminal velocity when $d \leqslant 5$ mm ($h/d \geqslant 0.1$), the simulated bubble shape, path and terminal velocity are quite accurate. This good agreement with experiment shows that the 2D simulation is enough to describe the bubble dynamics when the gap Reynolds number is small. It also confirms that the effects of the thin film effects on the bubble shape and terminal velocity are limited and can be neglected. For the case of $h = 1.0$ mm, the bubble shape and path are accurate, the terminal velocity can be predicted with an average overestimation of 9% when $d \leqslant 18$ mm ($h/d \geqslant 0.06$), the secondary motion (path vibration and shape oscillation) can be captured by simulation with a higher frequency. That is to say, the main discrepancy in simulation is the overestimation of the terminal velocity and the oscillation frequency. The overestimation of the terminal velocity in the two cases can be caused by several factors: (1) existence of three-dimensional effects; (2) roughness of the cell and (3) possible existence of turbulence. Each of these three factors induces a higher viscous dissipation, resulting in a low terminal velocity. However, (2) and (3) are not likely to be the main reason, because their effects are universal while the overestimation only happens in some size range. Instead, the three-dimensional effects can explain the distinction. When the gap thickness is small ($h = 0.5$ mm), the three-dimensional effects are minor, so only small bubbles are affected. With a doubling of the gap thickness ($h = 1.0$ mm), the bubble projected area in the gap is therefore also doubled, so more bubbles are influenced. Especially when the bubble is oscillating, the third-dimensional fluctuation may cause additional energy dissipation. However, the reason for obtaining a higher frequency in the simulation is still not clear, probably the three-dimensional effects contribute to it. In the experiment the constraints of the front and back walls may change the wake structure and slow down the oscillation, which makes the frequency different from the 2D simulation conditions. Apart from the three-dimensional effects, the spurious vortex in the CSF method itself may be a cause of the discrepancy as well. To fully understand the bubble behaviour in the third dimension and its effects, a full 3D simulation is necessary.

3.5 Conclusion

The bubble dynamics in a vertical Hele-Shaw cell with two different gap thicknesses have been examined experimentally. The main bubble properties including shape, path, terminal velocity change considerably when the cell gap thickness was narrowed from $h = 1.0$ mm to $h = 0.5$ mm. The shape and path stabilities were found to be determined by a critical value of $Re(h/d)^2$, that is equal to 8.5 under the present experimental conditions. The shape and path are stable when $Re(h/d)^2 \leqslant 8.5$, while vibrating when $Re(h/d)^2 > 8.5$.

Meanwhile a 2D VOF method coupled with a CSF model and a wall friction model has been applied to simulate the bubble dynamics in the two cases. By comparing with the experimental results, the simulation results are quantified as follows: (1) For $h = 0.5$ mm, the bubble shape, bubble path and bubble terminal velocity can be simulated very well when $d \geqslant 5$ mm. (2) For $h = 1.0$ mm, the bubble shape, bubble path can also be simulated accurately. The calculated terminal velocity is around 9% higher when $d \leqslant 18$ mm. The simulated velocity frequency and the perimeter oscillation frequency are 50% higher than the experimentally observed value. The agreement of the terminal velocity for most of the bubbles in $h = 0.5$ mm and large bubbles in $h = 1.0$ mm confirms that the thin liquid films have a limited effect on the bubble dynamics and can be neglected. The overestimation of terminal velocity and oscillation frequency are probably due to three-dimensional effects and spurious vortex.

Chapter 4

Effect of Gap Thickness

Bubbles in confined geometries serve an important role for industrial operations involving bubble-liquid interactions. However, high Reynolds number bubble dynamics in confined flows are still not well understood due to experimental challenges. In the present paper, combined experimental and numerical methods were used to provide a comprehensive insight into these dynamics. The bubble behaviour in a vertical Hele-Shaw cell was investigated experimentally with a fully wetting liquid for a variety of gap thicknesses. A numerical model was developed using the volume of fluid method coupled with a continuum surface force model and a wall friction model. The developed model successfully simulated the dynamics of a bubble under the present experimental conditions and showed good agreement between experimental and simulation results. It was found that with an increased spacing between the cell walls, the bubble shape changes from oblate ellipsoid and spherical-cap to more complicated shapes while the bubble path changes from only rectilinear to a combination of oscillating and rectilinear; the bubble drag coefficient decreases and this results in a higher bubble velocity caused by a lower pressure exerted on the bubble; the wake boundary and wake length evolves gradually accompanied by vortex formation and shedding.

The results described in this chapter are published in the following articles:

X. Wang, B. Klaasen, J. Degrève, B. Blanpain, F. Verhaeghe. Volume-of-fluid simulations of bubble dynamics in a vertical Hele-Shaw cell. (Submitted to *Physics of Fluids*)

4.1 Introduction

Bubbles play an important role in various industrial applications. In many cases, bubbles travel in a confined geometry instead of an unbounded medium. For instance, bubble dynamics in porous media, where bubbles are confined by the surrounding materials, have been widely used in fields such as air sparging, froth flotation, enhanced oil recovery, emulsion filtration and fluidized-bed reactor operations [109]. In order to understand bubble behavior in such conditions, this research defines a generalized model in which the bubble is confined between two flat parallel plates separated by a small gap - a vertical Hele-Shaw cell (Figure 4.1) [87].

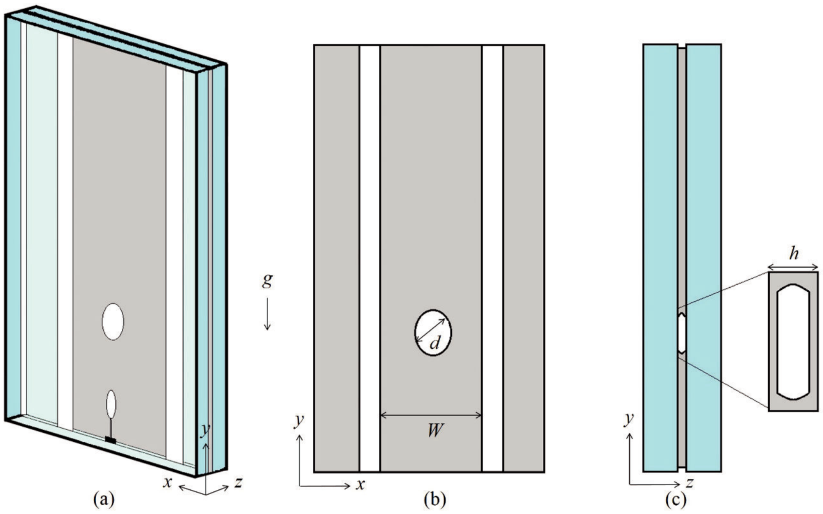

Figure 4.1: Illustration of a vertical Hele-Shaw cell. (a) isometric view; (b) front view; (c) side view. h gap thickness, d the equivalent bubble diameter, W cell width, g acceleration due to gravity.

In a Hele-Shaw cell, diverse bubble Reynolds numbers ($Re = u_b d/\nu$, u_b the bubble terminal velocity, ν the kinematic viscosity of the liquid) can be obtained by tilting the angle of the cell and changing the fluid viscosity. Most of the earlier studies focused on low Reynolds number bubble flow, using either an analytical approach or by doing experimens [54–56, 86, 88]. Later, intermediate Reynolds number bubble flow was studied [52, 58, 92]. The present study focuses on the high Reynolds number bubble flow in a vertical Hele-Shaw cell. It is fascinating and meaningful that the bubble in the cell is a two-dimensional analogue of an unconfined bubble with a higher interfacial area [110]. The two-dimensional bubble shape and terminal velocity were first studied by Davies & Taylor [23] and Collins [89]. Later, Lazarek & Littman [111] and Bessler & Littman [112] measured the pressure field by using pressure transducers. However, their studies only focused on the very large spherical-cap bubble. Recently, Kawaguchi's group and Roig *et al.* extended the studies to more types of bubbles by changing the initial bubble size [9, 59–61]. Furthermore, Roig *et al.* [9] measured the liquid perturbation by means of particle image velocimetry (PIV). However, in their experiments, the bubbles were observed only in a fixed gap thickness of $h = 1.0$ mm or 1.5 mm, yielding shape and path instabilities that are coupled over a wide size range. Yet for a more narrow gap thickness ($h = 0.5$ mm), bubbles can obtain both shape and path stability. This was shown in a previous study by the current authors [113]. The results suggest that the confinement of the gap thickness plays an important role in determining the bubble dynamics in a vertical Hele-Shaw cell. The relation between the gap thickness and the bubble dynamics, however, has not been investigated in detail for high Reynolds number flow.

In addition to the lack of experimental results on this relation, analytical descriptions of two-dimensional high Reynolds number bubbles only hold when the flow is simple. Therefore, only the spherical-cap bubble with a straight path has been studied theoretically with the spherical-cap shape being assumed a priori and surface tension ignored [23, 89, 114]. Later, it was proved [115] that the small surface tension of the spherical cap bubble plays a crucial role in determining the bubble terminal velocity. For a complete solution of the free-boundary problem, the boundary shape must be solved as a part of the overall solution, and only a numerical solution is possible. In a previous study, a numerical model was introduced that is able to predict bubble shapes in vertical Hele-Shaw cells filled with a low viscosity liquid [113]. Important to mention is that full wetting of the liquid on the cell surface is assumed. In this way, inconsistent behaviour induced by interactions with local defects and inhomogeneities of the cell surface is excluded. The present research extends the model to investigate the bubble motion induced liquid pressure and velocity fields and their interactions which have not been fully discovered by the experiments. Besides, the wake structure and vortex evolution in terms of gap thickness will be studied for a better understanding of the bubble dynamics.

4.2 Numerical simulation

Front-tracking methods, level-set methods and volume of fluid (VOF) approach are the three main methods available for gas-liquid multiphase flow with a sharp interface [64]. The VOF method is used in the present study due to its simplicity, robustness and intrinsic mass conservation [75].

In the present model, gas and liquid phases are considered as incompressible fluids, the flow is assumed to be laminar, surface tension σ is constant, the system is isothermal and constant fluid properties are applied. Furthermore, the thickness of the thin liquid films between the gas phase and the cell walls due to the total wetting of the liquid is neglected and three-dimensional effects caused by the curvature in the third dimension are not considered [113].

Based on these assumptions, the bubble in a vertical Hele-Shaw cell was simulated by a gap-averaged two-dimensional multiphase model. A single set of momentum and continuity equations for unsteady, incompressible, immiscible two-phase flow was applied for both phases. Two source terms were added in the Navier-Stokes momentum equation: one is for the surface tension in the plane, the other is to account for wall friction in the transverse direction. The surface tension along the interface between gas bubble and water was modelled by the continuum surface force (CSF) model proposed by Brackbill [66]. Darcy's law was used to calculate the in-gap wall friction due to the similarity between the Hele-Shaw cell wall resistance and porous media resistance. The governing equations, as well as the computational domain, boundary conditions and discretization method can be found in Ref [113]. Four gap thicknesses are simulated in the present paper, *i.e.*, h = 0.5, 0.7, 1.0 and 1.5 mm. In the previous studies, it was found that when $d \geqslant 5$ mm, three-dimensional effects are less significant, so the simulation results of bubbles with $d \geqslant 5$ mm are presented [113].

4.3 Experimental validation

Vertical Hele-Shaw cells with four different gap thicknesses (h = 0.5, 0.7, 1.0 and 1.5 ± 0.02 mm) have been constructed. The other two dimensions of the cells were each time left unchanged, *i.e.* 50 mm in width and 500 mm in height. The equipment is as described in Ref [62]. The cell was made of soda-lime glass with a thickness of 10 mm. The glass plates were washed in advance with Piranha solution (3:1 mixture of 96% H_2SO_4 and 30% H_2O_2) to remove organic residues and hydroxylate surfaces, making the plates highly hydrophilic. A bubble was generated with a syringe needle (inner diameter range 0.3–0.8 mm) controlled by an electromagnetic micro valve (brand is Bruker). By varying the time step of the valve and the needle inner diameter, the initial bubble size was controlled. Technically pure nitrogen gas (99.9%) and ultrapure water (18.2 MΩcm resistivity at 25°C produced by a Millipore Direct-Q 3 UV ultrapure water system) were used to avoid the effect of surface active agents. Thin liquid films were formed between the gas bubble and the wall due to the total wetting of water on the washed glass cell. The images of the bubble were recorded with a Tesin Cyclocam high speed video camera at a frame rate of 250 fps (resolution 640 × 480 pixels). The shutter time in the experiment was 2 ms. The recorded image frames were sequentially analysed with a MATLAB-based processing script. In each frame, the area S, and gravity centre (x, y) of the bubble were determined by mapping the bubble contour. The equivalent diameter d of the bubble was calculated as $d = 2(S/\pi)^{1/2}$; the vertical velocity uy as $u_y = \Delta y/\Delta t$ and the horizontal velocity u_x as $u_x = \Delta x/\Delta t$, where Δt is the time step.

4.4 Results and discussion

4.4.1 Bubble shape and path

The bubble shape and path at four different gap thicknesses are shown in Figure 4.2. For each gap thickness, four typical contours are selected and compared with experimental results.

When the gap thickness equals $h = 0.5$ mm (Figure 4.2a), the bubbles have two stable shapes: oblate ellipsoid and spherical-cap. Only rectilinear paths are observed for these bubbles. With an increase of h to 0.7 mm, the bubble becomes unstable comma-shaped and starts to vibrate when it is in the shape transition between oblate ellipsoid and spherical-cap. Simultaneously, the bubble rising path deviates from the rectilinear path (Figure 4.2b). However, the shape oscillation and path instability are limited and only happen in the size range of d = 9–11 mm. When $h = 1.0$ mm, the path evolution becomes quite different from the above two cases. Most of the bubbles are oscillating with a zigzag path except for very large bubbles (*e.g.* $d = 20$ mm in Figure 4.2c). The oscillation results in more complicated bubble shapes. Four bubble shapes are observed in both experiments and simulation: oblate ellipsoid, comma-shaped, bird flapping wings and spherical-cap as described in Refs [60] and [9]. The bubble shape and path when $h = 1.5$ mm are similar to that for $h = 1.0$ mm, *i.e.* small and medium size bubbles have zigzag paths, while the large bubbles (*e.g.* $d = 20$ mm in Figure 4.2d) show straight paths.

In all the cases, the simulation predicts similar bubble shape and path. Main differences are detected for large bubbles of $d = 20$ mm when $h = 1.0$ mm and h = 1.5 mm. The spherical-cap bubble exhibits a wavy (rippled) floor in the simulation, while the bottom of the bubble is flat in the experiment.

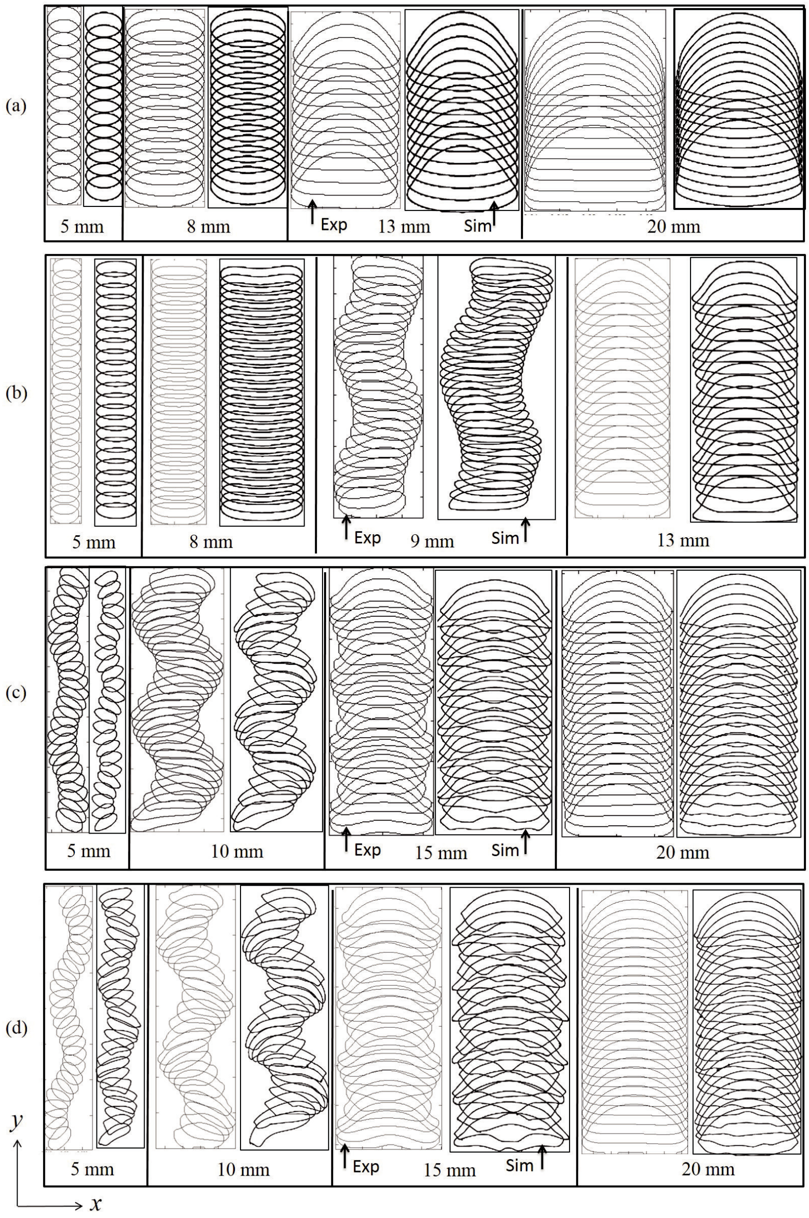

Figure 4.2: Comparison of bubble shape and path between experiment (left) and simulation (right): (a) $h = 0.5$ mm; (b) $h = 0.7$ mm, (c) $h = 1.0$ mm, (d) $h = 1.5$ mm. The successive contours are plotted at a time interval of 0.02 s.

4.4.2 Bubble Reynolds number and drag coefficient

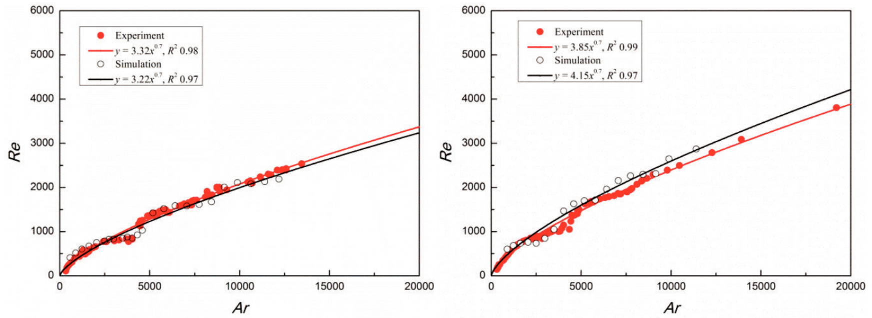

(a) h = 0.5 mm (b) h = 0.7 mm

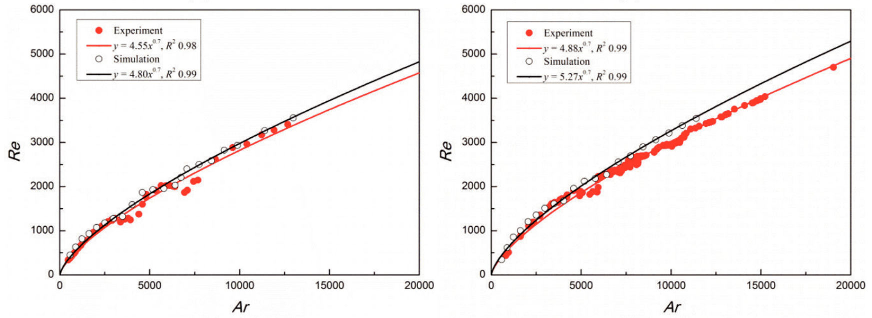

(c) h = 1.0 mm (d) h = 1.5 mm

Figure 4.3: Comparison of the Reynolds number Re as a function of the Archimedes number Ar: (a) gap thickness h = 0.5 mm, (b) h = 0.7 mm, (c) h = 1.0 mm, (d)h = 1.5 mm.

The governing non-dimensional numbers for a finite two-dimensional bubble in a vertical Hele-Shaw cell include the confinement ratios h/d and d/W, the Archimedes number $Ar = \sqrt{gd}d/\nu$ and Bond number $Bo = \rho g d^2/\sigma$ (ρ the liquid density, σ the surface tension). The Bond number is not independent of the Archimedes number because one fluid is used and therefore $Bo \approx Ar^{4/3}$ [9]. Besides, the bubble Reynolds number $Re = \rho u_b d/\mu$ is the most important parameter that characterizes the flow. To understand how it relates to the other numbers, the predicted and observed Re values are compared as a function of Archimedes number Ar (Figure 4.3). For all four gap thicknesses, the obtained Re lies in the high Reynolds number range ($100 < Re \leqslant 5000$), and therefore results in high Reynolds number bubble motion. As can be seen from Figure 4.3, Re increases with an increase in Ar for most of the Ar range. The Re values can also decrease with Ar in some limited Ar regions and this anomalous behaviour is linked to bubble shape regime transitions. As a whole, the Re and Ar relationship can be reasonably approximated by

$$Re = \varphi Ar^{0.7} \tag{4.1}$$

where φ is a constant. Its value depends on the gap thickness h, as listed in Table 4.1.

From the relationship, the bubble terminal velocity can be calculated as:

$$u_b = \varphi \mathrm{g}^{0.35} \nu^{0.3} d^{0.05} \tag{4.2}$$

Roig *et al.* [9] found experimentally that the bubble in a vertical Hele-Shaw cell is under the influence of buoyancy and drag force when the glass plates are clean and total-wetting. The force balance of the steady-state bubble in a Hele-Shaw cell can therefore be written as:

$$\rho \mathrm{g} \frac{\pi d^2}{4} h = \frac{1}{2} \rho C_D u_b^2 dh \tag{4.3}$$

where C_D is the drag coefficient which can be calculated as:

$$C_D = \frac{\pi \mathrm{g} d}{2u_b^2} \tag{4.4}$$

based on the obtained bubble terminal velocity V_b in equation 4.2, a simple correlation for the calculation of the drag coefficient C_D in equation 4.4 can be derived as:

$$C_D = \frac{\pi \mathrm{g}^{0.3} d^{0.9}}{2\varphi^2 \nu^{0.6}} \tag{4.5}$$

In terms of the Reynolds number, the correlation between the drag coefficient and the Reynolds number can therefore be expressed as:

$$C_D = \frac{\pi}{2\varphi^{2.86}} Re^{0.86} \tag{4.6}$$

From equation 4.5, both the gap-dependent constant φ and bubble size d determine the bubble terminal velocity and drag coefficient, but their effects are different: a thinner gap results in a lower terminal velocity and higher drag force, while a smaller bubble size causes both lower terminal velocity and lower drag force. The gap thickness is an important factor that influences the drag of the bubble. This effect is clearly confirmed by our experimental results as given in Table 4.1. By comparing the experimental results and the current simulation model, it is found that they have decent consistency with an average relative error below 8%. Equation 4.6 shows that the drag coefficient increases with increasing Reynolds number. By comparing the obtained drag coefficient with the one for the infinite two-dimensional one ($C_D = 2\pi$, for a cell with width $W = 40$ cm, gap thickness $h = 1.0$ mm in Ref. [9]), it is found that the drag coefficient is dependent on the bubble size or Reynolds number when the side wall spacing is finite. When the side wall effects are negligible, it is not related to the bubble size anymore.

Table 4.1: Comparison between experimental and predicted values of constant φ.

Gap thickness	Exp.	Sim.	Relative error, %
$h = 0.5$ mm	3.32	3.22	3.01
$h = 0.7$ mm	3.85	4.15	7.80
$h = 1.0$ mm	4.55	4.80	5.50
$h = 1.5$ mm	4.88	5.27	7.99

4.4.3 Pressure field and velocity field

To fully understand the bubble dynamics in a vertical Hele-Shaw cell, the pressure field and velocity field in the fluid have to be clarified since they determine the fluid motion, wake dynamics and bubble shape and path instability. However, the relevant experimental data is limited. For the pressure field, Lazarek and Littman [111] measured the pressure field around a large two-dimensional spherical-cap bubble in water. Later Bessler and Littman [112] extended this study for liquids of different viscosities and Raghunathan *et al.* [116] further extended to a liquid-solid system. In all these studies, only spherical-cap bubbles were observed. For the velocity field, Roig *et al.* [9] studied the velocity perturbation in the liquid by means of particle image velocimetry (PIV). However, simultaneous measurements on both fields have been found to be difficult since these two fields are intrinsically interactive and coupled. In the present model, except for the prediction of bubble shape, path and terminal velocity, the predicted pressure field and velocity field are also studied to further investigate the bubble-induced liquid fluctuation.

Figure 4.4 shows the simulated pressure field. The spherical-cap bubbles with diameter $d = 20$ mm are selected in all four gap thicknesses for two reasons: first, it allows for a qualitative comparison with the experimental measurements since only spherical-cap bubble pressure fields were experimentally observed; second, the spherical-cap bubble has a stable shape and rectilinear path, it makes a direct and quantitative comparison in different gap thicknesses possible. Nevertheless, no quantitative comparison between the predicted values and the mentioned available measurements is attempted since the boundary conditions of the cell width and cell gap thickness are quite different and they can be influential. To clearly show the flow-induced pressure fluctuation, the liquid hydrostatic pressure is subtracted, so therefore the modified pressure $p_{mod} = p - \rho g h$ is shown in the figure (see Figure 4.8).

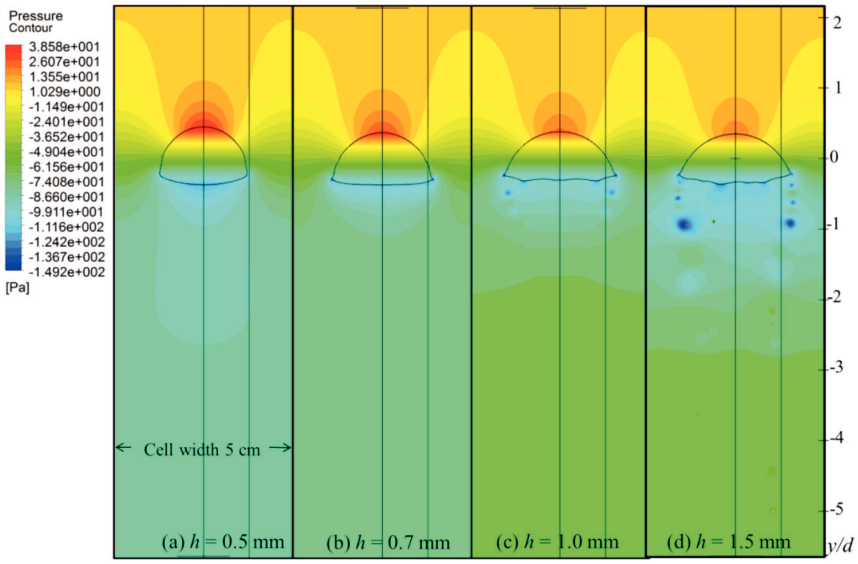

Figure 4.4: Simulated pressure fields for bubble diameter $d = 20$ mm. (a) gap thickness $h = 0.5$ mm, (b) $h = 0.7$ mm, (c) $h = 1.0$ mm, (d) $h = 1.5$ mm.

The entire pressure distribution around a spherical-cap bubble for four different gap thicknesses can be divided into three regions according to Lazarek and Littman [111], which include (a) the frontal pressure field, (b) the pressure field between the bubble cap and floor and (c) the pressure field behind the bubble. Above the bubble, a positive pressure (overpressure) is observed in the liquid region. The extent of the overpressure decreases as the position is farther removed from the bubble cap. Inside the bubble (away from the interface), the pressure inside the bubble is constant everywhere since the gas density is negligible. The pressure gradient in the figure is caused by the subtraction of $\rho g h$ (see Figure 4.7 in the appendix for the transformation). Behind the bubble, the pressure in the fluid is low and the pressure field gradually levels out in the liquid further away from the bubble. This pressure field can explain the force balance between gas bubble and liquid. Because the force on a fluid always points to the low pressure region, we can easily conclude that the liquid below the bubble will be filled up with surrounding liquid, and the liquid above the bubble interface will flow away. The liquid surrounding the bubble has a upward force. On the contrary, the gas bubble experiences a net downward force, which is the drag force. By comparing the pressure fields for the four gap thicknesses, it is observed that the increase of the gap thickness reduces the absolute values of the overpressure ahead of the bubble, leading to a drag reduction. Behind the bubble, local pressure minima are observed only when h = 1.0 mm and h = 1.5 mm. They refer to vortex cores as will be seen next in the velocity field.

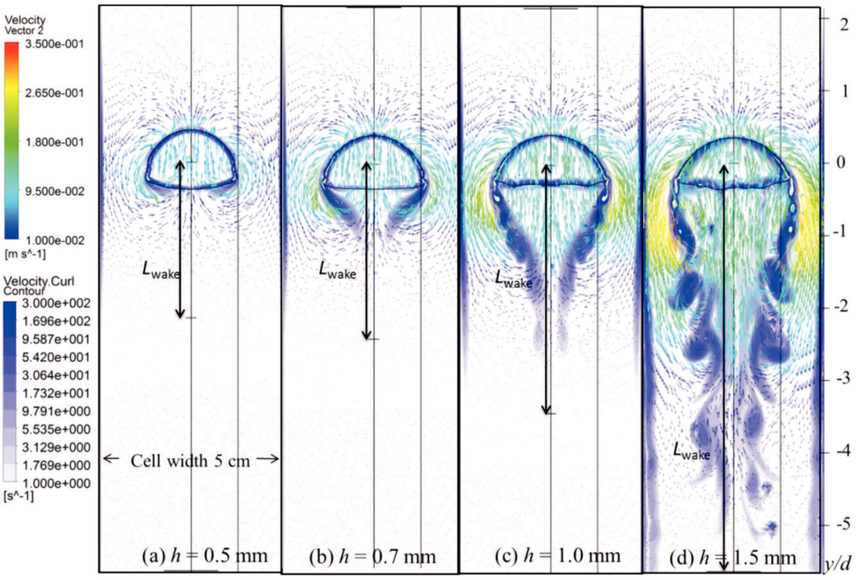

Figure 4.5: Velocity and vorticity contours in simulation for bubble diameter d = 20 mm. (a) gap thickness h = 0.5 mm, (b) h = 0.7 mm, (c) h = 1.0 mm, (d) h = 1.5 mm. The bubble centre in all these instantaneous contours is located in y = 0.15 m (y/d = 0).

The velocity field around bubbles with d = 20 mm for the four gap thicknesses are presented in Figure 4.5 in the form of velocity vector contours and velocity curl contours. In the figure, the contours of velocity vector $|\mathbf{u}| \geqslant 0.01$ m/s are shown. Vorticity is twice the local angular velocity in the flow, its contours are shown when $|\Omega| \geqslant 1$ /s.

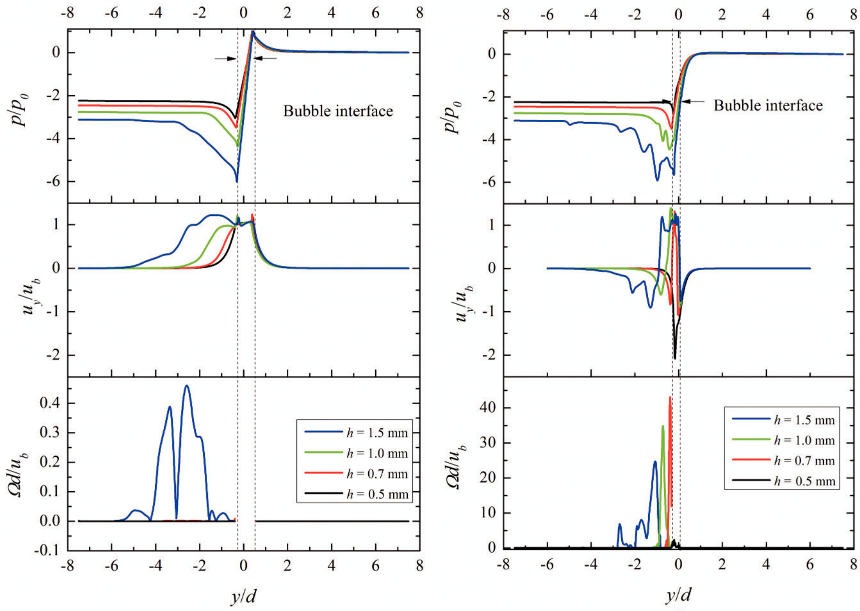

(a) (b)

Figure 4.6: Axial pressure, vertical velocity and vorticity distribution along (a) $x = 0.025$ m and (b) $x = 0.038$ m. Pressure p is normalized by the pressure at the bubble nose p_0. Vertical velocity u_y is normalized by bubble terminal velocity u_b, vorticity $\varOmega$ is normalized by using bubble diameter d and bubble terminal velocity u_b. y is normalized by bubble diameter d. $y/d = 0$ refers to bubble centre. $y/d < 0$ and $y/d > 0$ represent downstream and upstream, respectively.

In all four cases, the instantaneous velocity field is symmetrical, with a closed laminar wake behind the bubble. The frontal velocity distribution above the bubble is similar in the four cases, with a relatively lower magnitude when the gap is thinner. No vorticity is formed in the upper region, which means the flow in front of the bubble can be treated as irrotational. Behind the bubble, the wake structure in the four gap thicknesses varies substantially. One important wake parameter is wake length, it can directly show the extent of the liquid perturbation. In the figure the wake length when $|\mathbf{u}| \geqslant 0.01$ m/s is illustrated. It develops from $L_{wake} = 4.3$ cm (y/d = -2.2), when $h = 0.5$ mm to $L_{wake} = 11.3$ cm (y/d = -5.6), when $h = 1.5$ mm. The liquid velocity in the wake becomes higher and more unsteady with an increase of the gap thickness. The liquid can have a higher liquid velocity than the bubble terminal velocity when the gap thickness h reaches 1.5 mm. In addition to the wake length development, the vortices also evolve as the gap thickness is increased. In a narrow gap with $h =$ 0.5 mm, the vorticity behind the bubble is very small and no vortex cores are formed downstream of the bubble. With an increase of $h = 0.7$ mm, two parallel vortices are formed behind the bubble, and they are attached to both bubble edges and invariant with time. The two symmetric vortices extend further with wake shedding when the gap thickness $h = 1.0$ mm. The wake shedding becomes more unsteady and elongated for gap thickness $h = 1.5$ mm. The trailing vortices can coalesce and dissipate simultaneously with time, leading to irregular vortex shapes.

For a better understanding of the pressure-velocity coupling the liquid, the pressure, vertical velocity and vorticity distributions along two parallel vertical lines are shown simultaneously in Figure 4.6. One line is at $x = 0.025$ m which is the bubble's axis of symmetry along the bubble centre (see Figure 4.8 in the appendix for the pressure transformation). The other is at $x = 0.038$ m which is close to the vortex core. Their positions are illustrated in Figures 4.4 and 4.5. For a direct comparison, these variables are normalized to be non-dimensional.

The predicted vertical pressure and velocity show the following trends in the three regions: (a) upstream of the bubble, the pressure and velocity distributions in the four cases are similar, with a monotonically decreasing pressure and velocity along $x = 0.025$ m (the axis of symmetry) above the bubble nose and a monotonic increase in pressure and velocity along $x = 0.038$ m. The flow has no vorticity ahead of the bubble cap. Therefore the velocity field is irrotational and can be assumed as potential flow. The results resemble Lazarek and Littman's pressure measurements and Roig's velocity measurements qualitatively [9, 111]. Differently, due to the side-wall effects in our case, the upstream velocity reaches zero when $y/d \leqslant 2$, while it can extend to $y/d \leqslant 4$ in Roig's experimental measurements where side-wall effects are negligible. (b) The pressure inside the bubble increases linearly with increasing y/d. It means the pressure within the gas bubble is constant everywhere at a certain time. The velocity in the gas phase can be seen when $x = 0.025$ m. It is almost constant and equal to the bubble terminal velocity. (c) Downstream of the bubble, along the axis of the bubble ($x = 0.025$ m), minimum pressure is predicted just below the bubble interface and the pressure is recovered gradually when the liquid is away from the bubble. Due to the pressure modification, the pressure cannot be recovered to be zero (see Figure 4.8). The vorticity perturbation along the axis is quite small, so the pressure curve and velocity curve are smooth. The liquid velocity along the axis of the bubble centre is always positive, and it becomes zero when the liquid is distant from the bubble. The exact value of the distance y/d increases as the gap thickness increases. For $h = 0.5$ mm and $h = 0.7$ mm, $y/d =$ -2.2, $h = 1$ mm, $y/d =$ -3.4 and it increased to -5.6 when $h = 1.5$ mm (as also seen from the velocity contour). Beyond the critical value, the bubble induced velocity and pressure perturbation can be neglected. Besides, with an increase of the gap thickness, the liquid velocity in the vicinity of the bubble also increases. When $h = 0.5$ mm, the velocity dissipates very fast, with an increase to $h = 1.0$ mm, it can form a platform with a velocity value similar to bubble terminal velocity. When $h = 1.5$ mm, the value is 1.5 times higher than the terminal velocity. Additional information on the disturbance of the vortices to the pressure and velocity can be seen when $h = 0.038$ mm. The minimum pressure appears in the vortex centres instead of the bubble rear interface, which resembles the experimental observations of Raghunathan *et al.* [116]. It is accompanied by the velocity change from positive values to negative ones. Further downstream, there are small peaks in the pressure curve affected by the vortices. These vortices are not as sharp as the first ones with lower values of magnitude due to spatial decay.

4.5 Conclusions

Single bubble dynamics in vertical Hele-Shaw cells with varying thickness have been studied experimentally and by numerical simulation. A two-dimensional volume of fluid method coupled with a continuum surface force model has been applied to model the bubble characteristics such as shape, path and terminal velocity, as well as the bubble-induced liquid pressure filed and velocity field. After comparison and validation of the results with experimental observations, the relations between gap thickness and bubble dynamics and flow patterns in the liquid can be described as follows:

(1) two bubble shapes (oblate ellipsoid and spherical-cap) with a straight path are observed when $h = 0.5$ mm; three bubble shapes (oblate ellipsoid, spherical-cap and comma-shaped) with some vibrating paths ($d = 9$–11 mm) when $h = 0.7$ mm; while four shapes (oblate ellipsoid, comma-shaped, bird flapping its wings and spherical-cap) with strong path instability and shape oscillation for gap thicknesses h between 1.0 mm and 1.5 mm.

(2) the Reynolds number increases with increasing gap thickness. The scaling law $Re = \varphi Ar^{0.7}$ can be applied for the present confined two-dimensional bubble. The corresponding drag coefficient can be described as $C_D = \frac{\pi}{2\varphi^{2.86}} Re^{0.86}$. The increase of the gap thickness causes a monotonic increase in the constant φ, leading to a lower drag coefficient and higher velocity.

(3) lower pressure is observed in front of the bubble in a thicker gap, which is the main reason for the lower drag coefficient. The pressure in the wake also

varies. A pressure minimum is present when vortices exist and the numbers increase with increasing gap thickness.

(4) the wake length increases with higher liquid velocity when the gap thickness increases. A thicker gap thickness results in more vortices behind the bubble, meanwhile these vortices become more unsteady.

4.6 Appendix

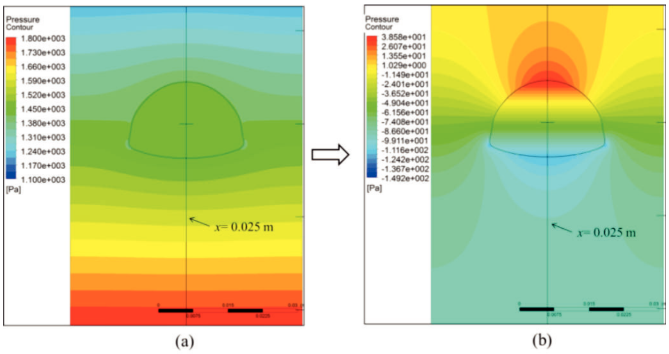

Figure 4.7: The pressure transformation in Figure 4.5. (a) The pressure p around the bubble (gauge pressure relative to the operating pressure). (b) The modified pressure $p_{mod} = p - \rho g h$ in Figure 4.5

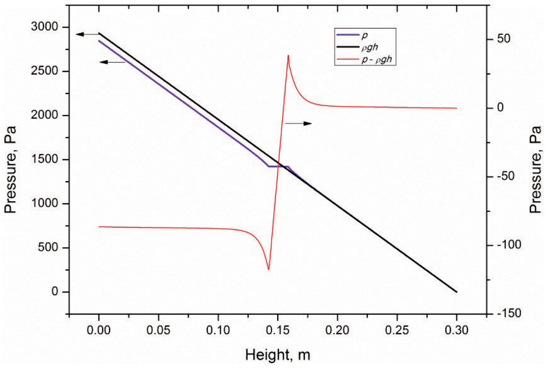

Figure 4.8: The pressure transformation along the symmetry line $x = 0.025$ m as shown in Figure 4.7.

Chapter 5

Drag Coefficient and Bubble Wake

Two-dimensional bubble characteristics in a Hele-Shaw cell were simulated to determine the effects of gap thickness h on the bubble velocity coefficient, to provide a quantitative description of the bubble wake dynamics and to compare the results with experimental data. It was found that the velocity coefficient decreases exponentially with $1/h$, resulting in an exponential increase of the drag coefficient. It was also found that in cells with a gap thickness $h = 1$ mm, periodic vortex shedding occurs when the bubble is small ($2 \leqslant d \leqslant 6$ mm, d bubble diameter) and follows a zigzag path. Intermediate bubbles ($6 < d \leqslant 12$ mm) with shape oscillation have only unsteady vortices close to the bubble interface, large spherical-cap bubbles ($d > 12$ mm) have only parallel trailing attached vortices. The vorticity decays exponentially with the diffusion time scale of $14t\nu/h^2$, which is faster than the experimental time scale of $6t\nu/h^2$, but close to the analytical time scale of $12t\nu/h^2$. The simulated vortices size is nearly half of the experimental value. The simulated longitudinal and transverse liquid velocities of the bubble follow trends similar to the experiments, although the exact values are not the same due to vortices size differences.

The results described in this chapter will be published in the following article:

X. Wang, B. Klaasen, J. Degrève, A. Mahulkar, G. Heynderickx, M.-F. Reyniers, B. Blanpain, F. Verhaeghe. A quantitative modelling of two-dimensional rising bubble dynamics: drag coefficient and bubble wake. (In preparation)

5.1 Introduction

Bubble wake plays a fundamental role in the fluid dynamics of multiphase systems [117]. Early in 1956, the effects of bubble wake on the bubble dynamics in gas-liquid two phase flow have been demonstrated by Saffman [38]. He pointed out that zigzag bubble motion is related to an oscillation of the wake or a periodic discharge of vorticity from the back of the bubble while the interaction of an oscillating wake and the instability of the motion near the bubble front results in the zigzag motion [38]. More recent studies also showed that wake instability causes path instability [33]. Therefore, a better understanding of the bubble wake is necessary for a thorough understanding of the bubble path. Besides its influence on the bubble behavior itself, the bubble wake also contributes to liquid mixing and turbulence production, and the velocity distribution in the wake region controls the diffusion of gas from bubbles into the liquid media [117]. That is to say, the heat and mass transfer efficiency in the system can be improved by the bubble wake. Even in gas-liquid-solid three phase fluidized beds, the bubble wake was also recognized as the key factor in explaining various phenomena such as solid mixing and particle entrainment [37].

Due to its importance and benefits, many studies have been devoted to understanding the bubble wake. In general, bubbles have different shapes like sphere, ellipsoid or spherical-cap, and their wake properties are different. The vortical structure and wake geometry of two-dimensional and three-dimensional spherical-cap bubbles were widely studied in the early days, and the main focus was on whether the vortex structure is open or closed and whether it is laminar or turbulent [37, 111, 112, 118–120]. More recently, the wake dynamics of zigzagging spheroidal bubbles was studied where it was shown that vortical structures exist behind the oscillating bubbles. Dye visualization [34], Schlieren photography [121] and PIV measurements [35, 122–124] have been used in these studies and they provide important information in the understanding of the wake structure and vortex formation-shedding mechanism. However, most of the studies provide only a qualitative description of the wake dynamics such as wake boundary and vertical geometry, while the quantitative observations of the liquid velocity and vertical strength in the liquid have seldom been conducted, due to the complicated 3D reconstruction. Among the techniques, PIV is able to measure the whole-field velocity instantaneously and therefore provides quantitative details of the wake dynamics, although the tracer particles are likely to contaminate the water [125]. Zenit and Magnaudet measured the vorticity strength of an oscillating ellipsoidal bubble [126, 127]. Their studies, however, only focus on one bubble shape, and the velocity field in the liquid is not measured . Roig *et al.* [9] provide the spatial and temporal decay of vorticity of the oscillating ellipsoidal bubbles, the longitudinal and transverse liquid velocity of the spherical-cap bubbles was measured as well, although the bubbles are confined in two dimensions.

The limitations in experimental measurements can be overcome by numerical simulations. The high spatial and temporal resolution of the simulated data allows for a detailed investigation of unsteady wakes and shape changes [81]. Meanwhile, the flow field and pressure distribution in the entire domain that are difficult to obtain from experiments can be easily obtained simultaneously in simulation. These results can be extended to other liquid-gas systems by only changing the corresponding physical properties. However, most of the numerical simulations are limited to a characterization of the bubble path and the time-averaged bubble velocity. Mougin and Magaudet examined the unsteady bubble wake of a spheroidal bubble, but the bubble shape was fixed with a prescribed aspect ratio [128]. Gaudlitz and Adams [81] investigated the unsteady open wake and unsteady shape changes in a zigzag ellipsoidal bubble and observed up to four hairpin vortices, however, the studies are limited to only one bubble size with one Reynolds number. Additionally, Zhang and Ni have presented the simulated bubble wake under a magnetic field [82]. Note that none of these studies have been validated by experiments.

This chapter is a follow-up work of our simulation effort to elucidate two-dimensional rising bubble dynamics [113, 129]. In the previous studies, the averaged bubble properties like bubble shape, bubble path, bubble terminal velocity and secondary motion have been simulated and validated with our own experimental results, meanwhile, the bubble wake was studied qualitatively by observing the vorticity distribution in the wake. However, these studies are confined in a narrow cell with finite width $W = 5$ cm. With a successful prediction of the averaged bubble characteristics in a narrow cell, we extend our studies to the unconfined two-dimensional bubble wake in a wide cell. The idea was motivated by the experimental measurements of Roig *et al.* [9], who measured both the vorticity strength evolution and liquid velocity induced by two-dimensional bubbles in a wide cell of $W = 40$ cm. Therefore, the main objective of the paper is to provide a quantitative simulation of the bubble wake structure. Meanwhile, the effects of the gap thickness on the bubble velocity and drag coefficient have also been studied for a better understanding of the two-dimensional bubble dynamics.

5.2 Numerical simulation

The two-dimensional bubble dynamics was simulated by the volume of fluid (VOF) method coupled with a surface tension model and a wall friction model.

The numerical method is identical to the one used in the previous studies in Chapters 3 and 4 and [113], with the exception of domain change. The domains of the two studies are shown in Figure 5.1. The previous study simulated the bubble dynamics in a Hele-Shaw cell with cell width $W = 5$ cm, while the present simulations were carried out in a cell with width $W = 40$ cm. The height of the simulated cell was the same as our previous studies for two reasons: firstly the height influence was small as proven in the previous study, secondly it allows for a direct comparison with our previous studies to investigate the side-wall effects. The detailed information on the assumptions, governing equations and discretization method can be found in [113]. An equal mesh size of 0.25 mm by 0.25 mm was used, which means 1920000 cells in total in the present study. Also a same time step of 0.0005 s was maintained. Five gap thicknesses were simulated, *i.e.* $h = 0.3$, 0.5, 0.7, 1.0 and 1.5 mm. Roig *et al.*'s experimental results [9] of $h = 1.0$ mm will be used for the validation of velocity coefficient and bubble wake. Our own experimental results of $h = 0.5$ mm in a same set-up with a different cell width $W = 20$ cm with the method described in [113] will be used to validate the velocity coefficient (this cell width is wide enough for the bubbles in the cell of $h = 0.5$ mm to exclude the side-wall effects). By doing so, we hope to generalize the unbounded two-dimensional bubble dynamics.

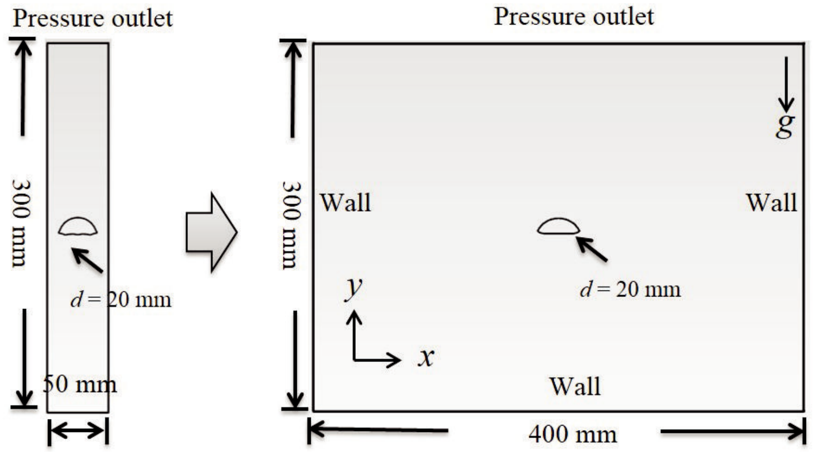

(a) $W = 50$ mm (b) $W = 400$ mm

Figure 5.1: The simulation domains (a) for the previous study in Chapters 3 and 4 and [113]; (b) for the present study. g gravitational acceleration.

5.3 Results and discussion

5.3.1 Bubble shape and path

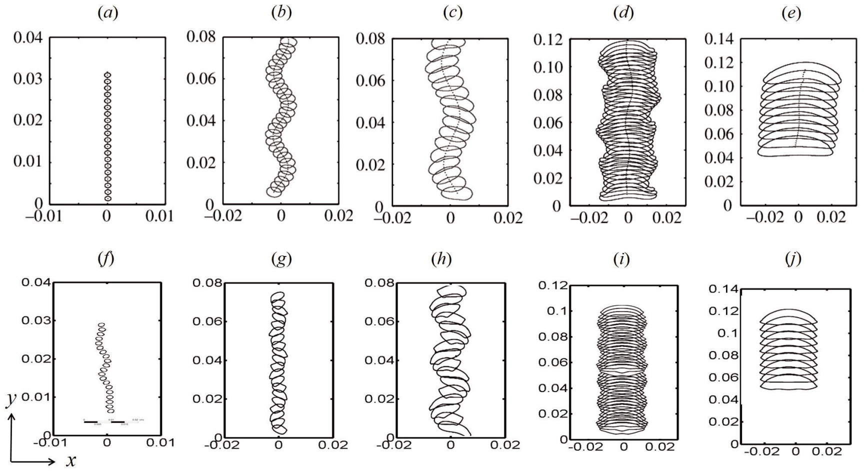

Figure 5.2: Comparison of bubble shape and path between experiment (a, b, c, d, e) and simulation (f, g, h, i, j). The time intervals of the simulated contours are kept the same as the experimental ones as illustrated in [9]. (a) The bubble diameter d = 1 mm, (b) d = 5 mm, (c) d = 8 mm, (d) d = 14 mm, (e) d = 19 mm, (f) d = 1 mm, (g) d = 5 mm, (h) d = 9 mm (the simulated bubble with d = 8 mm breaks up) , (i) d = 14 mm, (j) d = 19 mm.

The simulated bubble shape and path are compared with Roig *et al.*'s experimental data [9] (Figure 5.2). Similar bubble shape and path evolutions are predicted: the bubble shapes change from spherical and ellipsoidal to spherical-cap while the path changes from zigzag to rectilinear with an increase of the bubble size. We also noticed that there is some discrepancy between experiment and simulation: (1) The path for very small bubbles of d = 1 mm. In the experiment, these small bubbles have a rectilinear path, while in simulation, they are oscillating. Therefore, the transition from the rectilinear path to an oscillation path for small bubbles is not predicted correctly by the present model. (2) The bubble shape and the oscillation amplitude are not exactly the same, especially for a bubble size of d = 5 mm.

Three reasons can account for these deviations: (1) Three-dimensional effects are significant for small bubbles. (2) Surface tension in the experiment and simulation may not be the same: only distilled water instead of super-clean water was used in the experiment, therefore contamination may have an influence. (3) The current continuum surface force (CSF) based two-dimensional model itself cannot capture the subtle interfacial shape change and the shape-related path oscillation.

5.3.2 Bubble velocity coefficient and drag coefficient

The simulated and observed Re values are compared as a function of Archimedes number Ar (Figure 5.3a). Two gap thicknesses of $h = 0.5$ mm and $h = 1.0$ mm are compared here. The experimental results for $h = 1.0$ mm were obtained from Roig *et al* [9], and the experimental results for $h = 0.5$ mm were obtained from our own measurements. In both cases, the Re and Ar relationship can be described by the linear equation:

$$Re = \varphi Ar \tag{5.1}$$

where φ is the velocity coefficient. From the relationship, the bubble terminal velocity has the expression:

$$u_b = \varphi\sqrt{\mathrm{gd}} \tag{5.2}$$

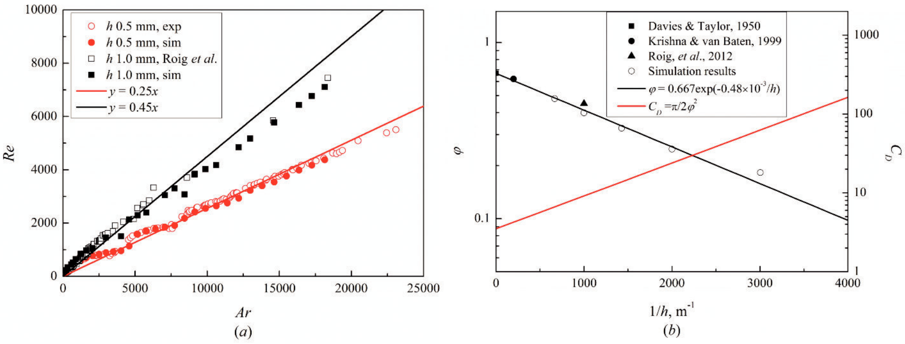

Figure 5.3: The Reynolds number Re as a function of the Archimedes number Ar in two gap thicknesses (a) and the velocity coefficient as a function of $1/h$ (b).

The obtained velocity coefficient φ from experiment takes the fitted values of 0.25 and 0.45 for $h = 0.5$ and 1.0 mm. The corresponding simulated values are 0.24 and 0.40, with average errors of 4% and 11%. By comparing the velocity coefficient change for the two gap thicknesses, it was found that the decrease of the gap thickness lowers the velocity coefficient. This is reasonable since smaller gap thickness leads to a higher viscous resistance exerted by the walls. To further discover the velocity coefficient evolution as a function of gap thickness, the simulated results of five gap thicknesses were presented, together with two velocity coefficient values from literature for $h = 5.0$ mm [98] and for real three-dimensions ($1/h = 0$ is assumed [23] Figure 5.3b). It was found that the velocity coefficient follows the equation:

$$\varphi = 0.667 \exp(-0.48 \times 10^{-3}/h) \tag{5.3}$$

i.e. the velocity coefficient attenuates exponentially as a function of $1/h$. With this relationship, the velocity in different gap thicknesses can be predicted and the overall drag coefficient change as gap thicknesses can be calculated. Roig *et al.* [9] found experimentally that the bubble movement within a thin gap is influenced by buoyancy force and drag force when the glass plates are clean and total-wetting, so the force balance leads to the equation for the drag coefficient C_D:

$$C_D = \pi/2\varphi^2 = 3.5e^{0.96\times10^{-3}/h} \tag{5.4}$$

Therefore, for a given bubble size with constant physical properties, the two-dimensional bubble velocity coefficient φ and drag coefficient C_D in a wide cell depend only on the gap thickness h. The decrease of the gap thickness will lead to an exponential decay of the velocity and corresponding exponential increase of the drag coefficient.

5.3.3 Bubble wake

In this part, the simulated bubble wake dynamics will be compared with Roig *et al.*'s experimental results quantitatively. Based on the available observations, the quantitative comparison is composed of three parts: (1) the instantaneous liquid velocity and vorticity contours, (2) the decay of vorticity, and (3) the instantaneous normalized longitudinal and transverse velocity fields in the liquid.

The typical velocity and vorticity contours are compared in Figure 5.4. In all five cases, vortices are formed in the bubble wake, and similar vorticity evolution as bubble size was found, *i.e.* the nature of the vorticity depends on the bubble size. For small bubbles of $d = 3.4$ mm and $d = 6$ mm, asymmetric vortices are shed periodically from alternating sides behind the bubble. These vortices become elongated and longitudinal with an increase of the bubble size. For the intermediate bubbles ($d = 9$ mm), the periodic property of the vortex shedding disappears and only the region near the bubble has the vortices. The vortices become more unsteady. Finally, for large bubbles, the shedding of the vortices disappears and two parallel vortices are attached to the bubble interface and are invariant with time. All these characteristics are reflected in the simulation, although the size of the shedded vortices is smaller in simulation than in experiment.

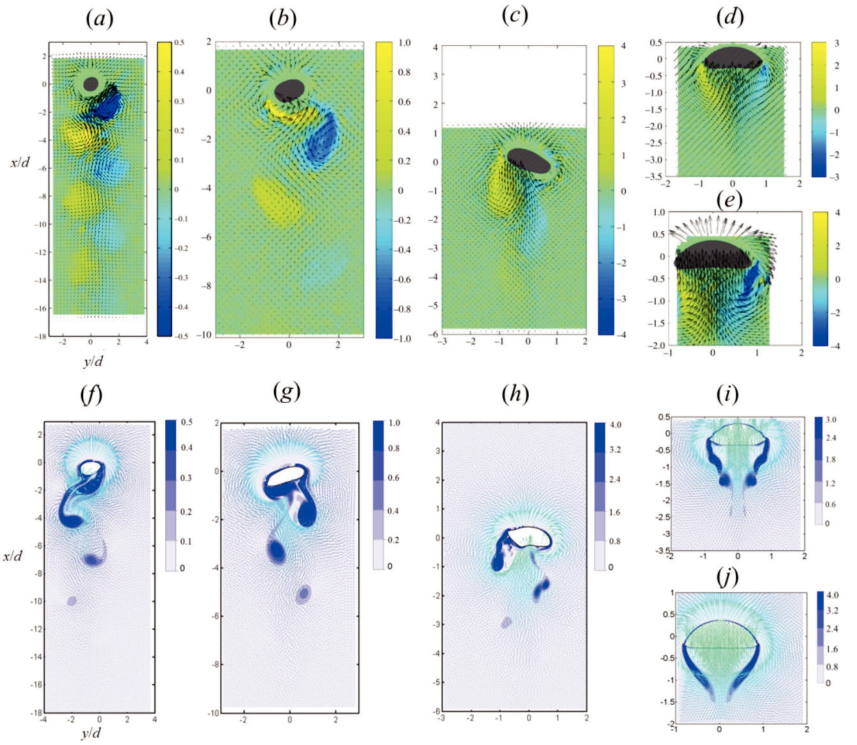

Figure 5.4: Comparison of the experimental (a–e) and simulated (f–j) velocity and vorticity around bubbles for $d = 3.4$ mm (a, f), $d = 6$ mm (b, g), $d = 9$ mm (c, h), $d = 16$ mm (d, i), and $d = 25$ mm (e, j). In all the figures, vorticity is normalized by u_b/d as in the experimental results. For a direct comparison, the same vorticity range is depicted.

Figure 5.5a illustrates the simulated decay of vorticity with time. For a direct comparison, the definitions of individual vortices and vortices size are kept the same as in Roig *et al.* [9]: the regions of vorticity exceeding one fourth of the maximum vorticity are assumed to contain individual vortices, and their size is defined from their area. In simulation, the decay of the vorticity was found to follow a similar exponential law as a function of the dimensionless time scale $t\nu/h^2$, which means the viscous shear stress exerted by the wall contributes to the fast decay of the vorticity. The decay follows the equation of $\Omega = \Omega_0\text{exp}(\text{-}14t\nu/h^2)$, close to the analytical results of $\Omega = \Omega_0\text{exp}(\text{-}12t\nu/h^2)$ with an assumption of parabolic flow in the gap and no diffusion in the plane [9]. However, the experimentally observed vorticity vanishes slower with a time scale of $6t\nu/h^2$. Roig explains this by pointing out that there is not enough time for the parabolic profile to develop. Figure 5.5b shows size evolution of the vortices. The overall vortices size is smaller than the experimentally observed ones. The experimental dimensionless vortices diameter has an average value of 2.5, while the simulated ones are in the range of 1.2–2 with an average value of 1.5. The size difference is also evident in the vortices contours in Figure 5.4. The smaller vortices size in simulation may link with the faster dissipation in the simulation. Besides, unlike the experimental measurements, the simulated vortices size has a slight increase with time.

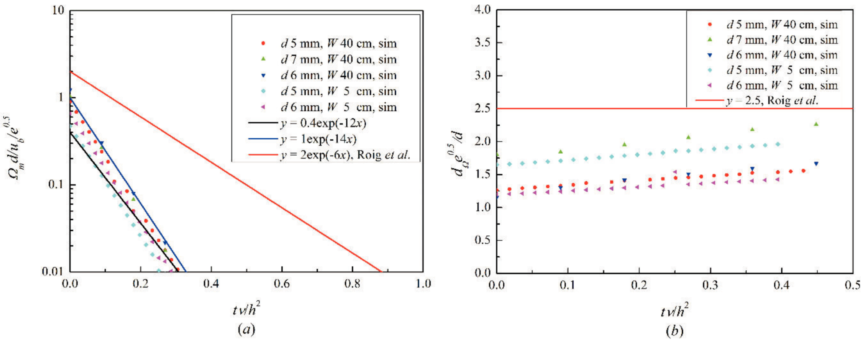

Figure 5.5: Comparison of the released vorticity properties. (a) Vorticity Ω decay with time. (b) Vortices diameter d_Ω with time.

Figure 5.6 shows the simulated longitudinal liquid velocity of two large bubbles with d = 16 mm and d = 25 mm. Upstream of the bubble, the velocity distribution is the same, with a monotonically decreasing velocity along the bubble centre. This can be described very well by the potential flow since there are no vortices above the bubble interface. Downstream of the bubble, the regions can be divided into three parts as proposed by Roig *et al.* [9]: (1) in the wake just beneath the bubble, there is a peak of the liquid velocity which leads to maximum liquid velocity. (2) further downstream the wake, the decay of the predicted liquid velocity also follows the exponential law of $u_y/u_b = \exp(-10y\nu/u_bh^2)$, when -0.36 $\leqslant y\nu/u_bh^2 \leqslant$ -0.2. (3) at the end of the wake, the decay of the liquid velocity slows down and depends on the bubble size (also the Ar number). All the three main properties of the longitudinal liquid velocity in the experiment can be simulated well by the present model. However, since the vortices size is different and the boundary condition may differ between simulation and experiment, the bifurcation positions where the liquid velocity becomes dependent on the bubble size are not exactly the same.

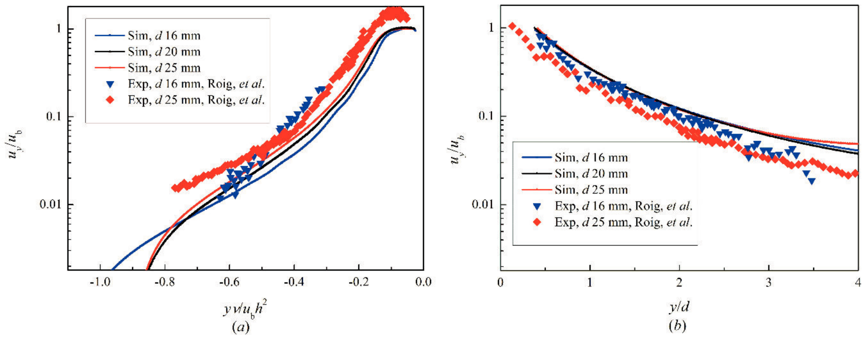

(a)
(b)

Figure 5.6: Comparison of the longitudinal velocity (velocity along the vertical symmetry line of $x/d = 0$ in Figure 5.4) between experiment and simulation for large bubbles. (a) Downstream of the bubble. (b) Upstream of the bubble.

The simulated transverse liquid velocity fields are shown in Figure 5.7. The vertical velocity u_y/u_{axis} and the horizontal velocity u_x/u_{axis} show different behaviour in the transverse direction. The vertical velocity u_y/u_{axis} distribution is axisymmetric along the symmetry line $x/d = 0$, while the horizontal velocity u_x/u_{axis} is point symmetric to the bubble centre. Meanwhile, the transverse velocity has the following characteristics in both simulation and experiment: (1) in the centre region of the wake ($|x/d| \leqslant 0.5$), the vertical liquid velocity u_y/u_{axis} is invariant except for $y/d =$ -1.06, and the velocity beyond certain $|x/d|$ can be negative due to liquid recirculation in the wake. (2) outside the attached wake, the liquid velocity u_y/u_{axis} is a linear function of y/d. (3) the horizontal velocity u_x/u_{axis} is perturbed by the vortices and shows peak values when it is close to the wake region when $y/d \geqslant$ -2. (4) the horizontal velocity u_x/u_{axis} becomes invariant with x/d when $y/d <$ -2. However, the exact $|x/d|$ and y/d values for these transitions are not the same in the simulation and experiment due to the wake scale differences, and the two linear lines of u_y/u_{axis} for $y/d =$ -2.67 and $y/d =$ -3.21 when $|x/d| \geqslant 0.5$ do not overlap as in the experiment, which means the in-plane diffusion is obvious in the simulation.

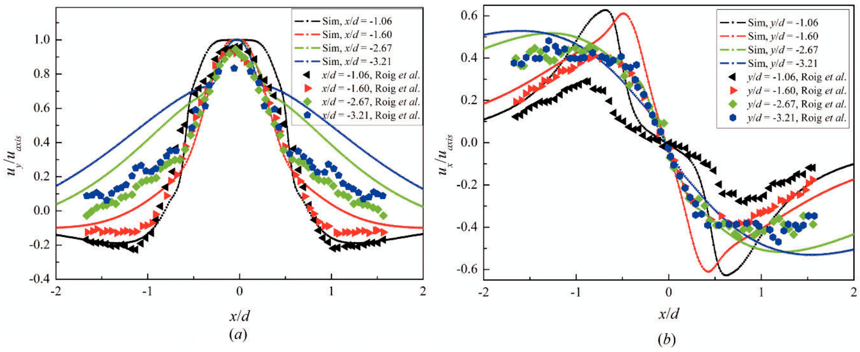

Figure 5.7: Comparison of the transverse velocity along four horizontal lines of constant y/d. (a) The vertical velocity u_y/u_{axis} in the liquid, (b) The horizontal velocity u_x/u_{axis} in the liquid. u_{axis} is the vertical velocity when $x/d = 0$ in each line.

5.4 Conclusions

The two-dimensional bubble dynamics within a thin gap has been simulated in the present study with an attempt to discover the relation between the gap thickness and the bubble terminal velocity and to quantify the bubble wake in a numerical way. The simulated bubble wake was compared with Roig *et al.*'s experimental data obtained by PIV measurements. The following conclusions can be drawn:

1. The average bubble terminal velocity can be predicted with an accuracy of 90%. It was found in the simulation that, for a given bubble size with constant physical properties, the velocity coefficient decreases exponentially with $1/h$, following an equation of $\varphi = 0.667\exp(-0.48\times10^{-3}/h)$. Consequently, the drag coefficient decreases exponentially with $1/h$.

2. The formation and shedding of the vorticity are predicted correctly. The shedded vortex in simulation was found to decay exponentially with time $14t\nu/h^2$, which is faster than the analytical results of $(12t\nu/h^2)$ and experimental results of $(6t\nu/h^2)$. The momentum diffusion in the in-plane direction may explain the discrepancy between the simulation results and the analytical results.

3. The longitudinal velocity and transverse velocity in the wake can be simulated well, the main properties and transitions in the experiment are captured. However, the exact position for the trends is not the same. The main reason may lie in the vortices size differences between experiment and simulation.

These discrepancies are acceptable since the boundary conditions and operating conditions in the experiment cannot be exactly extracted and applied during the simulation.

Chapter 6

2D Bubble Dynamics and Evaporation Simulation

Liquid evaporation into gas bubble at low saturation pressures plays an important role in many industrial processes. In this paper, the coupled problem of bubble dynamics and interface mass transfer was solved by the volume of fluid (VOF) model with a Hertz-Knudsen equation based evaporation model. The model can predict the bubble growth due to evaporation, as well as local concentration and temperature distribution. The effects of evaporation parameter, shape oscillation, bubble size and temperature were studied and it was found that the effect of the evaporation parameter can be quantified with an error function. In case of an extremely high evaporation parameter, the evaporation stops in a short time. Shape oscillation has limited effect on the overall evaporation rate but it can affect the concentration distribution and temperature in the wake. Small bubble size leads to fast evaporation and a more homogeneous concentration inside the gas phase. Bubbles in a high temperature fluid have a higher saturated vapour pressure, and more time is needed then to reach the steady-state.

The results described in this chapter will be published in the following article:

X. Wang, A. Mahulkar, B. Klaasen, J. Degrève, M.-F. Reyniers, B. Blanpain, F. Verhaeghe. Numerical simulation of bubble dynamics and evaporation. (In preparation)

6.1 Introduction

Liquid evaporation at low saturation pressures is of interest in a variety of fields such as hydrology, oceanography, and chemical engineering [130, 131]. Since Dalton's pioneering work in 1802, numerous studies have been devoted to the problem of evaporation to date [132]. In the case of evaporation, a molecule is transported across the interface between liquid and vapour phases [133]. Since the phases can be either dispersed or continuous, the evaporation may happen in all forms such as droplet, liquid film, free surface or bubble. The present study is motivated by the problem of gas injection in liquid Zn in pyro-metallurgical processes. Under these operating conditions, the liquid zinc will evaporate into the gas bubble and induce the mass transfer and reaction in the gas phase. Therefore, an accurate evaporation model for the rising gas bubble in the pure liquid is indispensable for an understanding of the whole process.

In a pure liquid, when the liquid saturated vapour pressure at the interface exceeds the partial pressure in the gas phase, evaporation occurs in the form of vapour to the gas phase. The vapour transports to the gas phase by diffusion and convection. The mass transfer is controlled by both the evaporation and mass transport in the gas phase. The bubble may grow in size if the saturated vapour pressure is high enough. In the bubble case, the mass transfer may depend on the bubble dynamic characteristics. For example, the area of the contact interface for evaporation is determined by the bubble size and shape, and normally the shape is not spherical unless the bubble diameter $d < 1.4$ mm [38]. The evaporation time is possibly dependent on the bubble rise velocity when the evaporation rate is moderate and a long evaporation time is needed. The vapour mass transport in the gas phase is affected by the internal gas recirculation. Meanwhile, the evaporation-induced bubble growth will in turn affect the bubble dynamics by changing its shape, velocity and wake. Therefore, the evaporation is a coupled problem of mass transfer and momentum transfer. Although the problem is quite common, however, the majority of the theoretical and experimental studies focused on other related phenomena such as nucleate boiling [134], film boiling, and evaporation in a liquid mixture. The fundamental problem of a free-rising gas bubble with evaporation is not well understood.

To solve the coupled problem of momentum and mass transport at the deformed interface, numerical simulation can be useful. Volume of fluid (VOF) and level-set (LS) methods have proven to be promising [84]. For example, in the studies of droplet mass transfer, Yang and Mao, as well as their colleagues [135–137] used a level-set method to study interfacial mass transfer from/to single drops in an immiscible liquid with resistance in both phases. Strotos *et al.* extended the studies to two-component droplet evaporation with the VOF methodology [138]. The methods are also widely used in studies on the mass transfer in film boiling [139, 140] and stratified flow [141–143]. For the bubble mass transfer, Kröger *et al.* [144] used a VOF-based approach to simulate the non-reactive or reactive mass transfer from a rising bubble to liquid. Ganguli and Kenig simulated an oxygen gas bubble diffusing into the continuous phase [84]. Alke also studied the mass transport of a diluted species in two-phase flows using a VOF-based approach [145]. Hardt and Wondra presented an evaporation model for microscale evaporation phenomena [146]. Jeon *et al.* studied condensing vapour bubbles using VOF model [147]. However, none of the studies have been extended to the bubble evaporation at low saturation pressures where the transport resistance in the gas phase is important.

In our previous studies, two-dimensional bubble hydrodynamics has been simulated and good agreement with experimental data was found [113]. In this study, we aim to couple the evaporation model into the existing VOF-based momentum model. The evaporation model is rather critical. Three main methods have been used to couple the evaporation at the interface, *i.e.* dimensionless numbers and correlations [147], Fick's law [145] and Hertz-Knudsen equation [131]. The use of dimensionless correlations is not advisable because it significantly depends on experimental conditions [148], so that reproducibility is difficult to ensure. A subtle difference in geometry and operation conditions may change the correlations. Additionally, dimensionless groups for the expanding evaporation bubbles are not readily available. In Fick's law, the local concentration gradient at the interface is used as driving force and the interface is assumed to be saturated [149]. It can be used only in dilute systems [145]. Moreover, the thickness of regions over which concentration and temperature gradients are significant is unknown and may extend to the micro-scale (μm) [148]. Sufficiently accurate resolution at the interface is thus difficult for our present meso-scale model. Therefore, the Hertz-Knudsen formula was used for the evaporation model. However, the shortcoming of the model is that the measurement of the evaporation coefficient in the Hertz-Knudsen formula can indicate a scatter over four orders of magnitude due to the effects of pressure, temperature, surface tension, *et al.* [150]. Therefore, the current model is not aimed to get an accurate evaporation coefficient for the bubble case, but to simulate the general bubble behaviour corresponding to a range of evaporation coefficients.

6.2 Numerical simulation

In this study, the unsteady interface evaporation and mass transfer to an initially inert two-dimensional rising nitrogen gas bubble will be simulated. To model the phenomena, the following assumptions are made: (1) the fluids are

Newtonian, viscous and incompressible; (2) the initial temperature in both phases is identical, and only the evaporation's induced latent heat is considered; (3) the physical properties including mass diffusivities and surface tension are constant and contamination is absent; (4) the flow is two-dimensional and laminar for both phases; (5) local thermodynamical equilibrium exists at the interface; (6) no chemical reaction is present in the system.

6.2.1 Governing equations

The governing equations are from ANSYS FLUNT Theory Guide.

VOF model

The VOF model is a fixed grid technique. The tracking of the interface between the phases is accomplished by the solution of a continuity equation for the volume fraction γ of the phases, this equation has the following form:

$$\frac{\partial(\rho_g \gamma_g)}{\partial t} + \nabla \cdot (\rho_g \gamma_g \mathbf{u}) = \dot{m}_g \tag{6.1}$$

$$\frac{\partial(\rho_l \gamma_l)}{\partial t} + \nabla \cdot (\rho_l \gamma_l \mathbf{u}) = \dot{m}_l \tag{6.2}$$

$$\dot{m}_g = -\dot{m}_l \tag{6.3}$$

Where $\mathbf{u}$ is the fluid velocity, t the physical time, ρ the density, and μ the dynamic viscosity. The subscripts g and l represent gas phase and liquid phase respectively. $\dot{m}_g$ is the mass transfer to the gas phase, $\dot{m}_l$ is the mass transfer to the liquid phase. γ the volume fraction of the second phase (gas phase) in the computational grid cell. *i.e.*, $\gamma = 0$, when the grid cell is full of liquid; $\gamma = 1$, when the grid cell is full of liquid; $0 < \gamma < 1$, when the grid cell is at the interface, which is partially filled with liquid. The volume fraction for the primary phase (liquid phase) is solved since the volume fraction of all phases sums to unity in each grid cell:

$$\gamma_g + \gamma_l = 1 \tag{6.4}$$

Momentum equation

In the VOF method, a single momentum equation is solved throughout the domain, and the resulting velocity field is shared among the phases. The momentum equation, is dependent on the volume fraction of all phases through the properties ρ and μ.

$$\frac{\partial}{\partial t}(\rho\mathbf{u}) + \nabla(\rho\mathbf{u}\mathbf{u}) = -\nabla p + \nabla\cdot \mu(\nabla\mathbf{u} + \nabla\mathbf{u}^T) + \rho\mathbf{g} + \mathbf{F}_\sigma + \mathbf{F}_w \tag{6.5}$$

g is the acceleration due to gravity, In our case, ρ and μ are taken constant in each fluid with a jump at the interface. They can be defined by:

$$\rho = \gamma\rho_g + (1-\gamma)\rho_l \tag{6.6}$$

$$\mu = \gamma\mu_g + (1-\gamma)\mu_l \tag{6.7}$$

$\mathbf{F}_\sigma$ denotes an additional surface tension source term. $\mathbf{F}_w$ is an additional in-gap wall friction source term. Their formulation can be found in Chapter 3 and [113].

Energy equation

Since the liquid evaporation to vapour gas is an endothermic process, there will be local temperature variation near the interface and in the surrounding bubble wake. The energy equation is also shared by the two phases:

$$\frac{\partial}{\partial t}(\rho E) + \nabla\mathbf{u}(\rho E + p) = \nabla\cdot(\Lambda\nabla T - \sum_j H_j J_j) + E_s \tag{6.8}$$

Where E is the energy, T the temperature, Λ the thermal conductivity. J_j is the diffusion flux of species j. E_s is the energy source term. Energy E and temperature T are mass-average variables as shown below:

$$E = \frac{\rho_l\gamma_l E_l + \rho_g\gamma_g E_g}{\rho} \tag{6.9}$$

with $E_l = H_l$ - $\frac{p}{\rho_l} + \frac{\mathbf{u}^2}{2}$ and $E_g = H_g$ - $\frac{p}{\rho_g} + \frac{\mathbf{u}^2}{2}$. The specific enthalpy H_i (i represents either g or l) is based on the specific enthalpy of that phase and the shared temperature, with the form:

$$H_i = \sum_j \omega_{i,j} H_{i,j} \tag{6.10}$$

and

$$H_{i,j} = \int_{T_{ref}}^{T} c_{p,j}\,dT \tag{6.11}$$

Where $\omega_{i,j}$ is the mass fraction of species j in phase i. c_p is the heat capacity. T_{ref} is 298.15 K.

Species equation

The species equation will be solved only in the gas phase since the liquid phase is pure, and the gas phase contains the mixtures of vaporized liquid component and inert gas. Therefore, inside the gas phase, the transport of species j is governed by the local balance equation:

$$\frac{\partial}{\partial t}(\rho_g \gamma_g \omega_{g,j}) + \nabla(\rho_g \gamma_g \mathbf{u} \omega_{g,j}) = -\nabla \cdot (\gamma_g J_{g,j}) + \dot{m}_{g,j} \tag{6.12}$$

The diffusion flux term $J_{g,j}$ that appears is given by:

$$J_{g,j} = -\rho_g D_j \nabla \omega_{g,j} \tag{6.13}$$

Where D_j is the mass diffusion coefficient for species j in the binary mixture.

Evaporation model

One of the most important parts of the simulation is the choice of evaporation model. A user-defined function is coupled to the existing bubble dynamics model and the mass transfer rate is calculated only at the interface. To add the evaporation model, three steps need to be followed: (1) find the interface grid cells; (2) calculate the normal interfacial mass transfer area A; (3) add the evaporation equation. The codes for steps (1) and (2) can be found in the Appendix B. Here only the equations for the evaporation model are introduced.

The Hertz-Knudsen equation for the net mass flux J$'$ over the vapour-liquid interface is described by [131]:

$$J' = \frac{2\eta}{2-\eta} \frac{\sqrt{M}}{\sqrt{2\pi R}} (\frac{p_{sat}(T_l)}{\sqrt{T_l}} - \frac{p}{\sqrt{T_v}}) \tag{6.14}$$

Where η the evaporation coefficient, M the molar mass, R the universal gas constant. p_{sat} the saturated vapor pressure of the liquid temperature T_l . p is the partial pressure of the evaporating component in the gas phase. In the calculation, the temperature variation between gas phase and liquid phase is very small, therefore, the evaporation coefficient can be simplified to:

$$J' = \frac{2\eta}{2-\eta} \frac{\sqrt{M}}{\sqrt{2\pi R T_l}} (p_{sat} - p) = c(p_{sat} - p) \tag{6.15}$$

where the evaporation parameter $c = \frac{2\eta}{2-\eta} \frac{\sqrt{M}}{\sqrt{2\pi R T_l}}$. Therefore the volume based mass transfer source term:

$$\dot{m} = J' \frac{A}{V_{cell}} \tag{6.16}$$

And the energy source term:

$$S_e = -\dot{m}\Delta H_{vap} \tag{6.17}$$

where A is the interface area of the bubble, V_{cell} the volume of the grid cell, ΔH_{vap} latent heat.

6.2.2 Simulation strategies

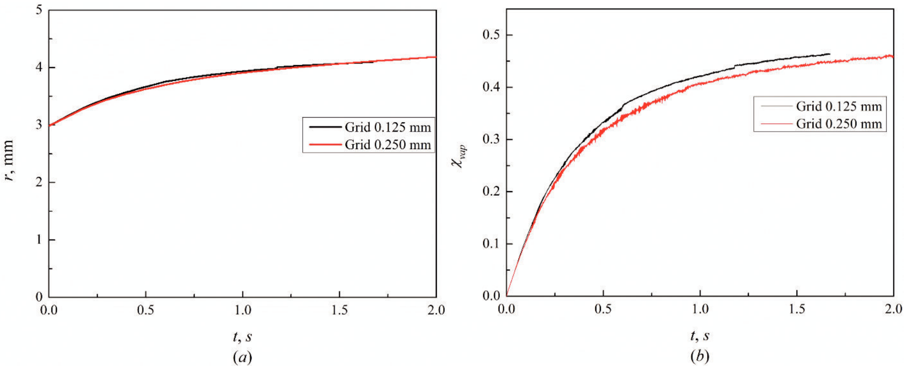

Figure 6.1: Check for grid independence results. (a) Bubble radius r evolution with time. (b) Evolution with time of water vapour mole fraction χ_{vap} in the bubble.

The simulation was based on our previous two-dimensional bubble dynamics model [113]. In addition, species transport model, energy model, together with an interface evaporation model are coupled in the VOF model. The computational domain was composed of 50 mm in width by 500 mm in height. The height is 200 mm more compared with the previous dynamic models for a better observation on the bubble evaporation process. Therefore, the total bubble rising time was increased. In the simulation, liquid water was used instead of liquid metal to reduce the effects of the hydrostatic pressure on the bubble expansion. The domain was filled with stationary water and a spherical bubble was introduced in the bottom centre of the domain as described in the previous studies. At the same time, the interface mass transfer was initialized. The operating pressure was 1 atm. No-slip boundary conditions were applied at all walls. Except for the properties of density and viscosity given in Chapter 3 and [113], the other physical properties of the system can be found in Appendix A. For the gas-phase mass transfer, the gas Schmidt number Sc ($Sc = \nu/D$,

ν the kinematic viscosity, D the mass diffusivity) has the order of 1, *i.e.*, the concentration boundary layer has approximately the same thickness as the momentum boundary layer. Therefore, there is no need to decrease the mesh size to capture the mass concentration gradient induced by the interface evaporation. The discretization method and calculation method are the same as in the previous publication, and the same time step of 0.0005 s was used. To test the grid independence, the mesh size was refined from 0.25 mm to 0.125 mm and their results are compared in Figure 6.1. The difference in predicted bubble radius can be neglected and the difference for the averaged water vapour mole fraction is within 5%, therefore the grid independence was satisfied. However, if the resistance to mass transfer is mainly in the liquid phase, a finer mesh for mass transfer will be required in order to capture the steep concentration profile in the direction normal to the phase boundary [83].

6.3 Results and discussion

6.3.1 Effect of evaporation parameter

It is well known that the evaporation coefficient η can be greatly influenced by many factors such as pressure, temperature, curvature of the interface, surface active substances and impurities [151]. Therefore, the evaporation coefficient can vary substantially in a range. It is not the scope for the current simulation to find an accurate evaporation coefficient for the bubble evaporation since it is an input rather than an output. For an accurate estimation of the evaporation coefficient, experimental measurement or molecular dynamics simulation is recommended [152]. It is therefore more meaningful in our simulation to find the overall effect of evaporation coefficient on the bubble evaporation process. The highest evaporation coefficient cannot exceed the values of Badam *et al.*'s measurement [153]. They measured the evaporation under a very low pressure of less than 1000 Pa. The evaporation parameter c is in the range of 1–5 $\times$ 10^{-5} s/m . In case of surface contamination, the evaporation can also be reduced by some orders of magnitude. Therefore, the evaporation parameter c in the simulation was set changed from 10^{-6} s/m to 10^{-9} s/m. The simulation was carried out for a bubble with an initial bubble size of $d = 6$ mm in a cell of gap thickness $h = 0.5$ mm. The initial temperature is set to 356 K, with a saturated vapour pressure for water of 0.5 atm.

From the simulation results (Figure 6.2), it can be seen that in larger values of the evaporation parameter the bubble evaporation process is greatly enhanced. When the evaporation parameter is higher than 10^{-7} s/m, the evaporation process reaches the steady state within 1 s. With a decrease of the evaporation parameter, the evaporation process slows down. In all cases, it was found that the averaged mole fraction curve as a function of time can be approximated by the error function:

$$\frac{\chi_A}{\chi_{A0}} = \operatorname{erf}\frac{0.000211/\sqrt{c}}{\sqrt{t}} \tag{6.18}$$

The fitting for very low values of evaporation parameter is less satisfactory as compared to that for the higher evaporation parameter values.

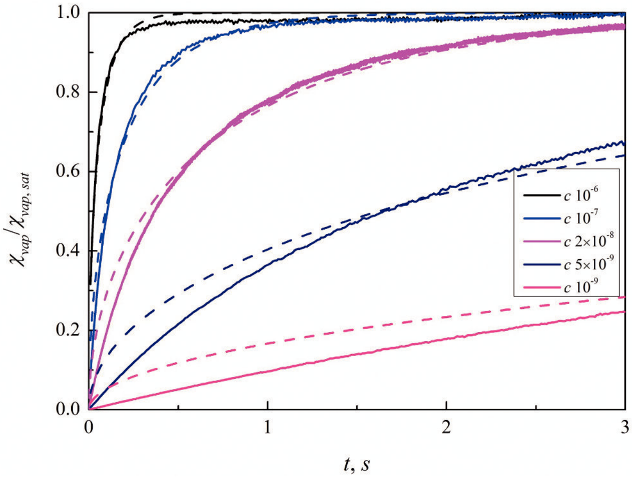

Figure 6.2: Values of the dimensionless mole fraction evolution with time for different evaporation parameter c. The dashed lines show the predicted evolution according to Equation 6.18.

6.3.2 Concentration and temperature distributions

Although the evaporation coefficient can vary over several orders of magnitude, a reasonable value for bubble evaporation in our case is needed. The evaporation process for a bubble of diameter $d = 6$ mm in a Hele-Shaw cell with gap thickness $h = 0.5$ mm was studied. The initial temperature is set to 356 K, with a saturated vapour pressure of 0.5 atm. Since no experimental data is available for the evaporation parameter of bubbles, therefore, the evaporation parameter under similar operating conditions of a flat interface was adopted. Pauken [130] investigated the evaporation for a moving air stream at atmospheric pressure. The correlation based on the experimental measurements is $J = a(p_{sat} - p)^b$, where a and b are a function of gas velocity u ($a = 2.06 \times 10^{-8} + 2.72 \times 10^{-8} u +$

$6.90 \times 10^{-9}u^2$, $b = 1.22 - 0.19u + 0.038u^2$, when J is given in kg/(m^2·s), p_{sat} and p in Pa, and u in m/s). He pointed out that the exponent

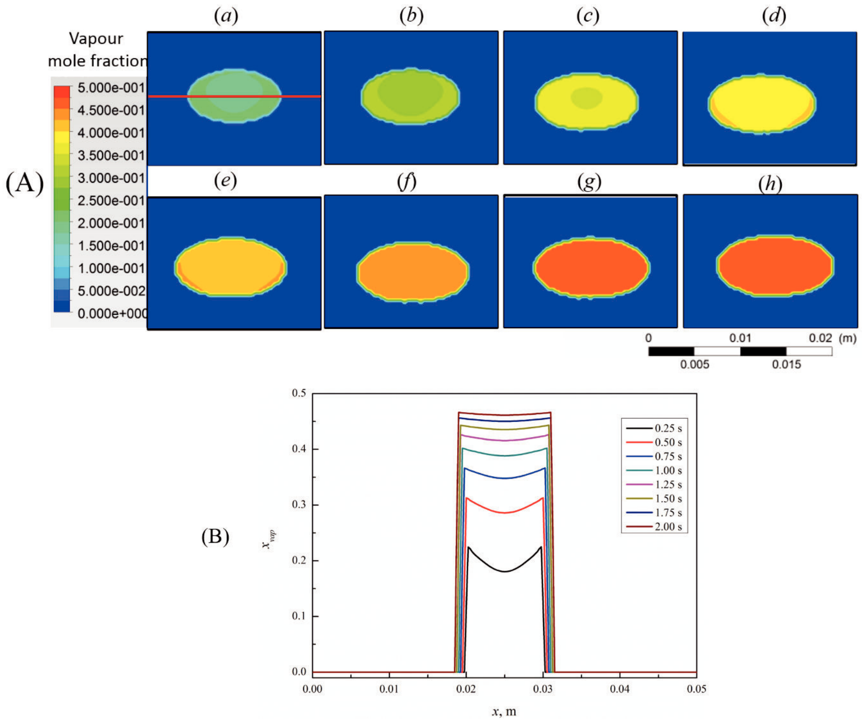

Figure 6.3: Simulated vapour mole fraction contours at different times (A) A bubble with diameter $d = 6$ mm in a cell of gap thickness $h = 0.5$ mm. (a) 0.25 s. (b) 0.5 s, (c) 0.75 s, (d) 1 s, (e) 1.25 s, (f) 1.5 s, (g) 1.75 s. (h) 2.0 s. (B) The time evolution of mole fraction distribution along the horizontal bubble symmetry line illustrated in (A).

b usually takes a value between 1.2 and 1.3, and is caused by the free evaporation during the experiment. In our case, there is no temperature gradient induced free evaporation, the function of $J = a(p_{sat} - p)$ is therefore adopted in our case, *i.e.* $c = a$. The bubble terminal velocity was used for the calculation of the gas velocity in bubble near the gas bubble/liquid interface. The calculated evaporation parameter c equals 2.34×10^{-8} s/m when the bubble terminal velocity of 0.1 m/s was used. In fact, within the velocity range of 0.01–0.20 m/s, a changes in a relatively narrow range of 2.10–2.60 $\times 10^{-8}$ s/m. Therefore the bubble velocity induced evaporation coefficient change in the calculation can be neglected. The simulated bubble vapour concentration contour with $c = 2.34 \times 10^{-8}$ s/m is shown in Figure 6.3, together with scale of numerical values. The vapour concentration increases gradually with time, and the composition inside the bubble approaches a homogeneous distribution. After 1 s, the concentration difference from bubble interface to the bubble centre becomes negligible. With the increase of the vapour mole fraction inside the bubble, the bubble size also increases gradually due to the mass transfer from the liquid phase.

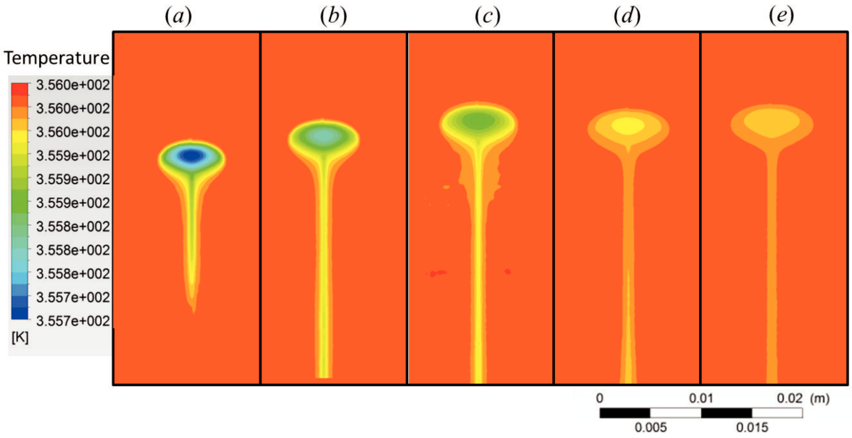

Figure 6.4: The simulated temperature distribution contours at different time for bubbles in Figure 6.3. (a) 0.25 s. (b) 0.5 s. (c) 0.75 s, (d) 1.75 s, (e) 2.0 s.

The initial temperature distribution is uniform. After initialization, the endothermic evaporation gives rise to local temperature variation. Figure 6.4 shows the temperature contours corresponding to simulated concentration contours in Figure 6.3. The overall temperature variation is very small, within 0.5 degree. The temperature distribution in the liquid resembles the bubble wake. This temperature distribution is similar to the measured concentration distribution in the bubble wake in Figure 2.7 and [154]. Inside the bubble, it is surprisingly found that the lowest temperature is obtained at the bubble centre while the temperature close to the bubble rim is higher although the magnitude difference is indeed very small. Normally the bubble interface should have a temperature drop due to evaporation. To find out how the non-intuitive temperature distribution was developed, the temperature evolution at the beginning of the bubble evaporation is shown in Figure 6.5.

The initial temperature is constant and uniform before evaporation. During evaporation, the temperature of neighbouring cells close to the bubble interface starts dropping, forming a low-temperature layer at the interface. The thickness of the layer increases over time, approaching the bubble centre. With further mass transfer, the centre gradually forms a low temperature core since the vapours close to the bubble rim can absorb the heat from the interface. Therefore, the temperature in the centre becomes the lowest. Two reasons contribute to this counter-intuitive temperature distribution. First, in the VOF method, the gas and liquid at the interface cells share one temperature, therefore, the gas temperature at the interface can be increased by the liquid temperature in the cell. Second, the spurious currents near the bubble rim in the CSF model in Figure 3.7 can also lead to spurious heat transfer at the interface which induces an artificial increase of the temperature.

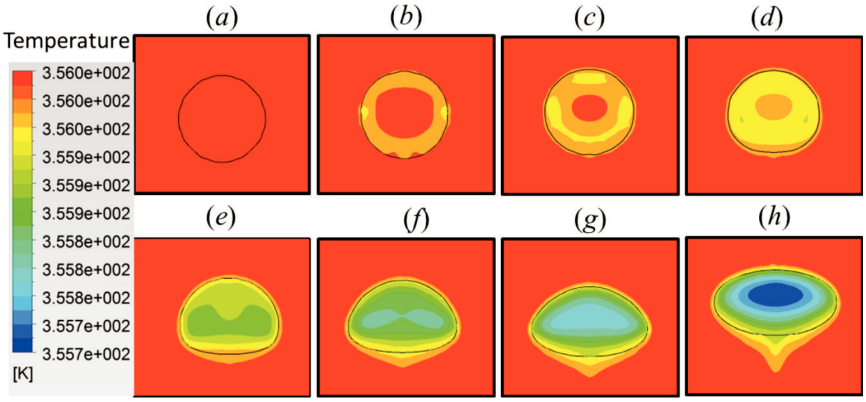

Figure 6.5: The temperature contour evolution at the early stage of the evaporation process. (a) 0 s. (b) 0.01 s. (c) 0.015 s. (d) 0.02 s. (e) 0.04 s. (f) 0.045 s. (g) 0.05 s. (h) 0.075 s.

6.3.3 Effect of shape oscillation

Figure 6.6 and Figure 6.7 illustrate the concentration and temperature contours for an oscillating bubble. The same initial temperature and evaporation coefficient were adopted. The simulated bubble with initial diameter $d =$ 6 mm was placed in a cell with gap thickness $h = 1.0$ mm. Different from the bubbles without oscillation, the fast shape expansion here leads to bubble break-up and very unsteady bubble shapes. The mole fraction inside the gas bubble is higher compared to the non-oscillating bubbles, with a maximum difference of 5%. The mass transfer improvement is not readily apparent since the mass transfer in a non-oscillating bubble is already very fast. In other words, the effects of oscillation on the gas phase mass transfer process are limited in this case. Despite the small enhancement to the mass transfer in the gas phase, oscillation changes the temperature distribution in the liquid. The temperature in the liquid is quite different from the cases of $h = 0.5$ mm (Figure 6.4). This temperature distribution difference lies in their vortical structure differences. Only the regions with vorticity have a lower temperature. It turns out that the wake structure determines the heat and mass transfer inside the liquid.

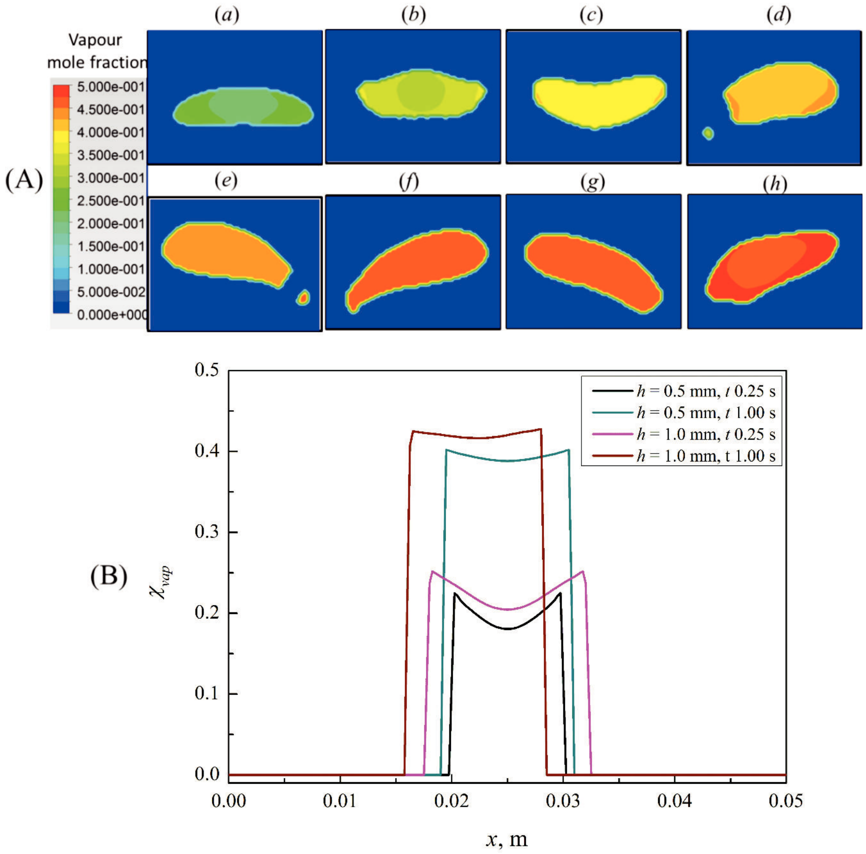

Figure 6.6: The simulated vapour mole fraction contours at different times. (A) For a bubble with initial diameter $d = 6$ mm in a cell of gap thickness $h = 1.0$ mm. (a) 0.25 s. (b) 0.5 s. (c) 0.75 s, (d) 1 s, (e) 1.25 s, (f) 1.5 s, (g) 1.75 s. (h) 2.0 s. (B) The mole fraction distribution along the horizontal bubble line together with the results for $h = 0.5$ mm.

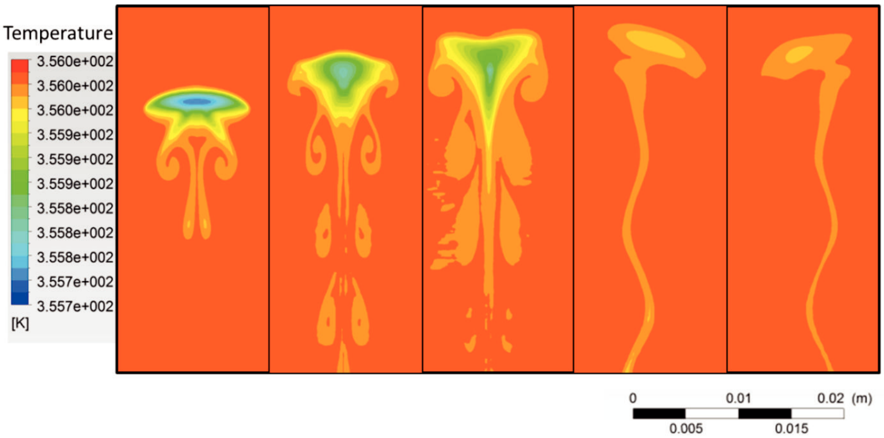

Figure 6.7: The simulated temperature distribution contours at different time with shape oscillation. (a) 0.25 s. (b) 0.5 s. (c) 0.75 s, (d) 1.75 s, (e) 2.0 s.

6.3.4 Effect of bubble size

Figure 6.8 illustrates the concentration contours for the different bubble sizes. For a bubble of $d = 3$ mm, the concentration in the bubble can to be assumed constant all the time. With an increase of the bubble size, the concentration gradient inside the bubble becomes pronounced. At $t = 0.25$ s (Figure 6.8B), the bubble centre of $d = 25$ mm is still free of water vapour. This transport difference can be approximated analytically by the unsteady diffusion in a sphere: when the dimensionless time $\tau = Dt/R^2$ is 0.04, the diffusion starts to reach the sphere's centre, and when the dimensionless time τ is 0.4, the diffusion in the sphere's centre is 95% complete. Therefore, for a spherical bubble with $d = 3$ mm, the analytical time for 95% completion is $t = 0.03$ s. After this short time span, the concentration can be treated constant all the time. For a spherical bubble with $d = 25$ mm, the analytical time for when the diffusion starts to reach the bubble centre is 0.22 s, which is close to our simulation results with $t = 0.25$ s. The longer transport time in simulation can be explained by two reasons: first, the bubble is expanding in the simulation, therefore it takes a longer time to transport; second, the bubble is not perfectly spherical.

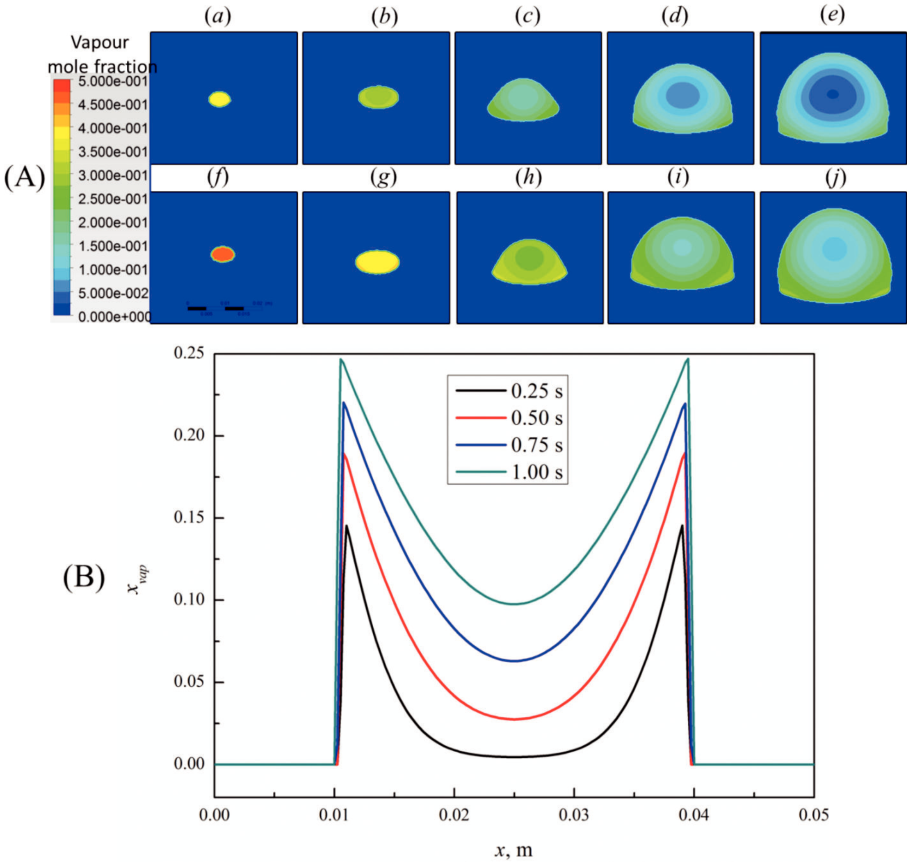

Figure 6.8: The simulated vapour mole fraction contours for bubbles (A) with different sizes at time $t = 0.25$ s (a–e) and $t = 1.0$ s (f–g). (a) and (f) $d = 3$ mm. (b) and (g) $d = 6$ mm. (c) and (h) $d = 12$ mm. (d) and (i) $d = 20$ mm. (e) and (f) $d = 25$ mm. (B) the mole fraction distribution along the horizontal bubble line for bubble of $d = 25$ mm.

Due to the mass transport difference inside the gas bubble, the averaged vapour concentration inside the gas bubble is highly dependent on the initial bubble size (Figure 6.9). The concentration difference shows up immediately at the beginning of the process. At $t = 0.5$ s, the dimensionless average mole fraction for bubble with $d = 3$ mm is 0.75, while the value for $d = 25$ mm is only 0.20. The difference gradually decreases with an increase of the time.

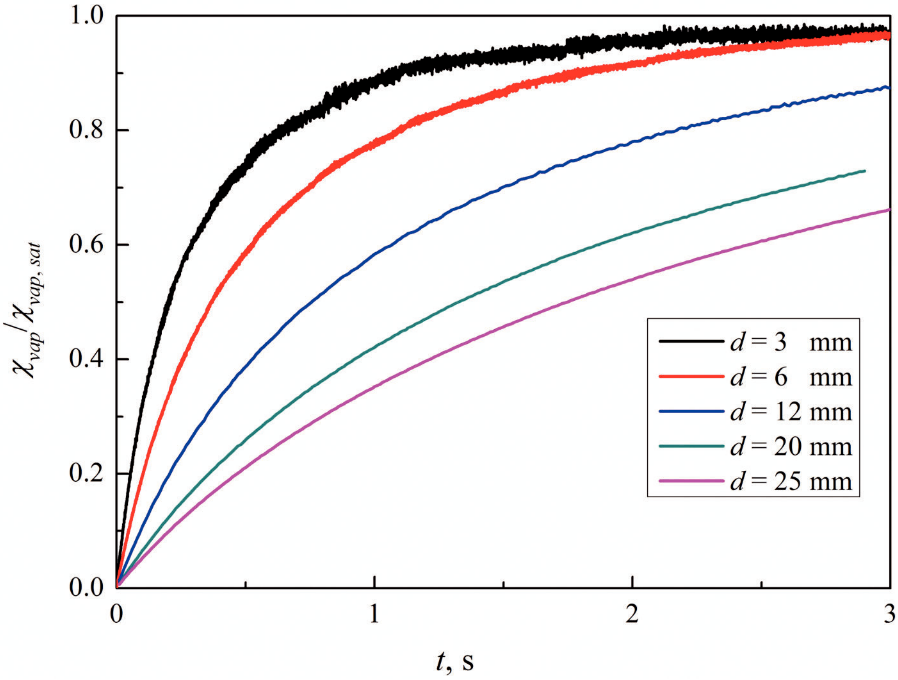

Figure 6.9: The averaged dimensionless vapour mole fraction as a function of time. The vapour mole fraction is normalized by the saturated mole fraction, therefore the maximum value is 1 when the evaporation is complete.

6.3.5 Effect of temperature

The effect of temperature IS shown in Figure 6.10. The bubble size is kept the same of $d = 6$ mm for all cases. Four temperatures were studied, representing four different saturated vapour pressure. As can be seen, the increase of the operating temperature increases the saturated vapour pressure, and it takes longer time to reach equilibrium. At the beginning, the curves are overlapped and their differences can be neglected. When the temperature is low, the concentration variation with time is limited. With an increase of the temperature, the difference becomes obvious, and it takes longer time to reach the steady-state.

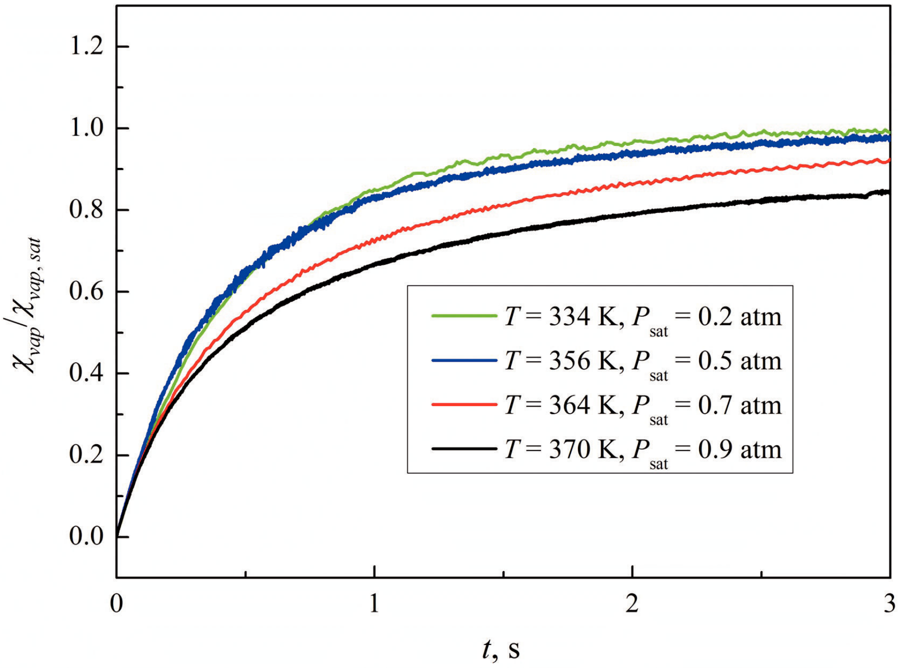

Figure 6.10: The dimensionless mole fraction evolution with time for different temperature.

6.4 Conclusions

An evaporation model based on the Hertz-Knudsen equation was coupled in the VOF model to predict the bubble evaporation in two dimensions. The evaporation-induced temperature variation was also calculated by coupling the heat transfer in the model. Meanwhile, the local concentration distribution and temperature distribution can be predicted. The local temperature variation is very small, which is within 0.5 degree. The concentration distribution affected by evaporation coefficient, shape oscillation, temperature and bubble size were analysed. Following results are obtained:

(1) Different evaporation paramter can have different evaporation rate. The evaporation rate at high evaporation parameter approximately follows an error function.

(2) The shape oscillation can change the concentration distribution inside the

gas bubble and temperature distribution and in the wake. However, since the gas mixing is fast inside the bubble, the shape oscillation has limited effects on the improvement of evaporation rate.

(3) Bubble size is an important factor as it can directly affect the interfacial area for the evaporation coefficient. Smaller bubble size has higher evaporation rate from the very early stage of the bubble evaporation, and it takes shorter time to reach the steady state. For the very small bubble of $d = 3$ mm, the vapour concentration inside the gas bubble can be assumed well-mixed and homogeneous, while it cannot be neglected with an increase of the bubble size.

(4) The effect of the temperature was studied with an effort to the impact of different saturated vapour pressure with a fixed evaporation parameter. At the early stage, they all follow a similar curve. However, their transport difference becomes evident with time, and it takes longer time for the bubbles in higher temperature to reach the saturation.

Chapter 7

Conclusions and Outlook

In this chapter, the main conclusions of the previous chapters are summarized. Thereafter, some suggestions for further work are presented.

7.1 General conclusions

The research carried out in the present study is aimed to numerically simulate the complex phenomena of single bubble dynamics and evaporation in two dimensions. To achieve the goal, in the first part, the bubble fluid dynamics were studied since a thorough understanding of the bubble dynamics is requisite for the bubble evaporation, also with a hope to shed light on the two-dimensional bubble dynamics in liquid metal. The buoyancy-driven single bubble behaviour in a vertical Hele-Shaw cell has been studied. The bubble behaviour was numerically simulated by taking a two-dimensional volume of fluid (VOF) method coupled with a continuum surface force (CSF) model and a wall friction model in the commercial computational fluid dynamics (CFD) package Fluent. By adjusting the viscous resistance values, the bubble dynamics in different gap thicknesses can be simulated. After validation of the bubble dynamic model and extrapolation from a narrow cell to a wide cell, the model was extended to the second task of simulating the bubble dynamics coupled with evaporation at low saturation pressures. The coupled problem of bubble dynamics and interface mass transfer was solved by the VOF model with a Hertz-Knudsen equation based evaporation model. The results obtained during the two parts are summarized here along with some general conclusions.

The results of the simulated two-dimensional bubble dynamics indicate the following:

• The simulated time-averaged bubble properties in a narrow cell with width $W = 5$ cm show that for bubble shape and bubble path, good agreement is obtained between experiment and simulation. The estimated terminal velocity is 90% accurate when the bubble diameter $d > 5$ mm. The amplitude of bubble horizontal velocity and bubble perimeter oscillation can be simulated well with a 50% higher of the oscillation frequency. Three-dimensional effects and spurious vortices are most likely the reason for this inaccuracy. The simulation confirms that the thin liquid films between gas bubbles and the cell walls have a limited effect on the bubble dynamics.

• The effects of the governing parameters of h/d are studied by changing the gap thicknesses, *i.e.* $h = 0.5$, 0.7, 1.0 and 1.5 mm. It was found that with an increased spacing between the cell walls, the bubble shape changes from oblate ellipsoid and spherical-cap to more complicated shapes while the bubble path changes from only rectilinear to a combination of oscillating and rectilinear. The Reynolds number increases with increasing gap thickness. The scaling law $Re = \varphi Ar^{0.7}$ can be applied for the present confined two-dimensional bubble of $W = 5$ cm. The corresponding drag coefficient can be described as $C_D = \frac{\pi}{2\varphi^{2.86}} Re^{0.86}$. The increase of the gap thickness causes a monotonic increase in the constant c, leading to a lower drag coefficient and higher velocity. For the pressure distribution, it was found that a lower pressure is observed in front of the bubble in a thicker gap, which is the main reason for the lower drag coefficient. The pressure in the wake also varies: minimal pressure is present when vortices exist and the numbers increase with increasing gap thickness. The wake length increases with higher liquid velocity when the gap thickness increases. A thicker gap thickness results in more vortices behind the bubble, meanwhile these vortices are unsteady.

- The simulation was extended to simulate the unbounded two-dimensional bubble dynamics within a thin gap. The drag coefficient and the bubble wake are quantified with Roig *et al.*'s [9] experimental measurements. It was found in the simulation that the velocity coefficient follows an exponential decrease as $1/h$, with an equation of $\varphi = 0.667\exp(-0.48 \times 10^{-3}/h)$. Similarly, the drag coefficient follows an exponential increase as $1/h$. The formation and shedding of the vorticity are predicted correctly, both unsteady vortex shedding and trailing steady vortices. The sheded vortex in simulation was found to decay exponentially with time $14t\nu/h^2$, which is faster than the analytical results ($12t\nu/h^2$) and experimental results ($6t\nu/h^2$). The momentum diffusion in the in-plane direction may partially explain the discrepancy between the simulation results and the analytical results. The longitudinal velocity and transverse velocity in the wake can be simulated well, while the exact position for the flow transitions differs due to vortices size differences between experiment and simulation.

The results of the two-dimensional bubble dynamis with evaporation include:

The evaporation-induced bubble growth is simulated. Meanwhile, the local concentration distribution and temperature distribution can be predicted. The local temperature variation is very small, within 0.5 degree. The effects of evaporation parameter, shape oscillation, temperature and bubble size were analyzed. It is found that (1) different evaporation parameter can have different evaporation rate. The evaporation rate at high evaporation parameter approximately follows an error function; (2) shape oscillation can change the concentration distribution inside the gas bubble, also the temperature distribution in the wake. However, since the gas mixing is fast inside the bubble, the shape oscillation has limited effects on the improvement of evaporation rate; (3) bubble size is an important factor as it can directly affect the interfacial area for the evaporation coefficient. Smaller bubble has higher evaporation rate from the very early stage of the bubble evaporation, and it takes shorter time to reach the steady state. For the bubble of $d = 3$ mm, the vapour concentration inside the gas bubble can be assumed well-mixed and homogeneous, while it cannot be neglected with an increase of the bubble size; (4) at the early stage, the bubbles at different temperatures follow a similar curve, then their transport difference becomes evident with time, and it takes longer time for the bubbles at a higher temperature to reach equilibrium.

7.2 Future work

Based on the results and conclusions of this thesis, the following suggestions can be made for further research:

Two-dimensional numerical simulation of bubble dynamics in liquid metal

In the present thesis, the model was investigated on the gas bubble in liquid water and it was validated by the experiment. Since liquid water and liquid metal have similar dynamic viscosity, it is possible to be extend the model with ease to discover the bubble flow properties in the liquid metal. Furthermore, because the liquid flow in the wake can be captured properly, it is possible to understand the liquid velocity distribution in the liquid metal. The simulation can go two ways, either to directly use the present model and get a qualitative results of the bubble dynamics in liquid metal, or to couple the non-wetting boundary conditions to simulate quantitatively the bubble dynamics in liquid metal and validate with Klaasen *et al.*'s [62, 63] experimental measurements.

Compare different surface tension models and adopt them in the present model

The present simulation can obtain similar bubble behavior in many ways, however, the bubble oscillation frequency is double that of the experimental measurements. Since the oscillation frequency is connected to the wake frequency and possibly wake shape and wake structure, an accurate oscillation frequency matters in many ways. From literature, it was found that the current surface tension model is two-order, and higher order's surface tension model may have better performance in oscillation frequency. Therefore how they can affect the bubble dynamics in two-dimensions would be very interesting.

Study the three-dimensional effects on the two-dimensional bubble dynamics

The bubbles in two-dimensions have curvature in the third dimension due to surface tension. How to quantify their effects to the two-dimensional bubble dynamics are important. A proper description of the surface tension in the third dimensions and study their influence on the two dimensional bubbles are important in other similar bubble dynamics such as slug bubbles.

Experiment on the bubble evaporation

The evaporation model in the present study has not been validated by experiments. Whether the evaporation coefficient is close to the value over a flat interface is still unknown. With a careful design of the equipment, the bubble growth can be captured and the evaporation rate can be measured experimentally.

Besides these four suggestions, some related problems such as the numerical simulations of two bubbles, a quantitative study of shape oscillation to the liquid phase mass transfer can be studied both experimentally and simulated with small changes of the model.

Appendix A

Physical properties of $SiCl_4$-Zn system and N_2-H_20 system

A.1 $SiCl_4$-Zn system

The physical properties of the reactants and products in the zinc reduction of silicon tetrachloride include density, viscosity, thermal conductivity, mass diffusion coefficients, surface tension, *et al.*, as listed in Table A.1. The surface tension of liquid zinc is expressed as $\sigma = 0.782 - 0.00017(T - T_m)$ (N/m) [155], where T_m is the melting point. The gas mixture of Zn-$SiCl_4$ can be treated as ideal gas [156]. Because experimental data on high temperature gas transport parameters are not available, these transport properties can be estimated from theoretical kinetic theory for the ideal gas [157].

The experimental values for saturated vapor pressure of liquid zinc can be expressed as [158]:

$$p = \exp(-6620/T - 1.255 \log T + 13.21) \tag{A.1}$$

Where p is in mmHg, T is the temperature in Kelvin. The equation is applicable from melting point to boiling point.

Table A.1: Physical properties of $SiCl_4$–Zn system [159,160].

Physical properties	Zn(l)	Zn(g)	$SiCl_4$(g)	$ZnCl_2$(g)	Si(s)
Molecular weight	65.38	65.38	169.90	136.29	28.09
Density, kg·m^{-3}	$6580 - 9.8(T - T_m)$	Ideal gas	Ideal gas	Ideal gas	2320
Melting point, °C	419.53	419.53	-68.74	292	1414
Boiling point, °C	907	907	57.64	732	3265
Viscosity, Pa·S	0.00385 (419°C)	–	–	–	>10
Diffusion coefficient, m^2·s^{-1}	$\sim 10^{-9}$	–	–	–	–
Thermal conductivity, W·m^{-1}·K^{-1}	56.52	–	–	–	149

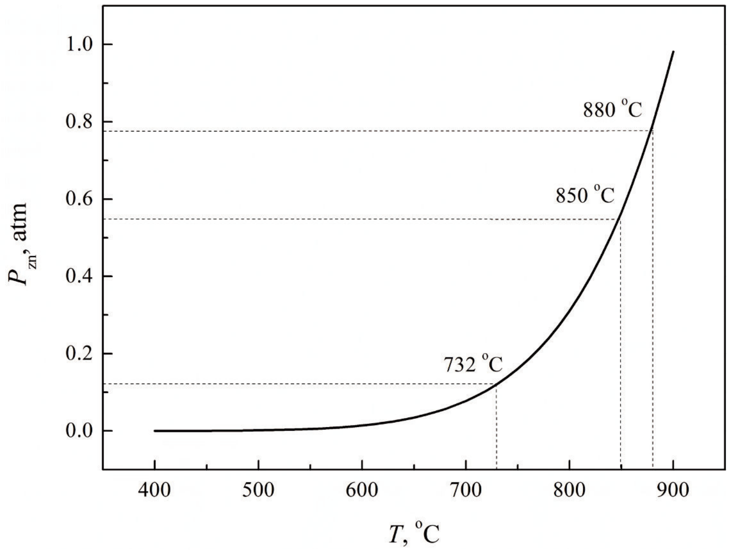

Figure A.1: Vapor pressure curve of liquid zinc.

A.2 N_2-H_2O system

The physical properties of N_2-H_2O system are extracted from FLUENT database, as shown in Table A.2.

Table A.2: The physical properties of N_2-H_2O system.

Physical properties	H_2O(l)	N_2(g)	H_2O(g)
Molecular weight	18	28	18
Density, kg·m^{-3}	997	1.185	0.554
Melting point, °C	0	-210	0
Boiling point, °C	100	-196	100
Viscosity, Pa·S	8.94×10^{-9}	1.66×10^{-5}	1.34×10^{-5}
Diffusion coefficient, m^2·s^{-1}	–	2.88×10^{-5}	2.88×10^{-5}
Thermal conductivity, W·m^{-1}·K^{-1}	0.60	0.024	0.0261

The experimental values for saturated vapor pressure of liquid water can be expressed as [161]:

$$p = \exp(20.386 - 5132/T) \tag{A.2}$$

Where p in mmHg, T is the temperature in Kelvin. The vapor pressure equation (A.2) is shown in Figure A.2.

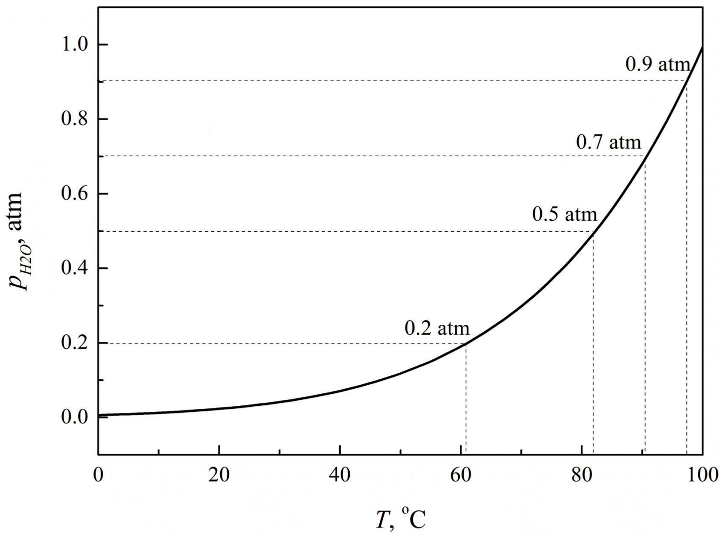

Figure A.2: Vapor pressure curve of liquid water.

Appendix B

The Illustration of Interface mass transfer model

- **Find interface grid cells**.

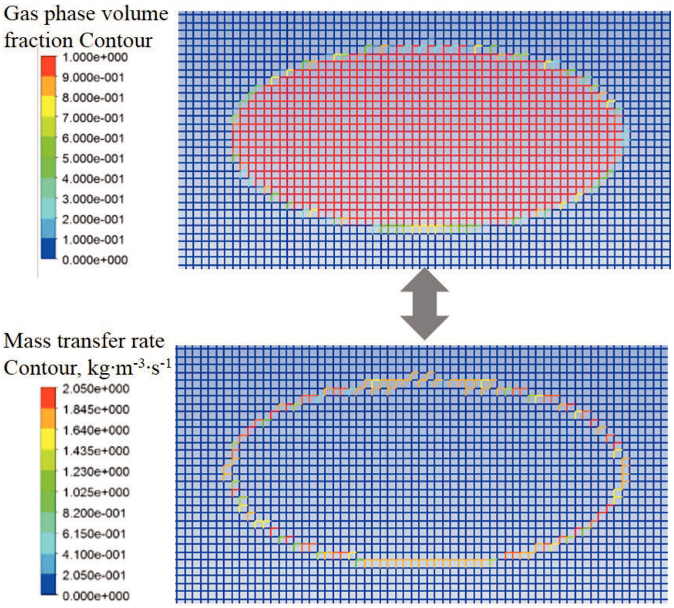

Figure B.1: The illustration of interface grid cells for mass transfer.

- **Calculate interface area A**.

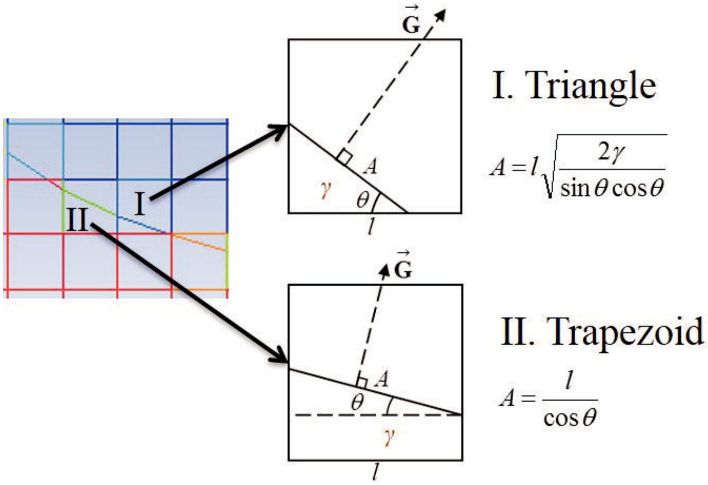

Figure B.2: The two area expressions for triangle interface(I) and trapezoid (II), respectively. l is the grid cell length.

More details can be found in the UDF.

```
/*******************************************************************
 UDF to define a simple mass transfer based on Saturation
   Temperature. The "from" phase is the gas and the "to" phase is the
   liquid phase
*******************************************************************/

#include "udf.h"
#include "sg.h"
#include "sg_mphase.h"
#include "flow.h"
#include "mem.h"
#include "metric.h"
#define denliq 998.2
#define denvap 1.225
#define denint 499.7125
DEFINE_ADJUST(store_VOF_gradient, domain)
 {
        real sum=0;
        Thread *t;
         Thread *ppt;
          Thread **pt;
          cell_t c;
           int phase_domain_index=1;
            Domain *pDomain = DOMAIN_SUB_DOMAIN(domain,phase_domain_index);
```

```
             Alloc_Storage_Vars(pDomain,SV_VOF_RG,SV_VOF_G,SV_NULL);
             Scalar_Reconstruction(pDomain, SV_VOF,-1,SV_VOF_RG,NULL);
              Scalar_Derivatives(pDomain,SV_VOF,-1,SV_VOF_G,SV_VOF_RG, Vof_Deriv_Accumulate);
              mp_thread_loop_c (t,domain,pt)
               {
                 if (FLUID_THREAD_P(t))
                        {
                                ppt = pt[phase_domain_index];
                                begin_c_loop (c,t)
                                 {
                                         C_UDMI(c,t,0) = C_VOF_G(c,ppt)[0];
                                          C_UDMI(c,t,1) = C_VOF_G(c,ppt)[1];
                                           C_UDMI(c,t,2) = C_VOF_G(c,ppt)[2];
                                           sum=sum+C_UDMI(c,t,3);
                                 }
                   end_c_loop (c,t)
                                }
                }
             Free_Storage_Vars(pDomain,SV_VOF_RG,SV_VOF_G,SV_NULL);
             Message("sum= %f  \n",sum);
}

DEFINE_MASS_TRANSFER(evap_source,cell,thread,from_index,from_species_index, to_index, to_species_index)
{
 #if !RP_HOST
  real vof;
  real x,y,c_val,area;
  real xc[ND_ND];
  int curr_ts;
        real m_lg;
        real coeff=0.0000000234;
        real pvap,partp;
        Thread *gas = THREAD_SUB_THREAD(thread, to_index);
        Thread *liq = THREAD_SUB_THREAD(thread, from_index);
        face_t f;
        Thread *tf;
        int n;
        int h=0;
        int l=0;
        m_lg=0.0;

        c_face_loop(cell, thread, n)         /* loops over all faces of a cell */
        {
                f = C_FACE(cell,thread,n);
                tf = C_FACE_THREAD(cell,thread,n);

                if (F_R(f,tf) > denint)
                        h=1;
                if (F_R(f,tf) <= denint)
                        l=1;
        }
           curr_ts=N_TIME;
           C_CENTROID(xc,cell,thread);
           vof=C_VOF(cell,gas);
        if (h==1 && l==1)
        {
```

```
                temp=C_T(cell,thread);
                pvap=exp(20.386-(5132.0/temp))/760.0*101325.0;
                partp=(C_P(cell,thread)+101325) *
C_YI(cell,gas,to_species_index)/18/(C_YI(cell,gas,to_species_index)/18+(1-
C_YI(cell,gas,to_species_index))/28);

   x=fabs(C_UDMI(cell,gas,0));
   y=fabs(C_UDMI(cell,gas,1));
   if(x>y)
    c_val=y/2/x;
    else
    c_val=x/2/y;
  if(vof>0.5)
    vof=1-vof;
    if(vof>c_val)
    area=sqrt(1+4*c_val*c_val);
    else
    area=sqrt(2*vof*(y/x+x/y));

                /*C_UDMI(cell,thread,0)=1.0;*/
                C_UDMI(cell,gas,3)=area;
                C_UDMI(cell,liq,3)=area;
          m_lg = coeff*(pvap - partp)*area/0.00025;
        }
        else
                {
                C_UDMI(cell,gas,3)=0;
                C_UDMI(cell,liq,3)=0;
                        }
        if (m_lg>0.0)
                return (m_lg);
        else
                return (0.0);

 #endif

}
```

Bibliography

[1] J.R. Davis. Aluminum and Aluminum Alloys. page 210. ASM International, 1993.

[2] Dipak Mazumdar and James W. Evans. Modeling of Steelmaking Processes. page 85. CRC Press, 2009.

[3] N. Kantarci, F. Borak, and K.O. Ulgen. Bubble column reactors. *Process Biochemistry*, 40:2263–2283, 2005.

[4] M. van Sint Annaland, N.G. Deen, and J.A.M. Kuipers. Multi-level modelling of dispersed gas-liquid two-phase flows. In *Bubbly Flows*, pages 139–157. Springer, 2004.

[5] G.B. Marin. Multiscale Simulation and Design. volume 40, page 24. Academic Press, 2011.

[6] B. Aboulhasanzadeh, S. Thomas, M. Taeibi-Rahni, and G. Tryggvason. Multiscale computations of mass transfer from buoyant bubbles. *Chemical Engineering Science*, 75:456–467, 2012.

[7] I. Roghair. *Direct Numerical Simulations of Hydrodynamics and Mass Transfer in Dense Bubbly Flows.* PhD thesis, Technische Universiteit Eindhoven, 2012.

[8] K. Ono and T. Matsushima. On the production of pure silicon. *The 61st Report of Research Institute of Mineral Dressing and Metallurgy*, pages 477–496, 1954.

[9] V. Roig, M. Roudet, F. Risso, and A. Billet. Dynamics of a high-Reynolds-number bubble rising within a thin gap. *Journal of Fluid Mechanics*, 707:444–466, 2012.

[10] W.G. Davenport, A. V. Bradshaw, and F.D. Richardson. Behavior of spherical cap bubbles in liquid metals. *Journal of the Iron and Steel Institute*, 205:1034–1042, 1967.

[11] J. Szekely. *Fluid Flow Phenomena In Metals Processing.* Elsevier Science, 2012.

[12] Paneni and W.G. Davenport. Dynamics of bubbles in liquid metals: two dimensional experiments. *Metallurgical Transactions*, 1:297–297, 1970.

[13] Schwerdtfeger, K. Velocity of rise of argon bubbles in mercury. *Chemical Engineering Science*, 23:937–938, 1968.

[14] S. Eckert, W. Witke, and G. Gerbeth. A new mechano-optical technique to measure local velocities in opaque fluids. *Flow Measurement and Instrumentation*, 11:71–78, 2000.

[15] A.C. Mikrovas and S.A. Argyropoulos. Measurement of velocity in high-temperature liquid metals. *Metallurgical Transactions B*, 24:1009–1022, 1993.

[16] S. Eckert, G. Gerbeth, and V.I. Melnikov. Velocity measurements at high temperatures by ultrasound Doppler velocimetry using an acoustic wave guide. *Experiments in Fluids*, 35:381–388, 2003.

[17] Q. Fu. *Optimization of chlorine fluxing process for magnesium removal from molten aluminum.* Ph.d thesis, University of California, Berkeley,, 1998.

[18] M. Iguchi, T. Nakatani, and H. Kawabata. Development of a multineedle electroresistivity probe for measuring bubble characteristics in molten metal baths. *Metallurgical and Materials Transactions B*, 28:409–416, 1997.

[19] Y. Saito, X. Shen, K. Mishima, and M. Matsubayashi. Shape measurement of bubble in a liquid metal. *Nuclear Instruments and Methods in Physics Research*, 605:192–196, 2009.

[20] B. Klaasen. *Gas bubbles in liquid metal in a Hele-Shaw cell a mesocropic study.* Ph.d thesis, University of Leuven, 2014.

[21] J.K. Brimacombe, E.S. Stratigakos, and P. Tarassoff. Mass transfer between a horizontal, submerged gas jet and a liquid. *Metallurgical Transactions*, 5:763–771, 1974.

[22] J.R.F. Guedes de Carvalho, F.A.N. Rocha, M.I. Vasconcelos, M.C.M. Silva, and F.A.R. Oliveira. Mass transfer during bubbling in single and multi-orifice absorbers. *Chemical Engineering Science*, 41:1987–1994, 1986.

[23] R.M. Davies and G. Taylor. The mechanics of large bubbles rising through extended liquids and through liquids in tubes. *Proceedings of the Royal Society of London A*, 200:375–390, 1950.

[24] W.G. Davenport, F.D. Richardson, and A.V. Bradshaw. Spherical cap bubbles in low density liquids. *Chemical Engineering Science*, 22:1221–1235, 1967.

[25] R. Clift, J.R. Grace, and M.E. Weber. Bubbles, Drops, and Particles. pages 1–240. Acedemic press, 1978.

[26] A.A. Kulkarni and J.B. Joshi. Bubble Formation and Bubble Rise Velocity in Gas - Liquid Systems : A Review. *Industrial and Engineering Chemistry Research*, 44:5873–5931, 2005.

[27] F. Durst, B. Schönung, K. Selanger, and M. Winter. Bubble-driven liquid flows. *Journal of Fluid Mechanics*, 170:53–82, 1986.

[28] M.I. Urseanu. *Scaling up bubble column reactors*. Ph.d thesis, Universiteit Van Amsterdam, 2000.

[29] M. Wu and M. Gharib. Experimental studies on the shape and path of small air bubbles rising in clean water. *Physics of Fluids*, 14:L49–L52, 2002.

[30] P.C. Duineveld. The rise velocity and shape of bubbles in pure water at high Reynolds number. *Journal of Fluid Mechanics*, 292:325–332, 1995.

[31] K. Ellingsen and F. Risso. On the rise of an ellipsoidal bubble in water: oscillatory paths and liquid-induced velocity. *Journal of Fluid Mechanics*, 440:235–268, 2001.

[32] W.L. Shew, S. Poncet, and J.F. Pinton. Force measurements on rising bubbles. *Journal of Fluid Mechanics*, 569:51–60, 2006.

[33] G. Mougin and J. Magnaudet. Path instability of a rising bubble. *Physical Review Letters*, 88:014502, 2002.

[34] T. Sanada, M. Shirota, and M. Watanabe. Bubble wake visualization by using photochromic dye. *Chemical Engineering Science*, 62:7264–7273, 2007.

[35] C. Bru. Structure and dynamics of the wake of bubbles and its relevance for bubble interaction. *Physics of Fluids*, 11:1781–1796, 1999.

[36] G.K. Batchelor. The stability of a large gas bubble rising through liquid. *Journal of Fluid Mechanics*, 184:399–422, 1987.

[37] K. Tsuchiya and L. Fan. Near-wake structure of a single gas bubble in a two-dimensional liquid-solid fluidized bed: vortex shedding and wake size variation. *Chemical Engineering Science*, 43:1167–1181, 1988.

[38] P.G. Saffman. On the rise of small air bubbles in water. *Journal of Fluid Mechanics*, 1:249–275, 1956.

[39] H.D. Mendelson. The prediction of bubble terminal velocities from wave theory. *AIChE Journal*, 13:250–253, 1967.

[40] G. Bozzano and M. Dente. Shape and terminal velocity of single bubble motion: a novel approach. *Computer aided chemical engineering*, 8:649–654, 2000.

[41] D. Rodrigue. A general correlation for the rise velocity of single gas bubbles. *The Canadian Journal of Chemical Engineering*, 82:382–386, 2004.

[42] M. Stöhr, J. Schanze, and A. Khalili. Visualization of gas-liquid mass transfer and wake structure of rising bubbles using pH-sensitive PLIF. *Experiments in Fluids*, 47:135–143, 2009.

[43] A.B. Newman. The Drying of Porous Solids: Diffusion Calculations, and Diffusion and Surface Emission Equations. *Transactions of the American Institute of Chemical Engineers*, 27:203–211, 1931.

[44] R. Kronig and J.C. Brink. On the theory of extraction from falling droplets. *Applied Scientific Research*, 2:142–154, 1950.

[45] L.E. Johns and R.B. Beckmann. Mechanism of dispersed phase mass transfer in visous, single drop extraction system. *AIChE Journal*, 12:10–16, 1966.

[46] H. Watada, A.E. Hamielec, and A.I. Johnson. A theoretical study of mass transfer with chemical reaction in drops. *The Canadian Journal of Chemical Engineering*, 48:255–261, 1970.

[47] M. Filla, J.F. Davidson, J.F. Bates, and M.A. Eccles. Gas phase controlled mass transfer from a bubble. *Chemical Engineering Science*, 31:359–367, 1976.

[48] T. Taha and Z.F. Cui. Hydrodynamics of slug flow inside capillaries. *Chemical Engineering Science*, 59:1181–1190, 2004.

[49] N.E. Zaritzky and A. Calvelo. Internal mass transfer coefficient within single bubbles theory and experiment. *The Canadian Journal of Chemical Engineering*, 57:58–64, 1979.

[50] C.-W. Park and G.M. Homsy. Two-phase displacement in Hele Shaw cells: theory. *Journal of Fluid Mechanics*, 139:291–308, 1984.

[51] B. Sandnes, E.G. Flekkoy, H.A. Knudsen, K.J. Maloy, and H. See. Patterns and flow in frictional fluid dynamics. *Nature communications*, 2:288, 2011.

[52] J.W.M. Bush. The anomalous wake accompanying bubbles rising in a thin gap: a mechanically forced Marangoni flow. *Journal of Fluid Mechanics*, 352:283–303, 1997.

[53] T. Maxworthy. The nonlinear growth of a gravitationally unstable interface in a Hele-Shaw cell. *Journal of Fluid Mechanics*, 177:207–232, 1987.

[54] G.I. Taylor and Saffman P.G. A note on the motion of bubbles in a Hele-Shaw cell and porous medium. *The Quarterly Journal of Mechanics and Applied Mathematics*, 12:265–279, 1959.

[55] S. Tanveer. The effect of surface tension on the shape of a Hele-CShaw cell bubble. *Physics of Fluids*, 29:3537–3548, 1986.

[56] T. Maxworthy. Bubble formation, motion and interaction in a Hele-Shaw cell. *Journal of Fluid Mechanics*, 173:95–114, 1986.

[57] A.R. Kopf-Sill and G.M. Homsy. Nonlinear unstable viscous fingers in Hele-Shaw flows. I. Experiments. *Physics of Fluids*, 31:242–249, 1988.

[58] E. Kelley and M. Wu. Path instabilities of rising air bubbles in a Hele-Shaw cell. *Physical review letters*, 79:1265–1268, 1997.

[59] M. Kawaguchi, S. Niga, N. Gou, and K. Miyake. Buoyancy-driven path instabilities of bubble rising in simple and polymer solutions of Hele-Shaw cell. *Journal of the Physical Society of Japan*, 75:124401, 2006.

[60] H. Kozuka, Y. Ikeda, and M. Kawaguchi. Path instabilities of bubble rising in polymer solutions of Hele-Shaw cell. *Journal of the Physical Society of Japan*, 78:114604, 2009.

[61] M. Yamamoto and M. Kawaguchi. Differences in path instabilities between a bubble rising in water and in aqueous polymer solution in a Hele-Shaw cell in the transient and steady states. *Journal of Dispersion Science and Technology*, 32:1445–1451, 2011.

[62] B. Klaasen, F. Verhaeghe, B. Blanpain, and J. Fransaer. A study of gas bubbles in liquid mercury in a vertical Hele-Shaw cell. *Experiments in Fluids*, 55:1652, 2014.

[63] B. Klaasen, F. Verhaeghe, B. Blanpain, and J. Fransaer. Observing Nitrogen Bubbles in Liquid Zinc in a Vertical Hele-Shaw Cell. *Metallurgical and Materials Transactions B*, pages 1–14, 2015.

[64] M. van Sint Annaland, W. Dijkhuizen, N.G. Deen, and J.A.M. Kuipers. Numerical simulation of behavior of gas bubbles using a 3-D front-tracking method. *AIChE Journal*, 52:99–110, 2006.

[65] William F Noh and Paul Woodward. Slic (simple line interface calculation). In *Proceedings of the Fifth International Conference on Numerical Methods in Fluid Dynamics June 28–July 2, 1976 Twente University, Enschede*, pages 330–340. Springer, 1976.

[66] J.U. Brackbill, D.B. Kothe, and C Zemach. A continuum method for modeling surface tension. *Journal of Computational Physics*, 100:335–354, 1991.

[67] W.J. Rider and D.B. Kothe. Reconstructing Volume Tracking. *Journal of Computational Physics*, 141:112–152, 1998.

[68] S. Osher and J.A. Sethian. Fronts propagating with curvature dependent speed: Algorithms based on Hamilton-Jacobi formulations. *Journal of Computational Physics*, 79:12–49, 1987.

[69] K.B. Deshpande and W.B. Zimmerman. Simulation of interfacial mass transfer by droplet dynamics using the level set method. *Chemical Engineering Science*, 61:6486–6498, 2006.

[70] Z. Yu and L.S. Fan. Direct simulation of the buoyant rise of bubbles in infinite liquid using level set method. *The Canadian Journal of Chemical Engineering*, 86:267–275, 2008.

[71] E. Olsson and G. Kreiss. A conservative level set method for two phase flow. *Journal of Computational Physics*, 210:225–246, 2005.

[72] E. Olsson, G. Kreiss, and S. Zahedi. A conservative level set method for two phase flow II. *Journal of Computational Physics*, 225:785–807, 2007.

[73] D. Enright, R. Fedkiw, J. Ferziger, and I. Mitchell. A hybrid particle level set method for improved interface capturing. *Journal of Computational Physics*, 183(1):83–116, 2002.

[74] G. Tryggvason, B. Bunner, A. Esmaeeli, D. Juric, N. Al-Rawahi, W. Tauber, J. Han, S. Nas, and Y.-J. Jan. A front-tracking method for the computations of multiphase flow. *Journal of Computational Physics*, 169:708–759, 2001.

[75] G. Tryggvason, R. Scardovelli, and S. Zaleski. Direct Numerical Simulations of Gas-Liquid Multiphase Flows. page 95. Cambridge University Press, 2011.

[76] R. Singh and W. Shyy. Three-dimensional adaptive Cartesian grid method with conservative interface restructuring and reconstruction. *Journal of Computational Physics*, 224:150–167, 2007.

[77] M. van Sint Annaland, N.G. Deen, and J.A.M. Kuipers. Numerical simulation of gas bubbles behaviour using a three-dimensional volume of fluid method. *Chemical Engineering Science*, 60:2999–3011, 2005.

[78] I.R. Park, K.S. Kim, J. Kim, and S.H. Van. A volume-of-fluid method for incompressible free surface flows. *International Journal for Numerical Methods in Fluids*, 61:1331–1362, 2009.

[79] G. Mougin and J. Magnaudet. Wake-induced forces and torques on a zigzagging/spiralling bubble. *Journal of Fluid Mechanics*, 567:185–194, 2006.

[80] R. Krishna and J.M. Van Baten. Simulating the motion of gas bubbles in a liquid. *Nature*, 398:208–208, 1999.

[81] D. Gaudlitz and N.A. Adams. Numerical investigation of rising bubble wake and shape variations. *Physics of Fluids*, 21:122102, 2009.

[82] J. Zhang and M.J. Ni. Direct simulation of single bubble motion under vertical magnetic field: Paths and wakes. *Physics of Fluids*, 26:102102, 2014.

[83] M. Kroger, A. Alke, D. Bothe, and H. Warnecke. A vof-based approach for the simulation of reactive mass transfer from rising bubbles. *Fortschritt Berichte-VDI Reihe 3 Verfahrenstechnik*, 883:290, 2007.

[84] A.A. Ganguli and E.Y. Kenig. A CFD-based approach to the interfacial mass transfer at free gas¨Cliquid interfaces. *Chemical Engineering Science*, 66:3301–3308, 2011.

[85] G. Pianet, S. Vincent, J. Leboi, J.P. Caltagirone, and M. Anderhuber. Simulating compressible gas bubbles with a smooth volume tracking 1-Fluid method. *International Journal of Multiphase Flow*, 36:273–283, 2010.

[86] A.R. Kopf-Sill and G.M. Homsy. Bubble motion in a Hele-CShaw cell. *Physics of Fluids*, 31:18–26, 1988.

[87] S.R.K. Maruvada and C.-W. Park. Retarded motion of bubbles in Hele-Shaw cells. *Physics of Fluids*, 8:3229–3233, 1996.

[88] W. Eck and J. Siekmann. On bubble motion in a Hele-Shaw cell, a possibility to study 2-phase flows under reduced gravity. *Ingenieur-Archiv*, 47:153–168, 1978.

[89] R. Collins. A simple model of the plane gas bubble in a finite liquid. *Journal of Fluid Mechanics*, 22:763–771, 1966.

[90] F. Riegels. Zur Kritik des Hele-Shaw-Versuchs. *Zeitschrift fur Angewandte Mathematik und Mechanik*, 18:95–106, 1938.

[91] S.G. Huisman, P. Ern, and V. Roig. Interaction and coalescence of large bubbles rising in a thin gap. *Physical Review E*, 85:027302, 2012.

[92] J.W.M. Bush and I. Eames. Fluid displacement by high Reynolds number bubble motion in a thin gap. *International Journal of Multiphase Flow*, 24:411–430, 1998.

[93] D. Ma, M. Liu, Y. Zu, and C. Tang. Two-dimensional volume of fluid simulation studies on single bubble formation and dynamics in bubble columns. *Chemical Engineering Science*, 72:61–77, 2012.

[94] W. Boos and A. Thess. Thermocapillary flow in a Hele-Shaw cell. *Journal of Fluid Mechanics*, 352:305–330, 1997.

[95] P. Gondret and M. Rabaud. Shear instability of two-fluid parallel flow in a Hele-Shaw cell. *Physics of Fluids*, 9:3267–3274, 1997.

[96] A. Tatulchenkov and A. Cebers. Complex bubble dynamics in a vertical Hele-Shaw cell. *Physics of Fluids*, 17:107103, 2005.

[97] N. Jarrige, I. Bou Malham, J. Martin, N. Rakotomalala, D. Salin, and L. Talon. Numerical simulations of a buoyant autocatalytic reaction front in tilted Hele-Shaw cells. *Physical Review E - Statistical, Nonlinear, and Soft Matter Physics*, 81:066311, 2010.

[98] R. Krishna and J.M. Van Baten. Rise characteristics of gas bubbles in a 2D rectangular column: VOF simulation vs experiment. *International Communications in Heat and Mass Transfer*, 26:965–974, 1999.

[99] J.M. Van Baten and R. Krishna. CFD simulations of mass transfer from Taylor bubbles rising in circular capillaries. *Chemical Engineering Science*, 59:2535–2545, 2004.

[100] G.S. Beavers, E.M. Sparrow, and R.A. Magnuson. Experiments on the breakdown of laminar flow in a parallel-plate channel. *International Journal of Heat and Mass Transfer*, 13:809–815, 1970.

[101] I. Lunati and D. Or. Gravity-driven slug motion in capillary tubes. *Physics of Fluids*, 21:052003, 2009.

[102] M. Seifollahi, E. Shirani, and N. Ashgriz. An improved method for calculation of interface pressure force in PLIC-VOF methods. *European Journal of Mechanics B*, 27:1–23, 2008.

[103] S.Y. Lin, Y.H. Chin, C.M. Wu, J.F. Lin, and Y.C. Chen. A pressure correction-volume of fluid method for simulation of two-phase flows. *International Journal for Numerical Methods in Fluids*, 68:181–195, 2010.

[104] D.L. Youngs. Time-dependent multi-material flow with large fluid distortion. pages 27–39. Academic Press, 1982.

[105] V. Kolár. Vortex identification: New requirements and limitations. *International Journal of Heat and Fluid Flow*, 28:638–652, 2007.

[106] J. Zhou, R.J. Adrian, S. Balachandar, and T.M. Kendall. Mechanisms for generating coherent packets of hairpin vortices in channel flow. *Journal of Fluid Mechanics*, 387:353–396, 1999.

[107] B.G.M. van Wachem and J.C. Schouten. Experimental validation of 3-D lagrangian VOF model: Bubble shape and rise velocity. *AIChE Journal*, 48:2744–2753, 2002.

[108] M.R. Ansari and M.E. Nimvari. Bubble viscosity effect on internal circulation within the bubble rising due to buoyancy using the level set method. *Annals of Nuclear Energy*, 38:2770–2778, 2011.

[109] K.D. Danov, D.S. Valkovska, and P.A. Kralchevsky. Hydrodynamic instability and coalescence in trains of emulsion drops or gas bubbles moving through a narrow capillary. *Journal of Colloid and Interface Science*, 267:243–258, 2003.

[110] E. Bouche, V. Roig, F. Risso, and A.-M. Billet. Homogeneous swarm of high-Reynolds-number bubbles rising within a thin gap. Part 1. Bubble dynamics. *Journal of Fluid Mechanics*, 704:211–231, 2012.

[111] G.M. Lazarek and H. Littman. The pressure field due to a large circular capped air bubble rising in water. *Journal of Fluid Mechanics*, 66:673–687, 1974.

[112] W.F. Bessler and H. Littman. Experimental studies of wakes behind circularly capped bubbles. *Journal of Fluid Mechanics*, 185:137–151, 1987.

[113] X. Wang, B. Klaasen, J. Degrève, B. Blanpain, and F. Verhaeghe. Experimental and numerical study of buoyancy-driven single bubble dynamics in a vertical Hele-Shaw cell Experimental and numerical study of buoyancy-driven single bubble dynamics in a vertical Hele-Shaw cell. *Physics of Fluids*, 26:123303, 2014.

[114] J.H. Hills. The two-dimensional elliptical cap bubble. *Journal of Fluid Mechanics*, 68:503–512, 1975.

[115] Y. Yang and H. Levine. Spherical cap bubbles. *Journal of Fluid Mechanics*, 235:73–87, 1992.

[116] K. Raghunathan, S. Kumar, and L.-S. Fan. Pressure distribution and vortical structure in the wake behind gas bubbles in liquid and liquid-solid systems. *International Journal of Multiphase Flow*, 18:41–50, 1992.

[117] L.-S. Fan and K. Tsuchiya. Bubble wake dynamics in liquids and liquid-solid suspensions. page 71. Butterworths-Heinemann, 1990.

[118] L. Han and M.H. Al-Dahhan. Gas-liquid mass transfer in a high pressure bubble column reactor with different sparger designs. *Chemical Engineering Science*, 62:131–139, 2007.

[119] T. Maxworthy. A note on the existence of wakes behind large, rising bubbles. *Journal of Fluid Mechanics*, 27:367–368, 1967.

[120] J.Y. Parlange. Spherical cap bubbles with laminar wakes. *Journal of Fluid Mechanics*, 37:257–263, 2006.

[121] A.W.G. De Vries, A. Biesheuvel, and L. Van Wijngaarden. Notes on the path and wake of a gas bubble rising in pure water. *International Journal of Multiphase Flow*, 28:1823–1835, 2002.

[122] K. Sakakibara, M. Yamada, Y. Miyamoto, and T. Saito. Measurement of the surrounding liquid motion of a single rising bubble using a Dual-Camera PIV system. *Flow Measurement and Instrumentation*, 18:211–215, 2007.

[123] Z. Liu and Y. Zheng. PIV study of bubble rising behavior. *Powder Technology*, 168:10–20, 2006.

[124] M. Roudet, A.M. Billet, F. Risso, and V. Roig. PIV with volume lighting in a narrow cell: An efficient method to measure large velocity fields of rapidly varying flows. *Experimental Thermal and Fluid Science*, 35:1030–1037, 2011.

[125] Z. Liu, Y. Zheng, L. Jia, and Q. Zhang. Study of bubble induced flow structure using PIV. *Chemical Engineering Science*, 60:3537–3552, 2005.

[126] R. Zenit and J. Magnaudet. Measurements of the streamwise vorticity in the wake of an oscillating bubble. *International Journal of Multiphase Flow*, 35:195–203, 2009.

[127] R. Zenit and J. Magnaudet. Path instability of rising spheroidal air bubbles: A shape-controlled process. *Physics of Fluids*, 20:061702, 2008.

[128] J. Magnaudet and G. Mougin. Wake instability of a fixed spheroidal bubble. *Journal of Fluid Mechanics*, 572:311–337, 2007.

[129] Xue Wang, Bart Klaasen, Jan Degrève, Bart Blanpain, and Frederik Verhaeghe. Volume-of-fluid simulations of bubble dynamics in a vertical Hele-Shaw cell. Submitted to *Physics of Fluids*.

[130] M.T. Pauken. An experimental investigation of combined turbulent free and forced evaporation. *Experimental Thermal and Fluid Science*, 18:334–340, 1998.

[131] I.W. Eames, N.J. Marr, and H. Sabir. The evaporation coefficient of water: a review. *International Journal of Heat and Mass Transfer*, 40:1963–2973, 1997.

[132] E. Sartori. A critical review on equations employed for the calculation of the evaporation rate from free water surfaces. *Solar Energy*, 68:77–89, 2000.

[133] P. Rahimi and C.A. Ward. Kinetics of evaporation: statistical rate theory approach. *International Journal of Thermodynamics*, 8:1–14, 2005.

[134] L.E. Scriven. On the dynamics of phase growth. *Chemical Engineering Science*, 50:1–13, 1959.

[135] J. Wang, P. Lu, Z. Wang, C. Yang, and Z. Mao. Numerical simulation of unsteady mass transfer by the level set method. *Chemical Engineering Science*, 63:3141–3151, 2008.

[136] P. Lu, Z. Wang, C. Yang, and Z. Mao. Experimental investigation and numerical simulation of mass transfer during drop formation. *Chemical Engineering Science*, 65:5517–5526, 2010.

[137] Z. Wang, P. Lu, Y. Wang, C. Yang, and Z. Mao. Experimental Investigation and Numerical Simulation of Marangoni Effect Induced by Mass Transfer during Drop Formation. *AIChE Journal*, 59:4424–4439, 2013.

[138] G. Strotos, M. Gavaises, A. Theodorakakos, and G. Bergeles. Numerical investigation of the evaporation of two-component droplets. *Fuel*, 90:1492–1507, 2011.

[139] D. Sun, J. Xu, and L. Wang. Development of a vapor¨Cliquid phase change model for volume-of-fluid method in FLUENT. *International Communications in Heat and Mass Transfer*, 39:1101–1106, 2012.

[140] W. Lee, G. Son, and H.Y. Yoon. Direct numerical simulation of flow boiling in a finned microchannel. *International Communications in Heat and Mass Transfer*, 39:1460–1466, 2012.

[141] R. Banerjee. Turbulent conjugate heat and mass transfer from the surface of a binary mixture of ethanol/iso-octane in a countercurrent stratified two-phase flow system. *International Journal of Heat and Mass Transfer*, 51:5958–5974, 2008.

[142] J.B. Haelssig, A.Y. Tremblay, J. Thibault, and S.G. Etemad. Direct numerical simulation of interphase heat and mass transfer in multicomponent vapour-liquid flows. *International Journal of Heat and Mass Transfer*, 53:3947–3960, 2010.

[143] A. Hassanvand and S.H. Hashemabadi. Direct numerical simulation of interphase mass transfer in gas ¨C liquid multiphase systems. *International Communications in Heat and Mass Transfer*, 38:943–950, 2011.

[144] D.G. Kröger and G.R. Branfield. Evaporation from a Water Surface : Theory and Experiment. *R&D Journal of the South African Institution of Mechanical Engineering*, 23:5–11, 2007.

[145] A. Alke, D. Bothe, M. Kroeger, and H.J. Warnecke. VOF-based simulation of conjugate mass transfer from freely moving fluid particles. *Computational Methods in Multiphase Flow V*, pages 157–168, 2009.

[146] S. Hardt and F. Wondra. Evaporation model for interfacial flows based on a continuum-field representation of the source terms. *Journal of Computational Physics*, 227:5871–5895, 2008.

[147] S. Jeon, S. Kim, and G. Park. Numerical study of condensing bubble in subcooled boiling flow using volume of fluid model. *Chemical Engineering Science*, 66:5899–5909, 2011.

[148] H. Marschall, K. Hinterberger, C. Schüler, F. Habla, and O. Hinrichsen. Numerical simulation of species transfer across fluid interfaces in free-surface flows using OpenFOAM. *Chemical Engineering Science*, 78:111–127, 2012.

[149] G. Strotos, M. Gavaises, A. Theodorakakos, and G. Bergeles. Numerical investigation on the evaporation of droplets depositing on heated surfaces at low Weber numbers. *International Journal of Heat and Mass Transfer*, 51:1516–1529, 2008.

[150] S. Popov, A. Melling, F. Durst, and C.A. Ward. Apparatus for investigation of evaporation at free liquid-vapour interfaces. *International Journal of Heat and Mass Transfer*, 48:2299–2309, 2005.

[151] R. Marek and J. Straub. Analysis of the evaporation coefficient and the condensation coefficient of water. *International Journal of Heat and Mass Transfer*, 44:39–53, 2001.

[152] T.H. Yang and C. Pan. Molecular dynamics simulation of a thin water layer evaporation and evaporation coefficient. *International Journal of Heat and Mass Transfer*, 48:3516–3526, 2005.

[153] V.K. Badam, V. Kumar, F. Durst, and K. Danov. Experimental and theoretical investigations on interfacial temperature jumps during evaporation. *Experimental Thermal and Fluid Science*, 32:276–292, 2007.

[154] U.D. Kück, M. Schlüter, and N. Räbiger. Analyse des grenzschichtnahen Stofftransports an frei aufsteigenden Gasblasen. *Chemie Ingenieur Technik*, 81:1599–1606, 2009.

[155] T. Iida and R.I.L. Guthrie. *The physical properties of liquid metals*. Clarendon Press, 1988.

[156] Ishino T. Matstumoto, A. Manufacture of high-purity silicon. I. Disproportionation reaction of silicon and silicon tetrachloride. *Kogyo Kagaku Zasshi*, 6:262–265, 1965.

[157] R.C. Reid, J.M. Prausnitz, and B.E. Poling. The properties of gases and liquids. page 90. McGraw Hill Book Co.,New York, NY, 1977.

[158] Y.K. Rao. Stoichiometry and thermodynamics of metallurgical processes . Cambridge University Press, 1985.

[159] B. Sylvan. Liquid metals chemistry and physics. page 451. Marcel Dekker, New York, 1972.

[160] R.N. Lyon. Liquid-metal handbooks. page 43. U.S. Government, 1952.

[161] W.M. Haynes. CRC Handbook of Chemistry and Physics. CRC Press, 2012.

Curriculum Vitae

Xue Wang

Date of birth: 20 January 1982

Place of birth: Sichuan, China

Email address: xwang82@outlook.com

Education

• 09. 2010–04. 2015:	PhD student in Engineering Science Department of Materials Engineering (MTM) University of Leuven (KU Leuven) Belgium.
• 09. 2004–07. 2007:	Master in Chemical Technology Key laboratory of Green Process and Engineering Institute of Process Engineering, Chinese Academy of Sciences China.
• 09. 2000–07. 2004:	Bachelor in Metallurgical Technology College of Chemical Engineering Sichuan University China.

Work experience

• 07. 2007–09. 2010:	China Petroleum Chemical Corporation China National Petroleum Corporation China.

List of Publications

Articles in internationally reviewed journals

[1] **X. Wang**, B. Klaasen, J. Degrève, B. Blanpain, F. Verhaeghe. Experimental and numerical study of buoyancy-driven single bubble dynamics in a vertical Hele-Shaw cell. *Physics of Fluids*, 26 (2014) 123303.

[2] **X. Wang**, B. Klaasen, J. Degrève, B. Blanpain, F. Verhaeghe. Volume-of-fluid simulations of bubble dynamics in a vertical Hele-Shaw cell. (Submitted to *Physics of Fluids*)

[3] **X. Wang**, B. Klaasen, J. Degrève, A. Mahulkar, G. Heynderickx, M. Reyniers, B. Blanpain, F. Verhaeghe. A quantitative modelling of two-dimensional rising bubble dynamics: drag coefficient and bubble wake. (In preparation)

[4] **X. Wang**, A. Mahulkar, B. Klaasen, J. Degrève, M. Reyniers, B. Blanpain, F. Verhaeghe. Numerical simulation of bubble dynamics and evaporation. (In preparation)

Papers at international conferences, published in full in proceedings

[1] **X. Wang**, B. Klaasen, J. Degrève, B. Blanpain, F. Verhaeghe. Two dimensional numerical simulation of bubble dynamics in a vertical Hele-Shaw cell. *CFD2014: Proceedings of 10th International Conference on CFD in Oil and Gas, Metallurgical and Process Industries, SINTEF*, Trondheim, Norway, Jun 17-19, 2014. pp. 687-694.

FACULTY OF ENGINEERING SCIENCE
DEPARTMENT OF MATERIALS ENGINEERING (MTM)
HIGH TEMPERATURE PROCESSES AND INDUSTIAL ECOLOGY
Kasteelpark Arenberg 44 bus 2450
B-3001 Heverlee
Xue.Wang@mtm.kuleuven.be
http://www.mtm.kuleuven.be